Universidade de Aveiro Departamento de Engenharia Mecânica
2014

Alexandre Manuel
Ferreira Magalhães

Modelação Termomecânica e Simulação Numérica de Processos de Sinterização

Thermo-mechanical Modelling and Numerical Simulation of Sintering Processes

Universidade de Aveiro Departamento de Engenharia Mecânica
2014

Alexandre Manuel
Ferreira Magalhães

Modelação Termomecânica e Simulação Numérica de Processos de Sinterização

Thermo-mechanical Modelling and Numerical Simulation of Sintering Processes

Dissertação apresentada à Universidade de Aveiro para cumprimento dos requisitos necessários à obtenção do grau de Mestre em Engenharia Mecânica, realizada sob orientação científica de Robertt Angelo Fontes Valente, Professor Auxiliar do Departamento de Engenharia Mecânica e co-orientação científica de António Gil d'Orey Andrade-Campos, Professor Auxiliar do Departamento de Engenharia Mecânica da Universidade de Aveiro

O júri / The jury

Presidente / President

Prof. Doutor João Alexandre Dias Oliveira
Professor Auxiliar da Universidade de Aveiro

Prof. Doutora Dulce Maria Esteves Rodrigues
Professora Auxiliar da Universidade de Coimbra

Vogais / Committee

Prof. Doutor Robertt Angelo Fontes Valente
Professor Auxiliar da Universidade de Aveiro (orientador)

Agradecimentos / Acknowledgements

Gostaria de agradecer ao grupo de investigação que me acolheu para o desenvolvimento deste trabalho, GRIDS, em especial aos meus orientadores: Professor Doutor Robertt Valente e o Professor Doutor Gil Campos e também um obrigado especial ao investigador Engenheiro Bruno Barroqueiro.

Um especial obrigado também a todos os meus amigos que estiveram sempre por perto ao longo do meu percuso académico nesta academia

Por último, mas não menos importante, um agradecimento aos meus pais porque sem o seu apoio, certamente hoje não estaria a concluir esta etapa da minha vida.

Palavras-chave

Metalurgia do Pó, Compactação, Sinterização, Método dos Elementos Finitos, Modelo Elasto-Plástico, Modelo Viscoelástico e Subrotinas de Utilizador.

Resumo

A metalurgia do pó é uma indústria vincada no fabrico de componentes de metal duro. Este tipo de indústria tem a característica de produzir peças de elevada complexidade através de pó metálico. Nos vários estágios que caracteriza a metalurigia do pó, dois são essenciais: o processo de compactação e o processo de sinterização. No processo de compactação, a preocupação está em produzir um corpo poroso, em que tenha as caracteristicas mecânicas ideias para prosseguir para o estágio de sinterização. Assim, a compactação de pós metálicos pode ser simulada recorrendo a modelos contínuos elasto-plásticos adoptados da mecânica dos solos. Estes modelos são normalmente implementados em código de elementos finitos e são usados para investigar as propriedades mecânicas do pó durante a compactação. No presente estudo demonstra-se o comportamento do fluxo do pó metálico, um aglomerado de aço inóxidável, que é descrito pelo modelo modificado elasto-plástico *Drucker/Prager-Cap* desenvolvido para aplicações em pó. O código de elementos finitos com o modelo *Drucker/Prager-Cap* foi usado para modelar os estágios de compressão e descompressão da compactação do pó. Os parametros usados no modelo *Drucker/Prager-Cap* foram obtidos da literatura. Este modelo foi implementado com a sub-rotina UVARM e a densidade relativa no final do estágio de compactação foi previsto. No estágio de sinterização, o objectivo principal é obter um corpo denso. Assim, foi implementado um modelo preciso no programa de simulação numérica que é necessário para representar o processo eficazmente. Os comportamentos de densificação e *Creep* do pó de aço inóxidável foi simulado e o modelo de material foi implementado conectando à sub-rotina *Creep* com o código de elementos finitos Abaqus. Esta abordagem é baseada em teorias contínuas de deformações de elasticas e viscosas não lineares de corpos porosos. A porosidade é actualizada durante a simulação. Crescimento de grão, gravidade, expansão térmica, condutividade térmica e outros factores heterogéneos são também considerados durante a simulação. Aplicação em modelo axissimétricos é feito e o resultado da simulação ao nível da contração volumétrica e a distribuição de densidades são discutidos

Keywords

Powder metallurgy; Compaction; Sintering; Finite Element Method; Elasto-plastic model; Viscoelastic model; User subroutines.

Abstract

Powder metallurgy is a well establish industry in the production of hard metal reference industry amongst metallic components industries. This type of industry has the quality of producing pieces with high complexity through metallic powder. Powder metallurgy, in the many steps that characterizes, there is two major steps: the compaction process and the sintering process. In the compaction process, the major concern is in producing a porous body, the green compact, which mechanic characteristics are the ideal for proceeding to the sintering stage. Therefore, the compaction of metallic powders can be simulated using phenomenological elasto-plastic continuum models adapted from soils mechanics. These models are typically implemented in finite element codes and are used to investigate the macroscopic property distributions in powders during compaction. The present study demonstrates the flow behaviour of a metallic powder, an agglomerated stainless steel, that is described by the modified Drucker-Prager/cap elasto-plasticity model developed for powder applications. A commercial finite element code implementing the Drucker-Prager/Cap model was used to model the compression and decompression stages of powder compaction. The parameters used in the Drucker-Prager/Cap model were obtained from the literature. This model was implemented with a user subroutine UVARM and the relative density at the end of the compaction stage was predicted.

In the sintering stage, the main goal is to obtain a full dense body. Therefore, an implementation of an accurate sintering model into a finite element simulation program is necessary for representing the process efficiency. The densification and creep behaviour of stainless steel powder during free sintering was simulated and the material model was implemented by linking the CREEP subroutine to the Abaqus finite element code. This approach is based upon the continuum theories of elastic and non-linear-viscous deformation of porous bodies. The porosity is updated during the simulation. Grain growth, gravity, thermal expansion, thermal conductivity, and other heterogeneous factors are also considered during the simulation. Application in an axysimmetric model is made and simulation results of axial shrinkage and density distribution is discussed after sintering.

Contents

List of Tables

List of Figures

Part I

Framing and State-of-the-Art

Chapter 1

Introduction

1.1 The Powder Metallurgy Process

From a couple of years to now, powder metallurgy (PM) has become one of the most widely used manufacturing technique in the metallurgy industry. The potential of this manufacturing technique is the possibility to manufacture complex parts with tight tolerances in an economical manner, especially for metals with high melting points and high hardness levels [1].

PM is a processing technique that involves the production of metal powders and conversion of these powders into engineered components. The steps of the typical process involve powder compaction in rigid dies and then heating of the compacted powder to bond the particles together. At the beginning, the powder starts as a fluid-like substance, where it is neither a liquid nor a strict solid [2].

In the compaction stage, the metal powder flows into a die cavity at room temperature and is physically pressed in the die leading to the formation of weak friction bonds between the particles to form a certain shape. Thus, the connection between particles during this stage is frail. The compact is usually very week. At the same time the pressure is applied, the powder in the die undergoes several stages: rearrangement of the particles, elastic deformation, fragmentation (for brittle materials) or strain hardening (for ductile materials) and the deformation [1]. After the compaction stage, the powder takes on the properties of a solid. Although weak after compaction, the solid component can be heated to a temperature where the particles sinter to one another forming strong bonds [2]. This is called the sintering stage, where the compacted powder is put into the furnace and heated to some temperature below the melting point, usually with a holding period. The friction existing between the die wall and the powder and the cross-section variation can causes: density gradients, residual stresses and cracks, which can occur in the green compact [1].

During the sintering stage, particle connection is formed mainly due to the atomic motions that eliminate the high surface energy associated with the powder. Several atomic motion paths have been found and categorized to six mechanisms of mass transportation according to modern sintering theory. Among the mechanisms, the grain boundary diffusion tends to be more important to the densification of most crystalline materials and appears to dominate the densification of many common metal powder systems [1]. These concepts can be found in chapters 3 and 4 for a detailed explanation.

In the solid-state sintering, when the material consolidates, it is inevitable that the part shrinks, from a macroscopic point of view. If the shrinkage is not uniform, the part can suffer distortion. The primary reason for the distortion is that the compact is not a uniform material. This comes from the nonuniform density distributions created during compaction. As a downside to this process of manufacturing components, it has been reported that 50 - 90% of the total component cost is due to extra machining to achieve the net desired shape [1].

In order to avoid an additional stage of hard machining to address the distortion and achieve the desired requirements, the process specification must be tailored to minimize density variation in the compaction stage and to provide controlled/expected shrinkage during the sintering stage [1].

These sintered products have many benefits, among them, they hold the shape imparted by the compaction die, but builds up strength in sintering. Many variants exist to this basic process [2].

Figure 1.1 demonstrates an overall process of powder metallurgy. Of these materials, steels are the dominant metallic species. A few powder metallurgy components are very large, the shapes can range from a simple cylindrical bearing to very complex structures such as hollow golf-club heads and helical seat gears. In this type of industry the tooling cost is substantially high, so, for this reason most PM production is targeted at structures manufactured at high rates (measured typically in parts per year), such as for automobiles, lawnmowers, home appliances, business machines, computers, and other electromechanical structures [2].

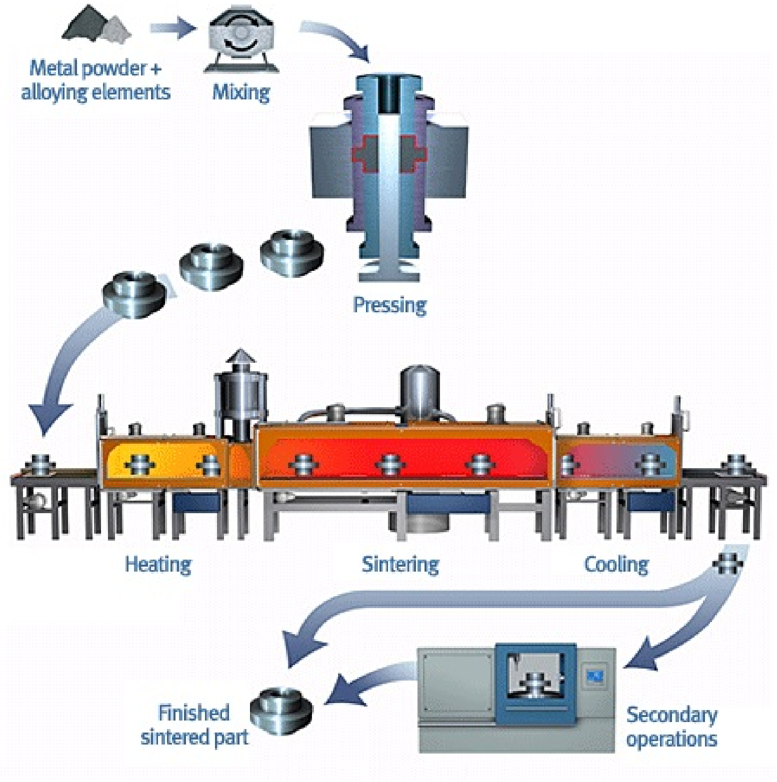

Figure 1.1: The powder metallurgy process [3].

1.2 Historical Perspective

The PM process had several successes in ancient times (probably as early as 3000 BC) with the manufacturing of coins and implements in ancient Egypt, gold-platinum powder compacts by the Incas, an iron pillar in India, copper coins in Germany, and platinum crucibles in the 1800s in England and Russia. The modern era is traced to Coolidge's experiments in the early 1900s (working for Edison) and the production of tungsten lamp filaments for the light bulb, a process that is still used today. By the 1930s several products emerged, including porous bronze bearings, tungsten radiation containers, copper-graphite electrical contacts, cemented carbides for metal cutting, and the first steel mechanical components. By the 1950s the industry became organized and the field emerged as a viable production technology for selected components. Early PM was applied mostly to small stress, moderately complex components as an alternative to machining [2].

By the 1960s, interest in the net-shaping attribute of powder metallurgy emerged. This idea relies on the attainment of final dimensions in the powder forming step, by that avoiding machining. Aerospace uses grew with the development of fully-density fabrication techniques, such as hot isostatic pressing. In the 1970s there emerged recognition of the rapid solidification rates possible in powder atomization, allowing the production of new compositions with novel properties. In more recent years, many new alloys, property combinations, and production technologies have emerged [2].

Nowadays, the PM industry is constituted by many companies, each with specialization in alloys, applications, and productions techniques. The largest activity is associated with ferrous alloys, some iron, and many steels. In spite of the many processes, PM faces many competitors from alternative forming technologies and alternative materials - mainly fine blanked steels, cast steels, die-cast zinc, injection-molded plastics, injection-molded ceramics, extruded aluminum matrix composites, and machined steels [2].

Ferrous alloys constitute the dominant powders, and structural automotive components constitutive the dominant applications. The combination of low production costs and high sintering strength dominates the PM selection criteria. Since high density is a precursor to high strength, the trend is toward higher densities to improve mechanical properties. Production technologies that allow high final densities include high-temperature sintering, powder forging, powder rolling, injection molding, infiltration, hot isostatic compaction, pneumatic forging, and warm compaction [2].

1.3 Overview of Processes and Steps

The PM processes can be divided in two major areas. One area is in injection molding and the other area starts with loose powders. In the powder injection moulding (PIM), the feedstock is sintered to nearly full density at high temperatures. Here, the powder is shaped in the forming step, but not compacted. More importantly, the particles are densified in sintering and not during compaction. The other major area of powder metallurgy is encountered in traditional die compaction, where densification occurs in pressing. Here, sintering has little impact on densification and is largely used to bond the particles. Between these two major areas, various technologies exist where sintering and compaction are combined for densification. Some examples occur in hot pressing, hot isostatic pressing and hot forging. Pressure-based densification depends on lower sintering temperatures, larger particle sizes, and higher forming pressures to densify the powder. Alternatively, sintering-based densification relies on low forming pressures, high sintering temperatures and small powders. The hybrid densification techniques apply simultaneously temperature and pressure to obtain a pore-free product [2].

For example, die compaction compresses the powder to produce a density 2-3 times the initial powder density. Alternatively, injection molding applies a relatively lower pressure that shapes the powder, so, the particles are neither deformed nor densified. These forming steps are characterized by typical stresses or pressures and forming times. Die compaction occurs in roughly one second [2].

With respect to the sintering step, some technologies rely on low temperature to bond the particles, while others rely on high temperatures to densify the structure. Sintering densification results in volume changes, while bonding results only in a strength gain. Again, each process is characterized by a typical temperature and time. Various PM fabrication techniques rely on a combination of pressure and temperature. For example, hot isostatic compaction might involve 200 MPa at 800 °C for one hour to densify a steel powder [2].

1.4 Needs for Research

As have been mentioned in this chapter, sintering process is one of the most powerful techniques to obtain components with high complexity and excellent response in mechanical performance. However, and particularly in complex components, the probability for some imperfections and geometric distortions to appear, from high levels of residual stresses with consequently smooth fractures, is high.

Therefore, numerical methods can be suitable tools to develop specific numeric simulations of the process. As computer technology and numerical algorithms develop rapidly nowadays, numerical tools such as the Finite Element Method (FEM) and Discrete Element Method (DEM) become more popular and powerful. Compared with the empirical optimization (trial and error method), numerical simulation is less expensive and shows a more efficient use time, especially for newly designed products [1].

1.5 Research Objectives

The ambit of this investigation work is to develop some competences in the powder metallurgy simulation area. Therefore, it is necessary to build an accurate numerical model to determine the shape change, *i.e.*, shrinkage and distortion of the compacted powder after the sintering. To reach this objective, it is necessary complete intermediate goals as:

- Capacity in working with some computation tools based on Finite Element Method (FEM) - The entire work is done resorting to a commercial finite element program. Therefore, there is a necessity of developing skills in an appropriated finite element software;

- Capacity in working with mathematical and computation models that describe thermo-mechanical couplings - There is a necessity to work with elasto-plastic model and viscoelastic model for describing the entire process;

- Numerical modelling and simulation of the process of powders' compaction - A elasto-plastic constitutive law is used for describing the deformation of the loose powder.
- Modeling the sintering process based on the continuum mechanics - A viscoelastic constitutive law is used to describe the deformation of the sintering part;
- Numerical simulation of the sintering process based on the FEM - Based on the employed sintering model and identified parameters, numerical simulations are carried out by FEM. The calculated shrinkages and distortions issued from numerical simulations are presented in the final of the sintering stage.

Chapter 2

Powder Compaction

2.1 Introduction to Powder Compaction

Powder metallurgy is a widely used net shape manufacturing technique in the metalworking industry. The most common process of consolidation in powder metallurgy is the uniaxial die compaction. This process consists in compressing loose powders into the die cavity by the application of pressure, forming a solid "green" part of relatively high density that conforms to the shape of the cavity. The pressure is usually applied along one axis into the cavity where the loose powder is pressed in the *y-direction* and has a lateral constrain as shown in figure 2.1. This deformation is defined by a decrease in porosity and an increase in particle bond strength [2]. This process is extremely fast and has a great potential for mass production of parts such as those in the automobile industry [4].

When the pressure required to apply in compaction is higher, higher also, will be the density of the compact. With standard tool steel or cemented carbide dies and punches, densities can theoretically reach up to 90% without tool damage. The compact with a modest density and strength after compaction is fragile and may break upon impact. Therefore needs to be sintered in a furnace with controlled atmosphere at a temperature approximately 80% of the melting temperature of the material, in order to attain the desired strength. During the sintering stage, the powder particles bond together, which can result in dimensional distortion of the compact. It is proven that the dimensional change is inversely proportional to the density of the compact; consequently density gradients in the green part will produce shape distortion [4].

During the compaction process, axial forces applied by the compaction load result in radial forces being generated at the die walls. Between the powder and the tool components there is friction. These frictional forces exist because of the applied pressure along the die wall decreases along the depth of the powder column. Due to a differential and non-uniform pressure distribution during the compaction process, it is produced a density gradient in the green parts. During the entire process of sintering, these densities gradients lead to non-symmetrical dimensional changes. Near the punches faces are located regions of high density that exhibit small dimensional changes, while in regions away from the punch faces have lower density, and for that reason exhibit larger dimensional change. This leads to a loss of dimensional precision on the finished component. The compaction process study is important for ensure uniformity in dimensions and properties after sintering, variations in green density need to be minimized and

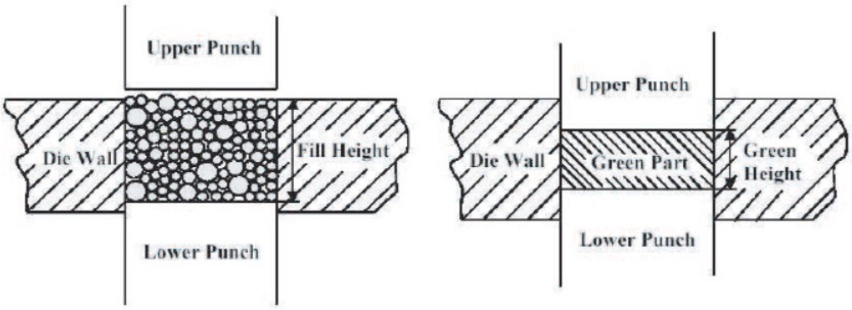

Figure 2.1: Schematic of a uniaxial die compaction process [4].

understood. In order to minimize density gradients is recommended reducing the friction during the compaction phase by adding lubricants in the powder or in the die-wall surface [4].

Many compaction options exist, including hard and soft tooling, heating the die and powder, using rolling mills and even shock waves. Table 2.1 shows a categorization and comparison of compaction options in PM. This table includes the main processing variants that uses different pressures to densify the powder in compaction. Each process associated to the nominal operating parameters, including pressing directions, shape complexity, and relative use. Differences in the compaction pressures and temperature help categorize the options [2].

Table 2.1: Compaction options [2].

Process	Cold Isostatic Compaction	Cold Forging	Die Compaction	Explosive Compaction	Roll Compaction	Warm Compaction
Pressure	Moderate, 400 MPa	Very high, > 800 MPa	High, 700 MPa	Very high, > 1 GPa	Low	High, 700 MPa
Temperature	Ambient	Ambient	Ambient	Very high	Ambient	Warm
Tooling	Soft	Hard	Hard	Soft	Hard	Hard, heated
Deformation Rate	Low	High	High	Very high	Low	High
Continuous	No	No	No	No	Yes	No
Shape complexity	Moderate to high	Moderate	High	Low	Low	Moderate
Precision	Low	Moderate	High	Low	High	High
Use	Moderate	Low	Extensive	Very low	Moderate	Low

2.2 Techniques of Compaction

2.2.1 Die Compaction

Die compaction involves the pressurization of the powder in a rigid tool set. A conceptualization of a die compaction cycle is given by figure 2.2. Powder is loaded into the cavity by gravity from a feed shoe that sweeps over the die opening. A few important features of the tool set become evident: the die body, lower punch, upper punch, and feed shoe. The lower punch is in the fill position during powder entry, but then drops to a lower position to create room for the upper punch to enter the die cavity. In the most common pressing cycle, the two punches work toward the center of the compact to densify the powder: double-action pressing. After application of the peak pressure, the upper punch is pulled from the die while the lower punch pushes the compact out of the die. After this point the cycle repeats [2].

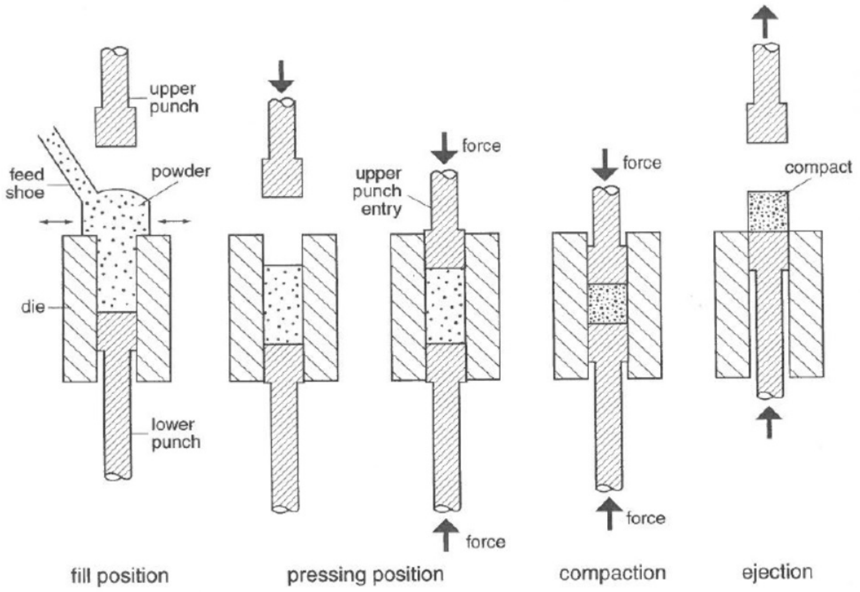

Figure 2.2: Die compaction scheme [2].

2.2.2 Warm Compaction

One way to improve green density of die-compacted powder is to heat the powder before the compaction. Various technologies known as *warm compaction* are emerging to performing simultaneous heating and bonding during pressing. Both the powder and the tooling are heated in warm compaction. A typical temperature for the powder and tooling might be 150 °C, and compaction pressures are usually in the range of 700 MPa. Heating of the die and punches requires modifications to the compaction press, and a heater is required in the powder feed mechanism. Both microwave and hot-oil heaters are available for bringing the powder up to a temperature near 150 °C. Depending on which polymer is selected the ejection forces can be highly variable [2].

2.2.3 Cold Isostatic Compression

Cold isostatic pressing (CIP) is a common process applied in complex shapes involving undercuts or large length/diameter ratios. This process is based on a flexible mould to apply pressure to the powder from all directions. For the CIP process, powder is filled in the flexible tooling and the sealed tooling is pressurized in a vessel filled with a fluid such as oil or water. Lubricants are rarely used. The work pressures in CIP can reach 1400 MPa but usually are performed at below of 420 MPa. During pressurization all seals must be under compression to prevent leakage of the pressurization fluid into the powder. Usually, an external support is needed to help hold the bag shape during powder loading, and in some situations the bag is evacuated to remove air prior compaction [2].

There are two variants of cold isostatic pressing: the wet-bag and the dry-bag techniques. The wet bag (figure 2.3), the filled and sealed mould is immersed into a fluid chamber that is pressurized by an external hydraulic system. This particulate conceptualization would be appropriate for forming a hollow tube by pressing the powder against a solid core. Ceased the compaction process, the wet mould (or bag) is removed from the chamber and compact extracted from the mould [2].

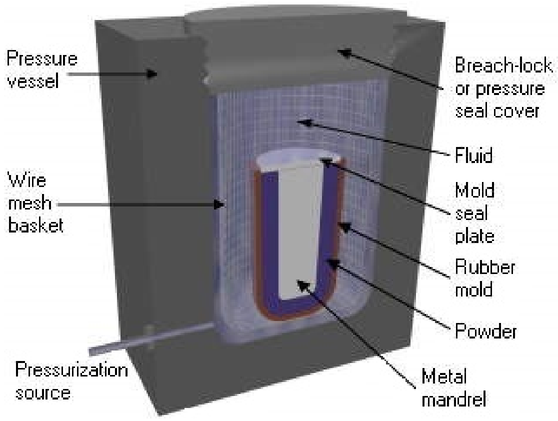

Figure 2.3: Wet bag technique using in CIP [5].

The dry-bag approach has in their benefit the high volume production due to the bag is built directly into the pressure cavity. In this technique, it is known that the flexible bag deforms but is not ejected. Two end plugs allow powder loading and component unloading on each cycle, without removing the bag assembly. Sealing is achieved by an upper punch that enters the bag before pressurization. In that situation, compaction stresses are generated by isostatic compression of the bag through a hydraulic fluid [2].

Isostatic pressurization is useful for making large, thin-wall, long, or homogeneous compacts. Density gradients are small in isostatically compacted components, allowing large sintering shrinkages without distortion. With isostatic compaction, the fluid provides uniform pressures and consequently, uniform density [2].

2.2.4 Powder Rolling

Although die compaction is the most common process, powder rolling can be applied as a first step toward full-density steel sheet. Powder rolling is different from the common powder compaction techniques because it is a continuous process. After the first stage of compaction, in a rolling mill, the powder is not very dense. However, subsequent rolling passes improve density [2].

Loose powder is gravity-fed into the gap between two rolls, which generate the green sheet. Gravity feed is the only effective means to feed powder, since there is no strength to the powder prior to rolling and green densities are very low. Figure 2.4 illustrates a schematic operation. A binder can be added to improve green strength, and water works for some powders. Two forces act on the powder as it is compressed. One is the normal force from the rolls that give compaction, but the other is a tangential force from friction between powder rolling. The compaction force must exceed the friction force in powder rolling. The allowed height reduction depends on the rotation angle from where the powder first contacts the roll to the point at which full compression occurs. For some powders this angle is as small as a few degrees [2].

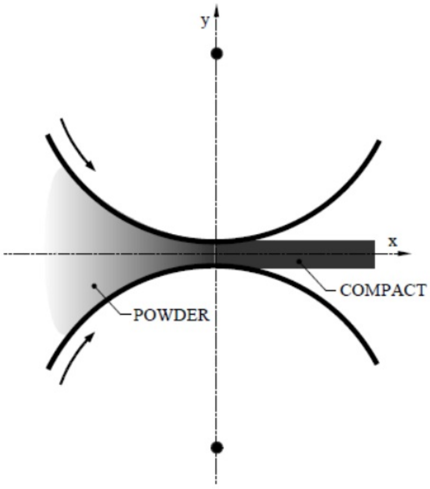

Figure 2.4: Powder rolling technique [6].

The higher the initial powder density and the greater the reduction in thickness on rolling, the higher the final density. However, powders with high apparent densities have less friction and undergo only small thickness reductions in rolling [2].

In a single-pass rolling operation, densities near theoretical have been achieved, but multiple-pass treatments are more common. Obviously, the final product is limited to a sheet form. In the green state, the rolled powder is too weak to be coiled, so immediate sintering is necessary. After the first sinter, repeated rolling and annealing allows fabrication of a full-density strip [2].

2.3 Phenomenological Compaction Models

The phenomenological compaction models, originally developed for soils mechanics, are usually incremental continuum plasticity models (sometimes also called critical-state models) characterized by a yield criterion, an isotropic (or kinematic) hardening function and a flow rule. The latter is often considered as of associative that means the yield surface and the plastic potential surface are coincident and, as a consequence, the plastic strain increment is normal to the yield surface.

There are a large number of constitutive models for simulation of compaction, among them the "cap" model and the Cam-Clay model. Not all can be described here, the description in section 2.3.1 focus on the most widely used model of phenomenological compaction models, namely the Drucker-Prager/"Cap" model.

2.3.1 The Drucker-Prager Soil Plasticity Model

The original Drucker-Prager soil plasticity model was developed by Drucker and Prager in 1952. The main purpose of the model, was to modify the von Mises yield criterion in metal plasticity to study the bearing capacity of soil foundations. While the metal plasticity models are independent of the first stress invariant, particulate materials exhibit the type of behaviour characterized by frictional materials in that the strength of these materials depends on hydrostatic stress. In the Drucker-Prager soil plasticity model is assumed that the material will behave elastically up at some point of stress at which yielding occurs. The shear stress necessary for yielding occurs depends in factors like the cohesion of the material and the normal pressure on the failure surface [4].

The original Drucker-Prager yield criterion modified the von Mises yield criterion by introducing a dependence on the mean (hydrostatic) stress, p. The Drucker-Prager yield function is given by:

$$f(J_1, J_{2D}) = \sqrt{J_{2D}} - \alpha_1 J_1 - k = 0, \tag{2.1}$$

where parameter J_1 is the first stress invariant ($J_1 = \sigma_{ii} = \sigma_1 + \sigma_2 + \sigma_3$), J_{2D} is the second invariant of the deviatoric stress, s_{ij} $\left(J_{2D} = \frac{1}{2} s_{ij} s_{ij}\right)$, and α_1 and k are positive material constants [4].

The parameter α_1 allows modify the von Mises yield surface (which is plotted in the principal stress space) from an infinitely long cylinder to a cone. This is why the criterion is also called the extended von Mises criterion. When α_1 is major than zero, the Drucker-Prager yield surface is a right circular cone with its axis equally inclined to the co-ordinate axes and its apex in the tension octant in the principal stress space. The failure surface defined by the Drucker-Prager failure criterion in the principal stress space and the meridional ($p - q$) plane is demonstrated in figures 2.5 and 2.6. In the meridional plane is shown that the parameters α_1 and k denote the angle of internal friction and cohesion respectively [4].

In the original proposed Drucker-Prager, the failure surface is the straight edge of a right circular cone, but some researchers have proposed that at higher stresses, the particulate system behaves as a liquid and its strength approaches the von Mises surface at these stresses. Therefore, the failure surface can be composed by an initial portion of the Drucker-Prager and then involves smoothly the subsequent von Mises surface that prescribes the strength of the material at 100% relative density as shown in figure 2.7 [2].

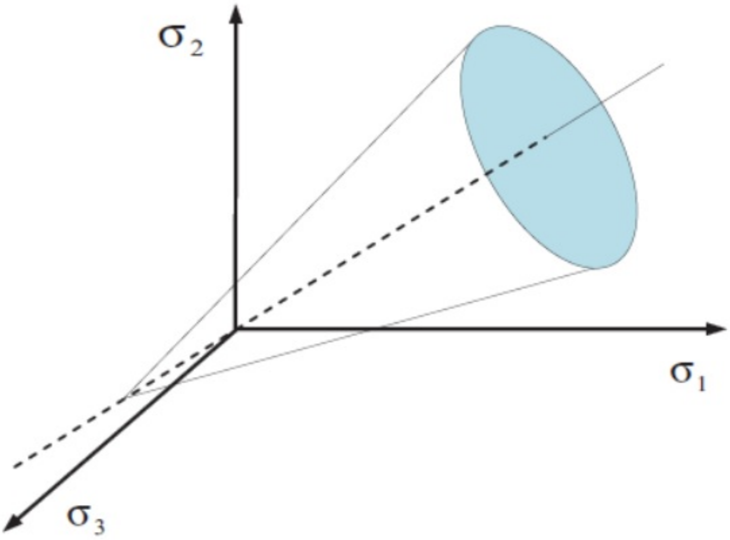

Figure 2.5: Principal stress space [4].

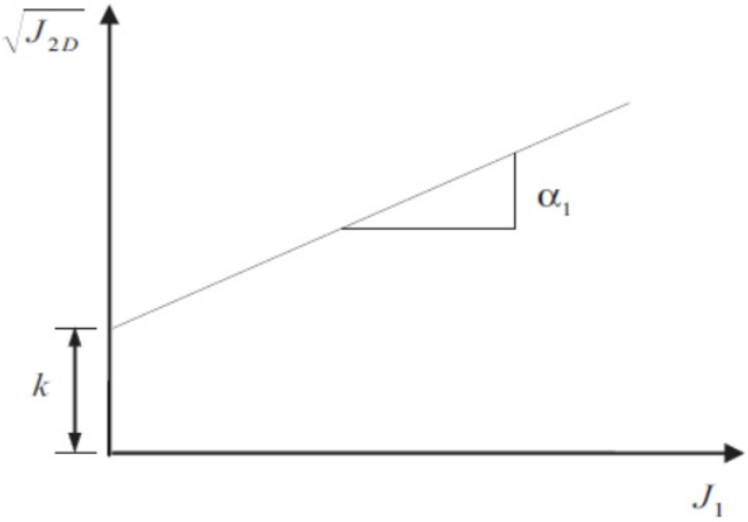

Figure 2.6: Meridional plane [4].

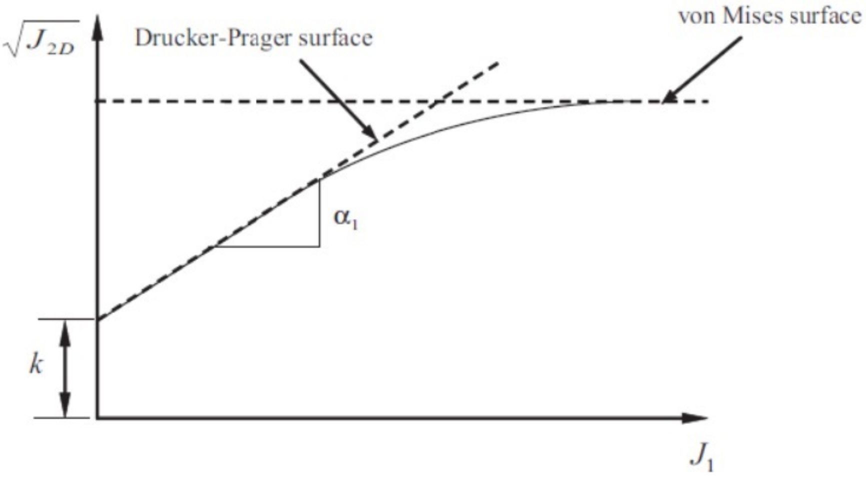

Figure 2.7: Proposed Drucker-Prager failure surface for higher stresses [4].

2.3.2 Flow Rule

When the state of stress reaches the yield criterion, the material undergoes plastic deformation. For define the direction of the plastic strain vector, is established a flow rule. Q is a constant called plastic potential function that is assumed to exist and the incremental strain vectors are assumed to be orthogonal to this function as given:

$$\mathrm{d}\varepsilon_{\mathrm{ij}}^{\mathrm{pl}} = \lambda \frac{\partial Q}{\partial \sigma_{\mathrm{ij}}}, \tag{2.2}$$

where the parameter λ is a positive factor of proportionality [4]. This expression is referred as the normality rule. In some cases, for several materials, the plastic potential function is assumed to be equal to the yield function. Such materials are said to follow the associative flow rule of plasticity. Substituting the expression for the yield function demonstrated at 2.1 in the normality rule 2.2, the new relation is given as:

$$\mathrm{d}\varepsilon_{\mathrm{ij}}^{\mathrm{pl}} = \lambda \left(\frac{S_{\mathrm{ij}}}{2\sqrt{J_{2D}}} - \alpha_1 \delta_{\mathrm{ij}} \right), \tag{2.3}$$

where S_{ij} is the deviatoric stress tensor [4]. From equation 2.3, it is noted that the plastic rate of a cubical dilation is given by:

$$\mathrm{d}\varepsilon_{\mathrm{ii}}^{\mathrm{pl}} = -3\alpha_1 \lambda. \tag{2.4}$$

As noted before, the volumetric component is negative indicating the shear failure along the Drucker-Prager failure surface is accompanied by volume increase or dilation. However resorting to experimental data, it was concluded that in particulate materials the dilation predicted by the Drucker-Prager model is usually larger than that found in practice. For some materials, the deformation occurs at constant volume or is accompanied by a decrease in volume. This discrepancy may be due to an invalid assumption of the normality rule. Although discarding, the normality rule would imply a material that violates the stability postulates by Drucker (1950). Another consideration, for explain the discrepancy could be due to the particulate material may not behave as a perfectly plastic body, an underling assumption of the failure surface definition. With all these presumptions and considerations it was presented the basis of the modified Drucker-Prager yield criterion with suggests treating the particulate material system as a work-hardening material which could reach the perfectly plastic state [4].

2.3.3 Work Hardening and Its Implications

In this section, the concept of work hardening is introduced for explaining the behaviour of material under plastic loading beyond its yield criterion but prior to failure. If an external agent causes added stresses on a body, work hardening of the material ensures that the material remains in stable equilibrium by absorbing the work done by these added stresses on the strains that result. The work hardening is based on two postulates [4]:

1. During the application of stresses, the work done by the external agency will be positive. This is expressed mathematically as:

$$\mathrm{d}\sigma_{\mathrm{ij}}\mathrm{d}\varepsilon_{\mathrm{ij}} > 0. \tag{2.5}$$

2. Over a cycle of application and removal of stresses, the work done by the external agency will be zero or positive. This is expressed as:

$$\mathrm{d}\sigma_{\mathrm{ij}}\mathrm{d}\varepsilon_{\mathrm{ij}}^{\mathrm{pl}} \geq 0. \tag{2.6}$$

Certain conditions need to be satisfied to grant an appropriate description of the physical process involving plastic deformation for contemplate the conceit of work hardening. These conditions were formulated by Prager (1949) and are [4]:

1. *Condition of continuity*: Given a state of stress that is on the yield surface, an infinitesimal change of stress $\mathrm{d}\sigma_{\mathrm{ij}}$ causes unloading if the stress path is directed for the interior of the surface and loading if the path is direct for the exterior of the surface and for last, neutral loading if the stress path is tangential to the yield surface. The condition of continuity states that neutral loading does not cause any plsatic deformation.

2. *Condition of uniqueness*: This conditions denotes that for a given state of a material and a system of infinitesimal increments of surface tractions, the resulting increments of stresses and strains are unique.

3. *Condition of irreversibility*: This condition relates that plastic deformation are irreversible, this condition states that the work done on plastic deformation will be positive.

4. *Condition of consistency*: This condition determines that the yield condition is satisfied as long the material stays in plastic state.

Considering the postulates and conditions mentioned above, is possible to study what the implications of assuming a work hardening material are on yield surface. Suppose that there is a stress state σ situated on the yield surface. Consider an infinitesimal increment in stress dσ whose stress path is directed towards the exterior of the yield surface as shown in figure 2.8. The incremental stress can be divided into two components: a tangential component d$\sigma^{(\mathrm{t})}$ and a normal component d$\sigma^{(\mathrm{n})}$ [4].

Assuming that the relation between the infinitesimal changes of stress and plastic strain is linear, the incremental plastic strain caused by dσ will be equal to the vector sum of the incremental plastic strains caused individually by d$\sigma^{(\mathrm{t})}$ and d$\sigma^{(\mathrm{n})}$. By imposing the condition of continuity that requires the plastic strain due to neutral (or tangential) loading to be zero, is founded that the incremental plastic strain d$\varepsilon^{\mathrm{pl}}$ due to dσ is dependent only on the normal component d$\sigma^{(\mathrm{n})}$. This leaves to the normality rule i.e the incremental strain vector is normal to the yield surface. Thus, it is concluded for a work hardened, the yield function follows the normality rule and ensures that the material is stable [4].

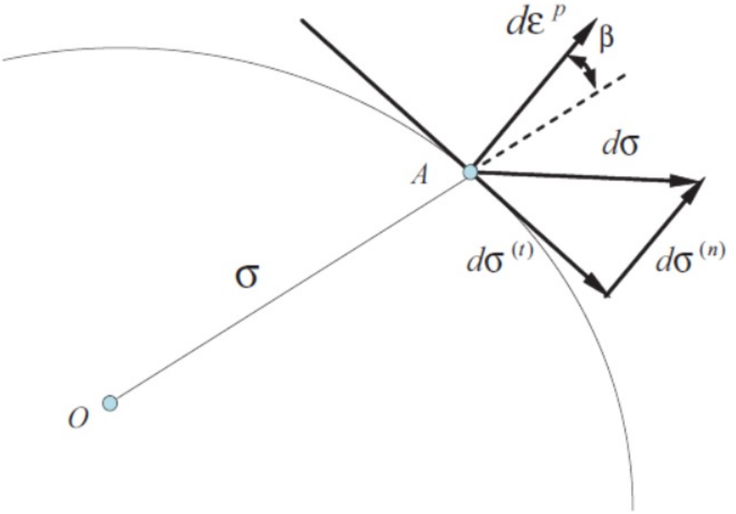

Figure 2.8: Implication of work hardening [4].

Another topic of the condition of irreversibility is that the work done due to plastic deformation is positive which is expressed as:

$$\sigma \cdot \mathrm{d}\varepsilon^{\mathrm{pl}} > 0 \tag{2.7}$$

or

$$\mid \sigma \mid \cdot \mid \mathrm{d}\varepsilon^{\mathrm{pl}} \mid \cos\beta > 0. \tag{2.8}$$

With this, it is concluded that the radius vector should make an acute angle β with the incremental plastic strain vector. Although from the previous explanation, was seen it that the incremental plastic strain vector is normal to the yield surface. Thus, the concept of work hardening and the condition of irreversibility requires the radius vector to make an accurate angle with an exterior normal to the yield surface. That is the yield surface has to be convex. As a objective to describe the behaviour of particulate material as a work hardening material, Drucker and co-Workers defined a series of spherical yield surfaces, the simplest convex surface possible. This concept of successive yield surfaces can explain the hardening or consolidation behaviour of particulate materials and allow the use of the normality rule of plasticity [4].

2.3.4 A Modified Drucker-Prager/Cap Model

The most used constitutive model in finite element simulation of compaction powder is the so called cap model. The various cap models developed differ by the functional form yield surface but they all have some kind of cap describing the hardening part. The cap model first proposed by Drucker and co-Workers assumed the particulate material to behave as a work hardening material that may approach the idealized perfectly plastic state. It is considered the fact that many particulate materials experience the plastic deformation even before reaching the ultimate failure state defined by the Drucker-Prager shear failure surface. This criterion also considers plastic deformations under pure hydrostatic loading. In their work, Drucker presented the criterion proposing the yield curve being described by two straight lines that Drucker-Prager called the lines of the failure criterion given by equation 2.1 and a circular arc closure corresponding to placing a spherical cap on the open end of the cone as shown in figure 2.9. The spherical yield surface changes with the hydrostatic pressure to describe work hardening [4].

If the material is consolidate hydrostatically up to state of the stress A and then unloaded, so, the material will behave elastically until to state A and then start experiencing plastic deformations. During successive yielding, the material hardens. When the stress point moves further the current yield surface as A, a new one yield surface is established at B. The region in which the material now behaves elastically will incorporate the sector OBD. The new yield surface at B intersects the Drucker-Prager failure surface at D. The experimentally observed volumetric behaviour of particulate materials can be explained by assuming the incremental plastic strain vector to be normal to the cap surface at its point of intersection. In addition, the incremental plastic strain vector needs to be normal to the hydrostatic axis at the point of intersection to ensure that no hardening takes place when the state of stress reaches a point on the yield surface that is locally parallel to the hydrostatic axis since no plastic volumetric changes occur at such a point. This is equal to the critical state concept where the material does not change in volume when reaches the critical state. For guaranteeing that no shear deformations take place under pure hydrostatic compression, the cap surfaces intersects the hydrostatic axis at right angles [4].

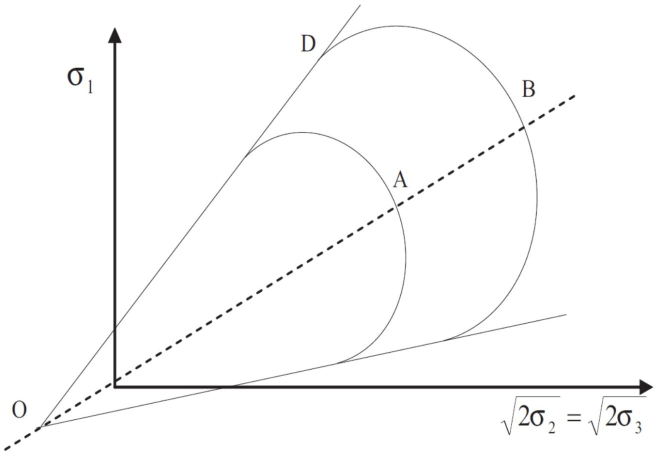

Figure 2.9: Drucker-Prager cap yield surfaces [4].

Drucker and co-Workers proposed a spherical yield surface, the simplest convex yield surface as required from the concept of work hardening. For different researchers, the shape of these yield surfaces has been assumed to be different. The shape of the yield surface needs be determined from appropriate laboratory tests. Many caps models were suggested all over the years by DiMaggio and Sandler (1971) and Lade (1977) where suggests a series of elliptical yield surfaces. A yield function given by Chen (1994) is a simple elliptical yield function referred to as the modified Drucker-Prager yield function and is expressed in equation 2.9 [4].

$$f(J_1, J_{2D}, k_1) = (J_1 - l)^2 + R^2 J_{2D} - (x(k_1) - l)^2 = 0 \tag{2.9}$$

The parameter R represents the aspect ratio of the ellipse, l is the location of the intersection of the Drucker-Prager surface and the cap, and x is a hardening parameter and a function of k_1 that defines the deformation history. This parameter k_1 is usually taken as the volumetric plastic strain [4].

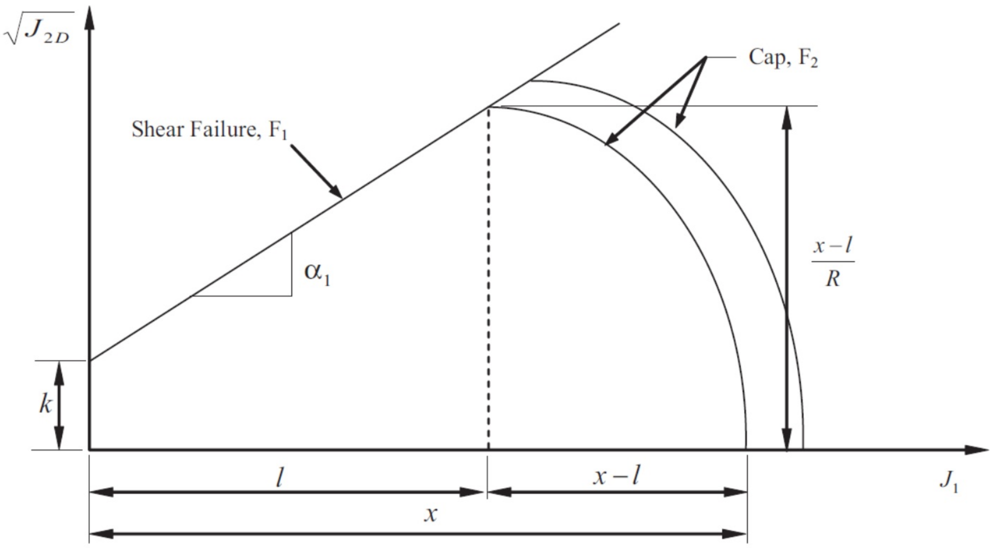

Figure 2.10: Modified Drucker-Prager cap model [4].

The hardening parameter that defines the yield surface represent a locus of points with the same volumetric plastic strains. A series of cap yield surfaces defined by equation 2.9 are shown in figure 2.10 that intersect Drucker-Prager failure surface as per the assumptions [4].

2.3.5 Constitutive Model Parameters

In some commercial finite element programs the modified Drucker-Prager model is defined by three principal segments: a pressure-dependent Drucker-Prager shear failure surface F_s, a series of compression yield surface F_c and a transition surface F_t like will be described in section 6.4. With variation the cap along the hydrostatic axis it is defined the volumetric strain hardening. The purpose of the transition surface is to remove any singularities during numerical computations when moving from the yield surface to the failure surface. The surfaces defined by the cap model described in ABAQUS in the $p-q$ or $(J_1/3-\sqrt{3J_2})$ plane is shown in figure 2.10 [4].

The hardening law is characterized by a piecewise linear function describing the hydrostatic yield surface p_b to the volumetric plastic strain $\varepsilon_{\text{pl}}^{\text{vol}}$ as shown in figure 2.16, $\varepsilon_{\text{pl}}^{\text{vol}}$ is the initial volumetric plastic strain beyond which the work hardening yield surfaces are defined [4].

The evolution parameter, p_a is related to p_b by equation 2.12 [4].

Cap Model Parameters

The Drucker-Prager/Cap model parameters can be characterized by identifying two different aspects on the cap:

•The plasticity parameters that describe the shape of the shear failure surface and the yield caps. Moreover, the plasticity parameters can be differentiated into two categories:

- *Failure surface parameters*: These group of parameters responsible to define the shape of the shear failure surface. These two failure surfaces parameters are the material cohesion or the intercept of the failure surface with the deviatoric stress axis, d, and the angle of internal friction or the slope of the failure surface with the hydrostatic axis, β.
- *Yield surface parameters*: These parameters define the location and shape of the yield caps or loci of constant volumetric strain. The yield surface parameters comprise the aspect ratio of the elliptic caps, R, and the location of the intersection of the cap surface with the shear failure surface.

•The work hardening parameters that describe the evolution of the yield caps with compaction. The location of intersection of the cap surface with the hydrostatic axis is prescribed by defining the work hardening parameter in terms of pairs of the hydrostatic compression yield stress, p_b, and volumetric plastic strain during the consolidation process, $\varepsilon_{\text{vol}}^{\text{pl}}$.

The parameters are determined by doing some tests in a specimen made of a desired material. Usually, the specimen is subjected to leading condition that would ensure that the material is loaded to failure under shear as it undergoes compaction [4].

Failure Surface Parameters

The failure surface parameters can be determined by performing a set of two or more triaxial compression tests. These tests are made for determine the strength and the stress-strain relationships of a cylindrical specimen made of particulate material. At a constant rate of axial deformation the specimen are isotropically consolidated and sheared in compression. Figure 2.11 shows a schematic of the triaxial test equipment [2].

The test apparatus consists of an axial loading device capable of providing a certain prescribed rate of axial strain on the specimen resorting to a piston. An axial measuring device incorporates the test apparatus. To measure the vertical deformation, a deformation indicator is used for measure the displacement of the piston. A triaxial compression chamber consists in a top and a base plate separated by a cylindrical pressure vessel that is used to house the cylindrical specimen during tests. The chamber is constructed of any material capable of pressure controlling and measuring devices as well as a volume measuring device to measure the volumetric strain [4].

For the specimen reach the equilibrium at the effective consolidation pressure, the test starts with the consolidation phase. The axial load piston is pull down and brought in contact with the specimen and the reading of the deformation indicator is recorded. After recording, the piston is raised a small distance and locked in place. The chamber pressure is then increased unit it reaches the desired effective consolidation. The specimen is then allowed and the volume readings are recorded at increasing intervals of time. The piston begins the contact with the specimen cap, after a initial holding time period and then axial deformation is obtained along with the volume readings for the time increments. Consolidation is allowed to continue for at least one overnight period after 100% primary consolidation has been achieved [4].

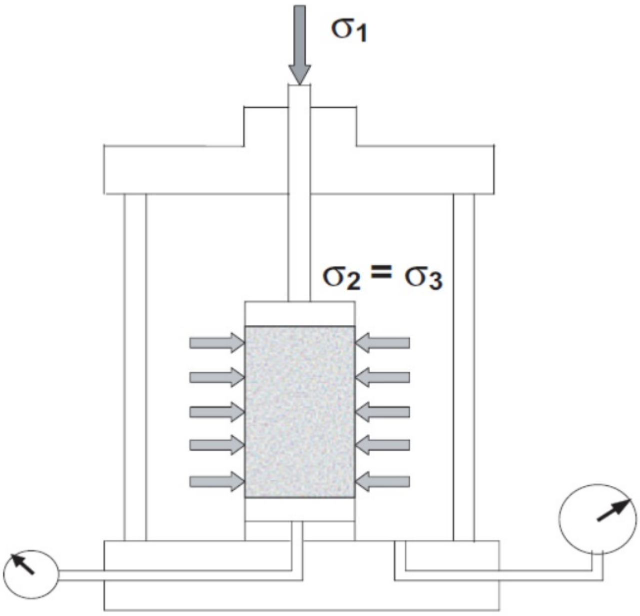

Figure 2.11: Schematic of triaxial test apparatus [4].

After the specimen be consolidated is then axially loaded at a constant confining pressure to cause shear failure. The axial load piston is brought in contact with the specimen and proper seating and alignment of the specimen with the piston is verified to prevent the applications of a lateral force on the piston. The specimen undergoes to an axial load at a desired rate of axial strain. The load and the deformation of the specimen is recorded at increments of strain to define the stress-strain curve until the material undergoes shear. Finished all this procedure the axial load is removed and the pressure in the triaxial chamber is reduced to zero. The specimen is removed from the chamber and its size is measured [4].

With the objective to plot the shear failure line, a minimum of two triaxial compression tests (i.e tests at two consolidation pressures) are sufficient. For get a better fit and reduce errors, the test is carried out at more than two consolidation pressures. Figure 2.12 shows the typical results plotted from a triaxial test at different consolidation pressures ($\sigma_3 = A, B, C, D, ...$) in order to the deviatoric stress against axial strain, ε_1, and also the shear failure surface plotted in the meridional plane by determining the failure stresses [4].

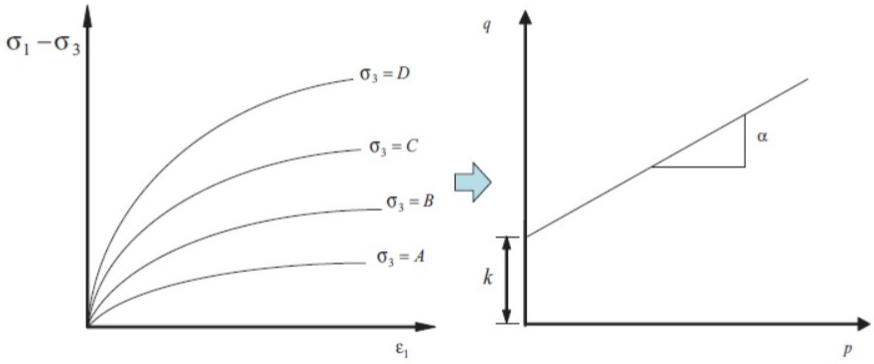

Figure 2.12: Results of a set of triaxial compression tests [4].

Yield Surface Parameters

The cap eccentricity parameter is determined resorting to a true axial compression test. It allows for the application of different stresses in the three orthogonal directions allowing for any loading path to be followed in the three-dimensional stress space. No standard exists for the true triaxial compression test. The parameter can be determined by using a cylindrical triaxial compression test. With this test can carefully obtain different loading paths leading to consolidation without shear the specimen. For realize these triaxial tests is recommended use a cubical triaxial tester that allows for independent normal loading to be applied in the three principal directions. In figure 2.13 it is shown a schematic of a true triaxial test loading condition for a cubical triaxial tester [4].

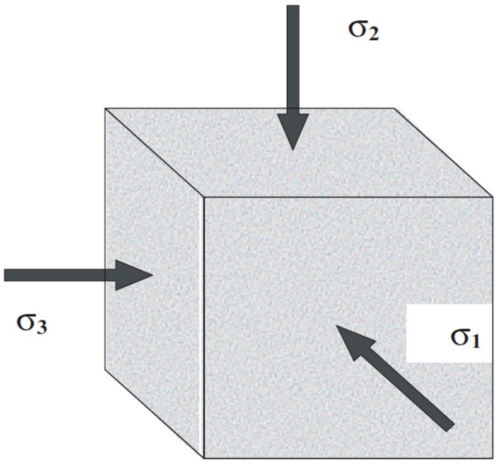

Figure 2.13: Schematic of a true triaxial test loading for cubical specimen [4].

The specimen powder is loaded into a flexible powder. The test is done considering applications of different stresses in the three orthogonal directions to allow consolidation of the specimen without shear. The three resulting principal stresses and the three principal logarithmic strain are measured during consolidation. During the consolidation the bulk densities and the corresponding stress states are calculated. The initial mass powder placed into the cavity is known, so it is easily to calculate the relative density at any deformation state. For each value of ρ obtained from the different stress states, the equivalent pressure stress, p and deviatoric stress measure, q, are calculated as in expressions 2.10 and 2.11 [4].

$$p = -\frac{1}{3}\left(\sigma_1 + \sigma_2 + \sigma_3\right) \tag{2.10}$$

$$q = \sqrt{\frac{1}{2}\left[\left(\sigma_1 - \sigma_2\right)^2 + \left(\sigma_2 - \sigma_3\right)^2 + \left(\sigma_1 - \sigma_3\right)^2\right]} \tag{2.11}$$

Values for p-q at different densities are plotted by using all the stress-strain curves obtained from the triaxial compression experiments. Thus, is possible to get yield surfaces or loci of constant volumetric strain (iso-density curves) as shown in figure 2.14. The cap eccentricity parameter can be predicted by the aspect ratio of the best fit ellipse through these points.

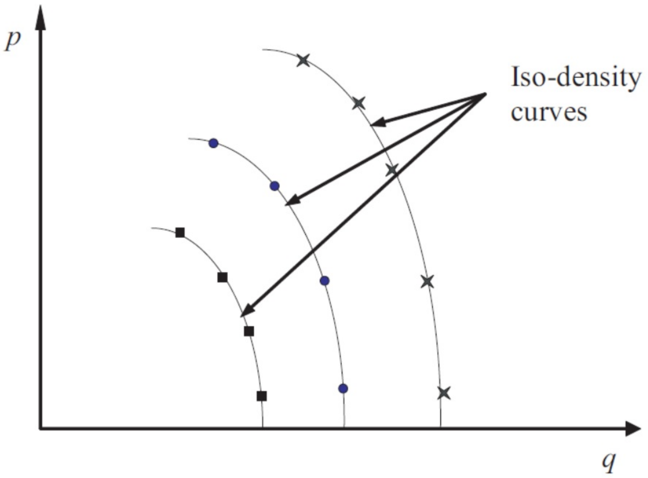

Figure 2.14: Iso-density curve representing Drucker-Prager yield caps in the $p-q$ plane [4].

Hardening Parameter

The hardening parameter is applied in Drucker-Prager/cap model for define the hardening law or the evolution of yield surfaces (caps) with increasing volumetric strains. The yield surfaces are loci of constant volumetric strain. The hardening law is defined by a piecewise function relating the hydrostatic compression yield stress i.e, the intersection of the yield surface with the hydrostatic axis, p_b, and the volumetric plastic strain, $\varepsilon_{\text{vol}}^{\text{pl}}$. The hardening law is usually determined by a hydrostatic compression test (also known as isotropic triaxial compression test). In this test the specimen is consolidated by loading it on a stress path along the space diagonal in the principal stress space with no shear [4].

The hydrostatic compression test starts with the specimen at a initial isotropic state of stress, ($p_0 = \sigma_0$). The physical state corresponding at the beginning of the hydrostatic compression is defined by the initial relative density, ρ_0. Next, the specimen begins consolidation by loading it in increments of hydrostatic stress, i.e., by applying equal increments of stress in the three orthogonal directions in a cubical triaxial tester. For calculate the mean (hydrostatic) stress it is considered to measure the stress applied on each face of the cubical triaxial tester. The elastic strain is measured at each increment of the hydrostatic stress and is the sum of the three principal strains. Typically in this type of testes the specimen is unload at various intervals during the test in order to obtain the bulk modulus for describing the elastic behaviour of the material. Then, a graph can be plotted for describe the variation of hydrostatic stress with volumetric strain as shown in figure 2.15. In this figure for example, the plot indicates that the specimen was unloaded twice during the test. The hardening law can then be defined as a piecewise function of the volumetric strain by fitting a function to the plotted data as shown in figure 2.16 [4].

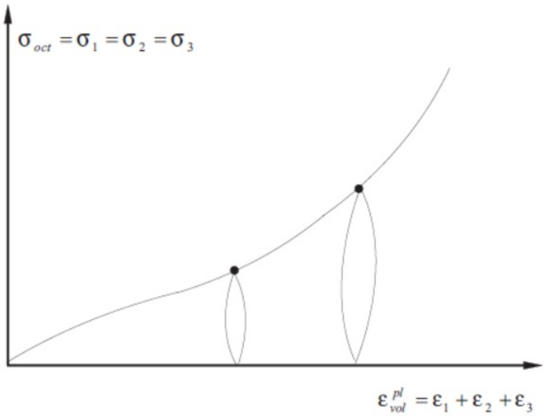

Figure 2.15: Hydrostatic stress versus volumetric strain [4].

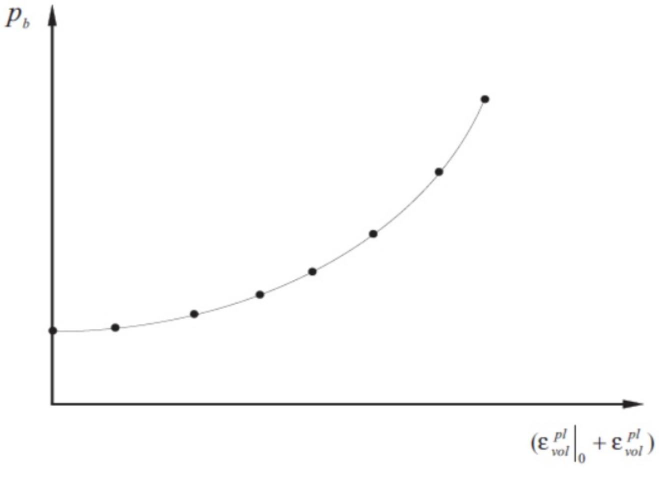

Figure 2.16: Hardening law [4].

Loading material with high strength, hydrostatically can be very difficult and the set-up expensive. Alternatively, it was adopted to test the material in a rigid die under compaction loads for determine the hardening law. Figure 2.17 shows a schematic of a uniaxial die pressing set-up. The set-up consists of an axial loading punch with pressure transducers mounted on it to measure the axial stress. Displacement transducers measure the longitudinal displacement and hence the axial strain or relative bulk density of the specimen [4].

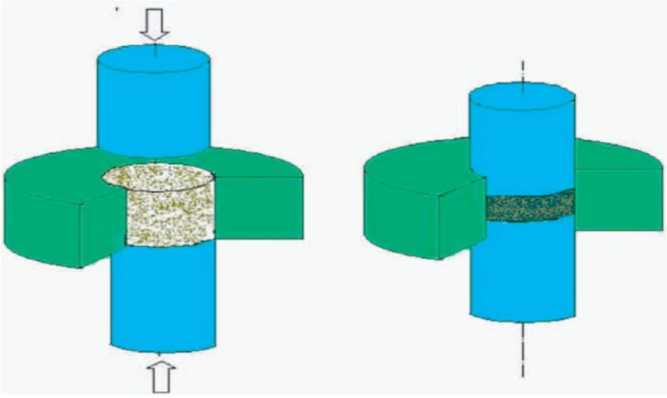

Figure 2.17: Schematic of a uniaxial die pressing experiment [4].

The die is considered be a rigid body, thus, the radial strain is assumed to be zero and the plastic volumetric strain is assumed to be approximately equal to the total volumetric strain since the elastic part of the volumetric strain is very small for high strength particulate material. The effect of friction can be minimize by choosing appropriate lubricants at the die wall or admixed with particulate material. When the specimen particulate material is loaded axially is measured, at the same time, the axial stress and the displacement for reunion data to give a plot of relative density versus axial stress. The hydrostatic compression stress, p_b, is associated to the axial stress, σ_z, by the expression in 2.12 given by [4]:

$$p_b = \frac{(1 + R.\tan\beta)\,\sigma_z}{1 + R.\tan\beta\sqrt{1 + \left(\frac{2}{3R}\right)^2}}. \tag{2.12}$$

The volumetric strain is derived from the relative density, ρ, as is shown in relation 2.13 [4].

$$\varepsilon_{vol}^{pl} = ln\left(\frac{\rho}{\rho_0}\right) \tag{2.13}$$

Chapter 3

Sintering

3.1 Introduction

The working definition of sintering follows: *Sintering is a thermal treatment for bonding particles into a coherent, predominantly solid structure via mass transport events than often occur on the atomic scale. The bonding leads to improved strength and a lower system energy* [7].

Sintering is a processing technique used to produce density-controlled materials and components from metal or/and ceramic powders by applying thermal energy. The sintering process is a widely used processing technology in powder metallurgy and ceramics industries [8]. During the sintering the green body undergoes the shrinkage in dimensions and then final high dense or full dense product is obtained [9]. Figure 3.1 shows the general fabrication pattern of sintered part and in this specific chapter it will be focus around the box named sintering.

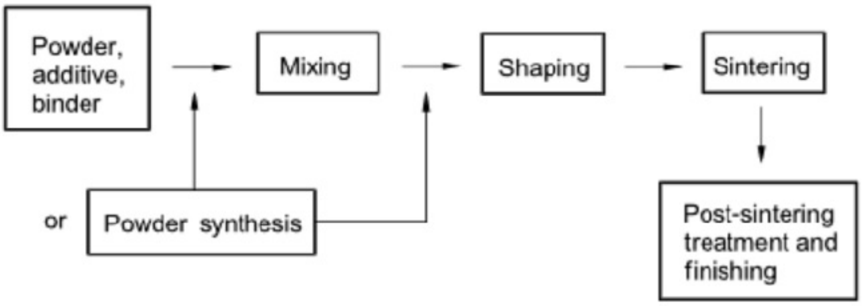

Figure 3.1: General fabrication pattern of sintered parts [9].

Sintering mechanisms can be divided into several types by means of mass transport mechanisms largely occurring at the atomic level. Most polycrystalline materials are sintered through solid-state diffusion that falls into solid-state sintering. Most sintering cycles generate a transient liquid phase that can improve the mass transport rate. It is called liquid-state sintering. For amorphous materials, viscous flow is the main mass transport mechanism during the process considered as viscous sintering [9].

Sintering aims is, in general, to produce sintered parts with reproducible and if possible, designed microstructure through control of sintering variables. Microstructural control means the control of grain size, sintered density, and size and distribution of other phases including pores. In most cases, the final goal of microstructural control is to prepare a fully dense body with a fine grain structure [9].

3.2 Definitions and Nomeclature

3.2.1 Density and Porosity

Density is the most widely reported property in sintering. It relates to the sintering kinetics and correlates with many properties of sintered materials. The density (ρ) is the mass per unit volume, which is called the absolute density (Mg/m^3 or g/cm^3). Here, the concern is lead with the fractional or percentage density that gives evidence of fundamental events occurring during sintering, independent of the material. It is defined as the measured density divided by the theoretical density. In fact, when work with powder structures, the compact density is often expressed as a fractional of percentage of theoretical solid density, designated V_s for the volume fraction of solid phase; thus $V_\mathrm{s} = \rho/\rho_\mathrm{T}$, where ρ_T is the theoretical density for the material. Alternatively, the volume fraction of porosity V_p is the fractional void space in the compact, where $V_\mathrm{p} = (1-\rho)/\rho_\mathrm{T}$. By definition the fractional porosity equal unit, as given by [7]:

$$V_\mathrm{p} + V_\mathrm{s} = 1. \tag{3.1}$$

The green density refers to the before sintering, so the green porosity is the void space prior to sintering. Theoretical density corresponds to the pore-free solid sintering [7].

Pores are an inherent part of sintering. They are present in the powder compact as interparticle voids. The pores space is characterized by its amount, size, shape, and distribution throughout the compact. As the particles sinter, often the compacts densify and reduce the pore size [7].

Porosity, a gross measure of the pore structure, gives the fraction of the total volume that is void. It is expressed as either a percentage or fraction of the total volume [7].

3.2.2 Shrinkage and Swelling

The dimensional change in a powder compact is one of the most widely applied sintering monitors. Shrinkage refers to a decrease in linear dimensions, and swelling refers to an increase in dimensions. Although in many situations sintering is intentionally performed to bond particles without significant dimensional change, there are a great many situations that exhibit shrinkage or swelling. In such situations there is considerable concern with controlling shrinkage or swelling to obtain the desired final dimensions [7].

Formally, the linear dimensional change is defined as $\Delta L/L_0$, reflecting the change in an initial green length L_0 to a final sintered length L_s given as ΔL. If the dimension is larger after sintering, the process termed swelling and $\Delta L/L_0$ is positive, while if the dimension is smaller after sintering the process is termed shrinking and $\Delta L/L_0$ is negative [7].

3.2.3 Coarsening and Densification

Many materials form sinter bonds between particles without densification. This is usually due to transport from surface sites to surface sites by surface diffusion or evaporation-condensation. Even thought there is no net dimensional change, there is considerable reduction of surface area, increase in grain size, and compact strengthening, with attendant changes in the pore size and shape. These are termed coarsening events and are best monitored by surface area, grain size, or pore size parameters. Coarsening processes also consume the surface energy that is responsible for densification, but do not reduce pore space. In these situations densification requires manipulation to minimize coarsening. It is common to observe sintering with simultaneous densification and coarsening. There are sintered products where lack of densification is desirable. Alternatively, densification is desirable in many structural materials. During coarsening the pores grow while during densification the pores shrink. In many cases this mixture of densification and coarsening leads to growth of the large pores and shrinkage of the smaller pores [7]. Figure 3.5 illustrates the scenario that it is possible for both coarsening and densification effects to exist.

3.2.4 Sintering stress

The Laplace equation expresses the stress σ associated with a curved surface as:

$$\sigma = \gamma \left(\frac{1}{R_1} + \frac{1}{R_2} \right), \tag{3.2}$$

where γ is the surface energy, and R_1 and R_2 are the principal radii of curvature for the surface. Figure 3.2 illustrates a general point on a curved surface and the two radii R_1 and R_2. A flat surface is stress free. During sintering, any surface with a bump, or dip, will tend to flatten over time to remove the stress [7].

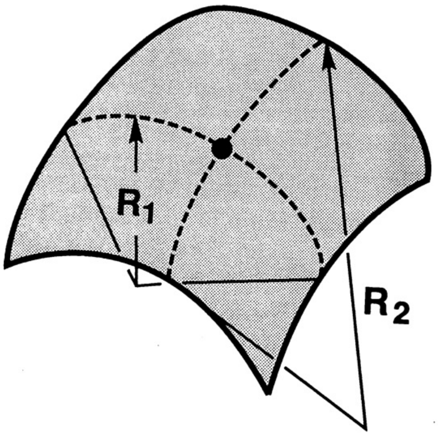

Figure 3.2: Curvature at any point on a curved surface is given in terms of the two principal radii R_1 and R_2 [7].

As an example of Laplace equation usage, consider the initial sintering of two spheres. The neck region can be simplified as drawn in figure 3.3. A free surface is characterized by disrupted atomic bonding, which is the source of the surface energy, and the grain boundary also a defective region (which is the source of the grain boundary energy). Initial atomic bounding in the neck region is highly disrupted. Along the surface away from the neck, the curvature is constant, with both R_1 and R_2 equal to the sphere radius, $D/2$. From equation 3.3.

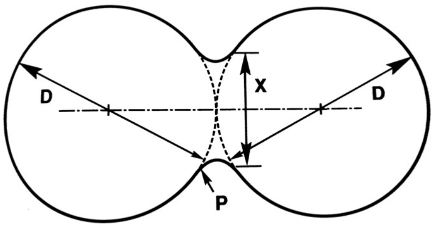

Figure 3.3: Sintering profile for two spherical particles with neck diameter of X [7].

$$\sigma = \frac{4\gamma}{D} \tag{3.3}$$

Using a circle approximation to the neck shape with a radius of p, where p is approximately equal to $X^2/4D$, the curvature at the neck gives a stress as follows:

$$\sigma = \gamma \left(\frac{2}{X} - \frac{4D}{X^2} \right). \tag{3.4}$$

Comparing 3.3 and 3.4 reveals that there is a large stress gradient in the neck region, since the stress changes sign over a relatively small distance. For a small neck the gradient can be quite large. Thus, the stress gradient provides a driving force for mass flow to the neck. As the neck grows, the curvature gradient is relaxed and the process is slow. In the intermediate stage, the curvature around the cylindrical pores provides the driving force. Alternatively, in the final stage, the curvature around the spherical pores drives shrinkage. A reduction in surface energy occurs either by removal of the pores or coalescence of the pores - hence the focus on densification and coarsening during sintering. Similarly, the particles bond and become grains. Grain growth during sintering reduces the grain boundary area and energy. The stress from interfacial energies acting over curved surfaces in a sintering system is termed the sintering stress. In a sense, the sintering stress results from equating the thermodynamic work associated with eliminating surface energy (and area) to mechanical work [7].

The sintering stress is associated directly with the curvature at the interparticle neck. By the final stage, the sintering stress takes on two contributions, one attributed to the pores and the second attributed to the grain:

$$\sigma = \frac{2\gamma_{\mathrm{ss}}}{G} + \frac{4\gamma_{\mathrm{sv}}}{d_p}, \tag{3.5}$$

where G is the grain size, γ_{ss} is the solid-solid grain boundary energy, γ_{sv} is the solid-vapor surface energy, and d_p is the pore size. At small grain sizes the first term is dominant, while at small pore sizes the second term is dominant [7].

Densification increases with the sintering stress, which in turn varies with temperature [7].

3.3 Categories of Sintering

Essentially, sintering processes can be divided into two types: solid state sintering and liquid phase sintering. Solid state sintering occurs when the powder compact is densified wholly in a solid state at the sintering temperature, while liquid phase sintering occurs when a liquid phase is present in the powder compact during sintering. Figure 3.4, in a representative mode, illustrates the two cases in a schematic phase diagram. At temperature T_1, solid state sintering occurs in an A−B powder compact with composition X_1, while at temperatures T_3, liquid phase sintering occurs in the same powder compact [8].

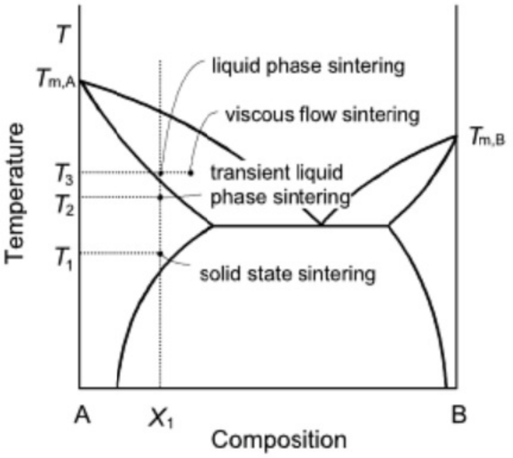

Figure 3.4: Illustration of various types of sintering [8].

Other types of sintering phases exists between solid state sintering and liquid phase sintering, which are for example, transient liquid phase sintering and viscous flow sintering. Viscous flow sintering occurs when the volume fraction of liquid is sufficiently high, so that the full densification of the compact can be achieved by a viscous flow of grain-liquid mixture without having any grain shape change during densification. In the transient liquid phase sintering, a combination of liquid phase sintering and solid state sintering occurs. In this sintering technique a liquid phase forms in the compact at an early stage of sintering, but the liquid disappears as sintering proceeds and densification is completed in the solid state. Resorting again to figure 3.4, it can be observed an example of transient liquid phase sintering when an $A - B$ powder compact with composition X_1 is sintered above the eutectic temperature but below a solidus line A_B, for example at temperature T_2. Since the sintering temperature is above the $A - B$ eutectic temperature, a liquid phase is formed through the reaction between the A and B powders during heating of the compact. During sintering however, the liquid phase disappears and only a solid phase remains because the equilibrium phase under the given sintering condition is a solid phase [8].

In general, liquid phase sintering allows easy control of microstructure and reduction in processing cost, but degrades some important properties, like mechanical properties, when compared with solid state sintering. Liquid phase sintering is applied when specified products utilize properties of the grain boundary phase [8].

3.4 Sintering Variables

It is convenient to identify the major variables that influence the sintering stage. So, the major variables which determine sinterability and the sintered microstructure of a powder compact can be divided into two categories: material variables and process variables (table 3.1) [8].

Table 3.1: Variables affecting sinterability and microstructure [8].

Variables related to raw materials (material variables)	Powder: shape, size, size distribution, agglomeration, mixedness, etc. Chemistry: composition, impurity, non-stoichiometry, homogeneity, etc.
Variables related to sintering condition (process variables)	Temperature, time, pressure, atmosphere, heating and cooling, etc.

The variables connected to raw materials (material variables) include chemical composition of powder compact, powder size, powder shape, powder size distribution, degree of powder agglomeration, etc. These variables influence the powder compressibility and sinterability (densification and grain growth). The other variables involved in sintering are mostly thermodynamic variables, such as temperature, time, atmosphere, pressure, heating and cooling rate [8].

3.5 Driving Force and Basic Phenomena

The driving force of sintering is the reduction of the total interfacial energy [8]. The impetus to reduce the total interfacial energy is considered as the sintering driving force, that includes the force associated to the curvature of the particle surfaces the externally applied pressure and the chemical reactions [9]. The total interfacial energy of a powder compact is expressed as γA, where γ is the specific surface (interface) energy and A the total surface (interface) area of the compact. The reduction of the total energy can be expressed as:

$$\Delta\left(\gamma A\right) = \Delta\gamma A + \gamma\Delta A \tag{3.6}$$

where the change in interfacial energy ($\Delta\gamma$) is due to densification and the change in interfacial area due to grain coarsening. For solid state sintering $\Delta\gamma$ is related to the replacement of solid/vapour interfaces (surface) by solid/solid interfaces. The scheme presented in figure 3.5 shows that the reduction in total interfacial energy occurs via densification and grain growth, the basic phenomena of sintering [8].

3.6 Sintering Mechanism

There are many types of transport mechanism occurring during the sintering process. Figure 3.6 illustrates the paths of material transport of the transport mechanics listed in table 3.2. The material transport due to the difference in interface curvature occurs under the parallel actions of various mechanisms. Some of these material transport mechanisms

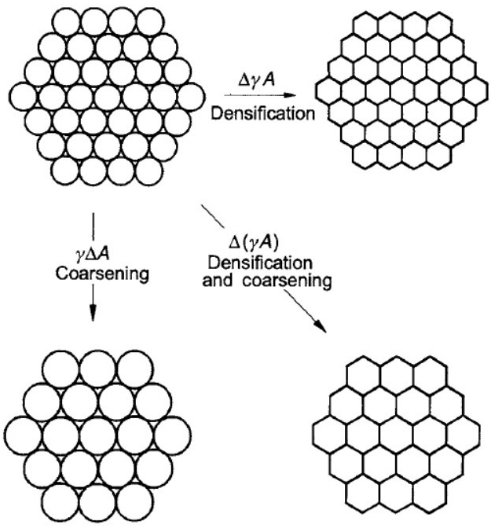

Figure 3.5: Basic phenomena occurring during sintering under the driving force for sintering, $\Delta\,(\gamma A)$ [8].

contribute to densification and shrinkage while others do not [8]. The vacancies and atoms move along the particle surfaces (surface diffusion), along the grain boundaries (grain boundary diffusion), across pore spaces (evaporation-condensation), and through the lattice interior (volume diffusion or lattice diffusion or viscous flow) [9].

Table 3.2: Material transport mechanisms during sintering [8].

Material transport mechanism	Material source	Material sink	Related parameter
Lattice diffusion	Grain boundary	Neck	Lattice diffusivity, D_l
Grain bounday diffusion	Grain boundary	Neck	Grain boundary diffusivity, D_b
Viscous flow	Bulk grain	Neck	Viscosity, η
Surface diffusion	Grain surface	Neck	Surface diffusivity, D_s
Lattice diffusion	Grain surface	Neck	Lattice diffusivity, D_l
Gas phase transport			
Evaporation/Condensation	Grain surface	Neck	Vapour pressure difference, Δp
Gas diffusion	Grain surface	Neck	Gas diffusivity, D_g

From figure 3.6, it can be illustrated that densification occurs only when the atoms move along the grain boundaries and create the continual mass flow into the pores. The center of the particles move closer through diffusion, that leads to the macroscopic shrinkage of the sintering bodies. So, grain boundary diffusion and volume diffusion contribute to densification. On the other hand, surface diffusion, evaporation-condensation are the coarsening mechanisms that occur without producing densification [9].

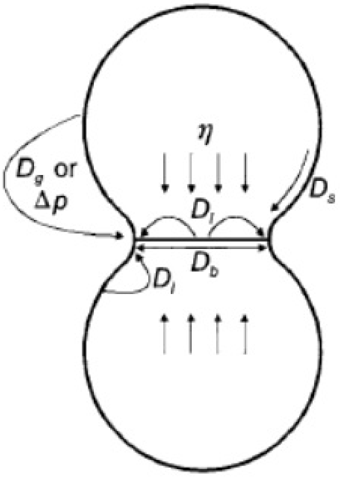

Figure 3.6: Material transport paths during sintering [9].

3.7 Stages of Solid State of Sintering

Solid state sintering is usually divided into three overlapping stages: intial; intermediate and final stage. Figure 3.7 demonstrates the typical densification curve of a compact for these stages over sintering time [8]. There is no clear-cut distinction between the stages, but each stage can be described by its general characteristics, as shown in figure 3.8 [9].

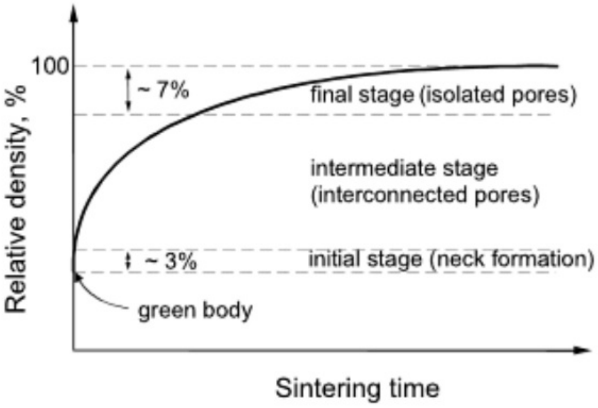

Figure 3.7: Densification curve behaviour of a powder compact through the three sintering stages [8].

The initial stage is characterized by the loose particles rearranging their positions to form new contacts with each other. Afterwards, the sintering necks are formed at the contact area and begin to grow by the diffusion process. The initial stage ends when the neck radius is around 0.3 of the radius of the particle and compact shrinkage is limited to $2-3\%$ at most. The intermediate stage is the most important for densification, since

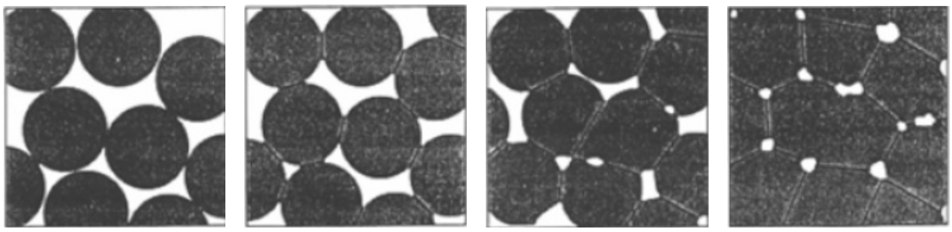

(a) Loose powder at the beginning of sintering

(b) Neck formation and growth in the initial stage

(c) Interconnected pores in the intermediate stage

(d) Isolated pores and grain growth in the final stage

Figure 3.8: Microstructure evolution in PIM sintering involving [9].

it determines the properties of the sintering components. Considerable densification, up to $\sim$ 93% of the relative density, occurs before isolation of the pores. The final stage is characterized by the isolated pores located at the grain corners. It is also known as the coarsening involving growth of the larger grains and the consumption of the smaller grains. For the ideal cylindrical pores occupying the grain boundaries, instability occurs at approximately 8% of the porosity. Considering the porosity distributions of the real materials, the pores begin to close at about 15% of the porosity and are all closed when the porosity is less than 5% [9].

3.8 Models of Initial Stage

The microscopic models are established from the particles level. If spherical particles of the same size are assumed, the sintering of powder compacts can be represented as the sintering between two particles, the two-particle model [8]. The two-particle model is the typical one used to simulate the neck growth and the densification during the initial sintering stage [9]. The typical geometries of the two-particle models are shown in figure 3.9, one without shrinkage (a) and the other with shrinkage (b). In figure 3.9 the distance between the particles does not change but the neck size increases as the sintering time increases [8]. In the model with shrinkage, the neck size increases with an increased sintering time by material transport between the particles and hence shrinkage results [9].

3.9 Intermediate and Final Stage Sintering

When necks form between particles in real powder compacts, pores form interconnected channels along 3-grain edges. As the sintering progresses, the pore channels are disconnected and isolated pores form and, at the same time, the grains grow [8].

Coble presented two geometrically simple models for the shape changes of pores during intermediate and final stage sintering: the channel pore model and the isolated pore model, respectively [9].

In the intermediate stage, the geometry of the grain is regarded as tetrakaidecahedron and the highly interconnected pores are assumed to be cylindrical ones located at the

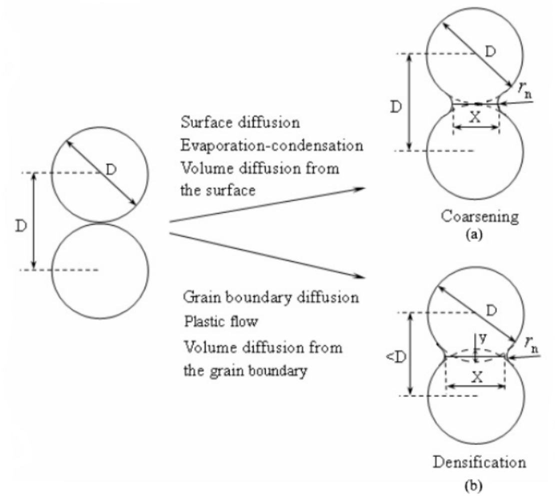

Figure 3.9: Geometrical description of the two-sphere particle model to describe the neck growth and densification in the initial state of sintering (a) without shrinkage; (b) with shrinkage [9].

grain boundaries [9], as shown in figure 3.10 (a).

As a geometrical model of final stage sintering Coble took tetrakaidecahedral grains with spherical pores with a radius of r_1 at their corners, as shown in 3.10 (b).

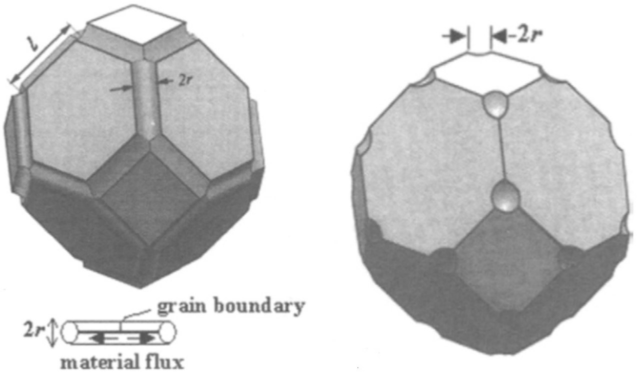

(a) Intermediate Stage Sintering

(b) Final Stage Sintering

Figure 3.10: Coble's geometrical models [8].

Chapter 4

Grain Growth

It is important to present an overview about grain growth, being intimately connected with the sintering cycle. Figure 4.1 demonstrates the formation of two elongated grains from six original particles where the grain behaviour with higher temperatures is shown [10]. It is these phenomenons occurring at higher temperatures that are interesting to approach in the context of this study.

The average grain size of polycrystalline materials increases as the annealing time increase and the phenomenon of grain growth is important in sintering. Phenomenologically, grain growth is divided into two types: normal and abnormal (sometimes also called exaggerated) grain growth. Normal grain growth is characterized by a simple and invariable distribution of relative grain size with annealing time, while abnormal grain growth, which occurs by the formation of some exceptionally large grains in a matrix, shows a bimodal grain size distribution [8].

Grain size influences many mechanical properties of polycrystalline materials [11]. In the case of metallic and ceramic systems are exposed to elevated temperatures, it generally results in grain growth with a simultaneous loss in strength and fractures toughness [12]. Grain growth and deformation are similar in one respect; both involve movement and rearrangement of atoms [11].

In sintering, grain growth reduces the number of diffusion vacancy sinks, which results in a decrease densification rate. Some studies revealed that stainless steel powder compact showed an intimate relation between grain growth and densification processes. The effect was particularly dominant in the intermediate stage of sintering in which the pore structure became rounded, usually when temperatures reach values above 1057 °C and for periods superior to one hour [12].

4.1 Grain Boundary Diffusion in Sintering

In grain boundary diffusion dominated by sintering processes, the sintering stress is proportional to the reciprocal of grain size. It is this relation that connects the macroscale deformation with the microstructure evolution of the material [1].

Grain boundary diffusion is a mass flow mechanism used to describe the solid state sintering of many materials during their densification. Grain boundaries form in the interface between crystals with different atomic orientations. Essentially, grain boundary diffusion consists of lattice defects between grains. Corresponding to large and small

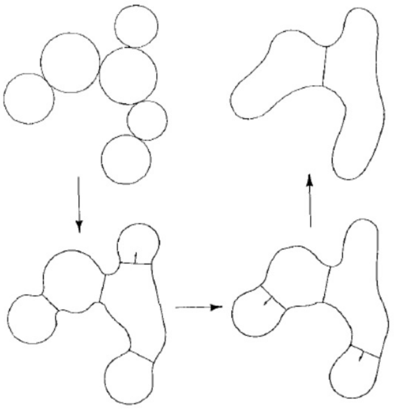

Figure 4.1: Diagram illustrating grain growth in cluster of particles by surface diffusion. Arrows on grain boundaries indicate direction of boundary movement [10].

rotation angles between adjacent grains, the misorientation could be random and repeated, respectively. Therefore, a grain boundary is as narrow as a crystallite, usually in a scale of nanometer. However, it is still an efficient mass flow path [1].

The influence of grain boundary diffusion on sintering is dependent on several factors: the grain shape, the grain size, and the distribution [1].

4.2 Grain Growth Mechanism

Grain growth is the process in which the average grain size of an aggregate of crystals increases. It is driven by the decrease in surface energy and reduction in the total grain boundary area. Grain growth is closely related to the migration of the grain boundary. For continuous materials, depending on the microstructure character and growth pattern, two different types of grain growth have been reported in previous studies: abnormal grain growth (discontinuous) and normal grain growth (continuous). Abnormal grain growth normally commences after a certain period of normal grain growth. Abnormal grain growth occurs at temperatures below $0.7T_\mathrm{m}$ to $0.9T_\mathrm{m}$, where T_m is the melting point. When abnormal grain growth (AGG) occurs, most of the grain boundaries are found to have faceted structures [1]. Abnormal grain growth is a coarsening type of microstructure where some (or a few) large grains grow unusually quickly in a matrix of fine grains with a very slow growth rate [8]. Therefore, the average of the grain size distribution is not changing significantly. When normal grain growth occurs, faceted grain boundaries are replaced with smoothly curved shapes and the grain growth speed increases dramatically despite the initial grain size [1].

If the activation energy for grain growth is high, grain growth may not be very fast and neither is the sintering densification. It has been noted that, as the temperature gets to a transition point, the activation energy may shift to a different level, which causes an immediate increase of grain size. As the grain grows bigger, the growth rate becomes slower. Ultimately, the resistance and the driving force may reach a balance point. According to these observations, it is reasonable to conclude that a transition temperature exists for grain growth of continuous material. This transition temperature defines the boundary between abnormal grain growth and normal grain growth, and also the shift between the two energy levels [1].

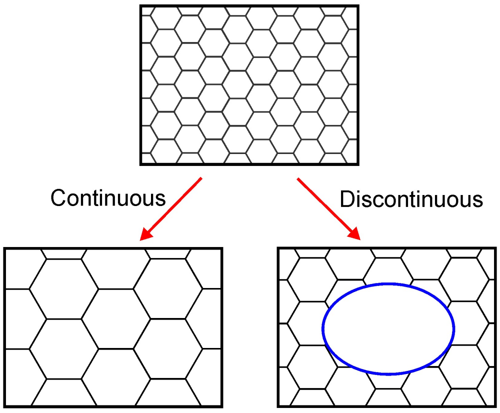

Figure 4.2: Normal grain growth (continuous) and abnormal grain growth (discontinuous) [13].

Considering the fact that even the smallest pore in a powder compact is much larger than the width of a grain boundary or the size of a dislocation, which is around several nanometres, it is reasonable to believe that the grain growth behaviour in a porous body is the same as it is in a full-dense body [1].

The grain growth behaviour occurs approximately in the final of the initial stage of sintering and continues into the intermediate stage. This behaviour is represented in scheme 4.3. Neck growth occurs between two spheres of slightly different size in contact; the grain boundary which develops as a consequence of the misorientation of the spheres at the contact interface (Figure 4.3 (b)) cannot migrate from the neck region because increases in interfacial area and total interfacial energy would be required. The neck disappears with further growth by varying transport mechanisms, which are for example, surface, grain boundary, and volume diffusion, leaving only a thermal groove at the grain boundary (Figure 4.3 (c)). The grain boundary becomes curved. The larger the difference in size between the initial particles, the greater will be the curvature of the grain boundary which develops. Grain-boundary curvature creates a driving force such that the boundary migrates toward its center of curvature. Grain-boundary migration occurs when the boundary is mobile enough to permit ions to move across it. Subsequent grain growth is evidenced by an elongated grain (figure 4.3 (d)) [10].

Thus, grain growth in porous compacts consists of growth of necks between particles until the grain boundary is free to move. Grain-boundary motion is probably fast compared to neck growth, and after the neck reaches a size comparable to that of the smaller grain, the boundary will move rapidly through the smaller grain. During grain growth the grain will either grow or disappear, depending on the size of its immediate neighbour [10].

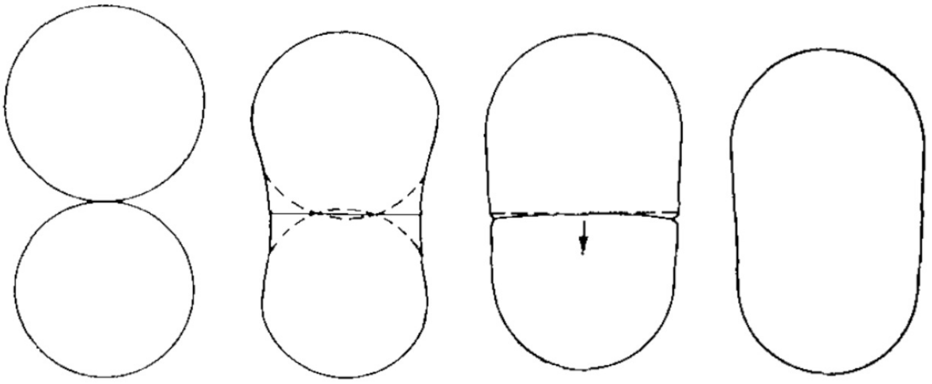

(a) Particles of slightly different size in contact

(b) Neck growth between contacting particles

(c) Grain boundary migration away from contact plane

(d) Grain growth

Figure 4.3: Qualitative mechanism of grain growth in porous compact [10].

Chapter 5

Constitutive Models

5.1 Thermal Expansion

In most cases, the main reason for heat absorption is the atoms vibrational energy increase, and consequently, volume changes. In the absence of phase transformation, most materials show positive heat expansion coefficient (α), i.e., they increase their dimension with an increase in temperature. Consequently, a material subjected to a thermal gradient, will suffer a thermal strain, resulting in thermal dilation. The stain (ε^{T}) is given by:

$$\Delta\varepsilon^{\mathrm{T}} = \alpha_{\mathrm{L}}\Delta T, \tag{5.1}$$

where α_{L} is the linear thermal expansion coefficient and ΔT is the temperature variation [14].

5.2 Heat transport

The sintering atmosphere determines several reactions during sintering. Additionally, the atmosphere is important in transporting heat to the compact [7].

There are three ways to transfer heat: conduction, convection, and radiation. Radiation occurs by the emission of light or other electromagnetic radiation from the furnace walls or heating elements. Convection and conduction require a gas phase. Conduction is heat transport through the gas, based on thermal conductivity of the material, like is explained in 5.2.1. Convection is also through the gas, but depends further on the velocity of the gas at the compact surface and is discussed in 5.2.2 [7].

Once heat is deposited at the compact surface, there is then the necessity to distribute the heat into the compact. This depends on the thermal conductivity, porosity, and gas phase. Usually, pores reduce the thermal conductivity for a material. Usually in most materials, the temperature difference between the surface and the interior is small during sintering [15].

5.2.1 Thermal Conductivity

Thermal conductivity is the property that quantifies the material capability to transport the heat from the high temperature zones to lower temperature zones (heat conduction). The heat conduction is the transmission of energy from particles in an elevated state energy to particles in a lower state energy, in order for each particle to be in a lower energy state [14].

The mathematical model usually applied to quantify the heat conduction is called the Fourier law, which establishes that the heat flux by conduction in a certain direction is proportional to the normal area, to the considered direction and to the temperature in the analysed direction given by:

$$Q = -KA\frac{dT}{dx}, \tag{5.2}$$

where K is the thermal conductivity of the material. The negative signal present on the relation is in consequence of the heat flux direction being opposite to the temperature gradient [14].

The heat conduction through the compact is not a large problem under normal heating rates. Only with large compacts, rapid heating, or high initial porosities will there be opportunities to generate large surface stresses that might cause cracking [7].

5.2.2 Convection

Convection is a commitment between two mechanisms that allow heat exchange. The atomic and the macroscopic movements contribute to the heat exchange. The heat exchange only happens if the material and the surrounding environment are at different temperatures, i.e, distinct energy levels. This exchange ends when the two systems involved reach an equilibrium state. The mathematical model most used to quantify this heat exchange is the Newton cooling law. This law says that the convection heat flux in a determined direction is proportional to the normal area to the considered direction and to the difference in temperatures. The proportionality constant is the convection heat flux (h) included in equation 5.3 [14].

$$q_{\mathrm{c}} = h_{\mathrm{c}}\left(T_{\mathrm{s}} - T_{\infty}\right) \tag{5.3}$$

5.2.3 Radiation

The radiation heat flux exchanged with the surrounding environment can be given by:

$$q_{\mathrm{r}} = k_{\mathrm{r}}\left(T_{\mathrm{s}} - T_{\infty}\right), \tag{5.4}$$

where $k_{\mathrm{r}} = \gamma_{\mathrm{r}}\left(T_{\mathrm{s}}^2 + T_{\infty}^2\right)\left(T_{\mathrm{s}} + T_{\infty}\right)$ and γ_{r} is the constant dependent of Stefan-Boltzman and the emissivity of the material, considering that the green body is inserted in a closed cavity [16].

5.2.4 Temperature distribution

All the materials have the capability to transfer the heat from higher temperature regions for lower temperature regions. During the heat transfer, there is the formation of thermal gradients and then, the necessity of quantifying them in time and space. In an analysis of heat conduction, it is important to try to identify the temperatures field in a specimen, according to the engaging environment. Therefore, it considered an infinitesimal volume element and a thermal balance into this element is applied, resulting in relation 5.5.

$$\dot{E}_{\text{Stored}} = \dot{E}_{\text{In}} - \dot{E}_{\text{Out}} + \dot{E}_{\text{Generated}} \tag{5.5}$$

Considering the Fourier law and the non-existent phase change, a differential equation that allows the temperatures distribution calculations in function of time and space ($T(x, y, z, t)$) is established. This is usually known as heat diffusion equation, which, despite its complexity, is very important in heat conduction transient analysis [14]. Mathematically, this differential equation is expressed as:

$$\rho C_p \frac{\partial T}{\partial t} = \frac{\partial}{\partial x}\left(K_x \frac{\partial T}{\partial x}\right) + \frac{\partial}{\partial y}\left(K_y \frac{\partial T}{\partial y}\right) + \frac{\partial}{\partial z}\left(K_z \frac{\partial T}{\partial z}\right), \tag{5.6}$$

where ρ is the density, C_p is the heat capacity and K_x, K_y and K_z represent the thermal conductivity in, respectively, the x, y and z directions [14].

5.3 Thermo-mechanical behaviour

When a certain material is subjected to a transform process, like what happens in powder metallurgy process, this one stays subjected to a mechanical and thermal residual stresses from the themo-mechanical effects. Therefore, it becomes relevant to study and to analyse the rheological behaviour of the material, i.e., the mechanisms that deform the material when subjected to effects.

It is necessary to point out that this process is an uncoupled process, i.e., in this work there are two distinct processes. The first part, of this work, is focused on the compaction process and the second part is focused on the sintering process. The two processes have distinct behaviours but when together, the powder metallurgy process emerges, which is controlled by a thermo-mechanical behaviour.

Different materials can present different mechanical behaviours, and they are classified according to their behaviour. In this work the isotropic material behaviour is adopted, mainly, to explain the deformation in the compaction process. The isotropic material has uniform characteristics in all directions, i.e., it presents symmetric properties relatively to a plane with arbitrary direction [14].

5.3.1 Strain Components

In this research, the strains created come from the compaction and sintering processes. Thus, velocities or strain rates can be divided into elastic (ε^{e}) and plastic (ε^{p}) that are essentially from the compaction stage and also elastic strain (ε^{e}), creep strain ($\varepsilon^{\mathrm{cr}}$) and thermal strain ($\varepsilon^{\mathrm{t}}$), essentially coming from sintering stage

In a industrial transformation process of a loose powder into a hard metal it occurs the development of the previously referred strains, which will be properly described.

5.3.2 Strain components from powder compaction

Starting by considering the simple case of uniaxial compression of a block material and identifying some elementary features of the material response and how this will be presented in the form of a material constitutive model, the next step is generalise the results to describe the response of porous powder compacts subjected to general multiaxial stress histories [17].

Consider, initially, the situation where a cylindrical specimen of a material is subjected to a uniaxial stress σ and as a result experiences a strain ε. Figure 5.1 shows a typical material response [17].

At low stress occurs the elastic strain, which corresponds to the simultaneous happening of applied force with respective strain, considering this phenomena time dependent. If the relation between the applied force and displacement is linear, the material behaviour is elastic linear. The material elastic behaviour could be interpreted resorting to an analogy with a spring. When a load is applied into a spring, this one deforms. However, the load necessary for increasing the strain also increases. At the end, when the load is removed, the spring returns to their initial state naturally. This kind of behaviour could be defined by Hooke's law. He says that the stress is the product of the elasticity module by the respectively strain [17], like shown in Equation 5.7.

$$\sigma^{\mathrm{e}} = E\varepsilon^{\mathrm{e}} \tag{5.7}$$

As the stress is increased the material eventually yields and plastic strain accumulates. The plastic strain works as a non reversible process. Any plastic strain is permanent and the strain stays in the body after unload. The calculation methodology like Hooke's law loses their influence. In this case, the process is time dependent and change the materials behaviour, in such manner, that their mechanical characteristics come to depend on the history material loads [14]. Figure 5.1 shows the situation where the specimen is loaded beyond the initial yield stress, σ_s, to a stress $\sigma = s$. If the stress is now reduced to zero the specimen unloads elastically. The residual plastic strain accumulated as a result of this loading history is ε^{p}. If the stress is increased to the value $\sigma < s$, the subsequent response is elastic and the total strain experienced by the specimen [17] is given by 5.8.

$$\varepsilon = \varepsilon^{\mathrm{e}} + \varepsilon^{\mathrm{p}} = \frac{\sigma}{E} + \varepsilon^{\mathrm{p}} \tag{5.8}$$

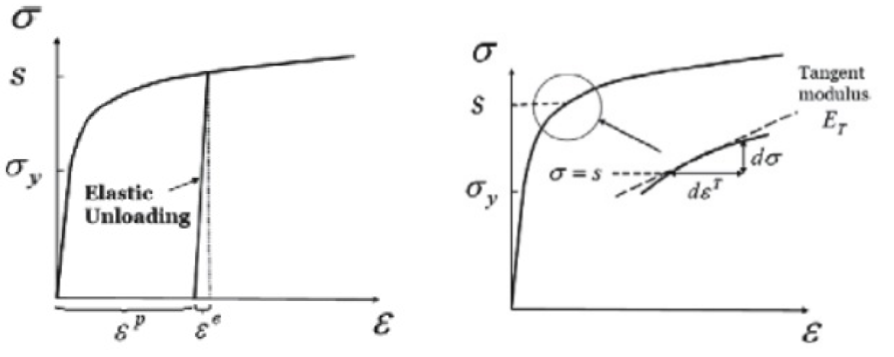

(a) (b)

Figure 5.1: Stress-strain curves for an elastoplsatic material, showing the decomposition of the strain into elastic and plastic components [17].

If the stress is increased to the point $\sigma = s$ further plastic straining can occur. The magnitude of s is important since, it gives the value of stress at which the response is no longer elastic, i.e, it is the instantaneous magnitude of the yield stress that results from prior thermomechanical loading history. It is evident that s (the yield stress) depends on the accumulated plastic strain, i.e, s is a function of ε^{p} [17].

Focus now in the deformation situation under multiaxial states of stress, where the compacts are subjected to axisymmetric loading histories, such as shown in figure 5.2, in which a cylindrical compact is subjected to axial and radial components of stress, σ_{a} and σ_{r} [17].

The hydrostatic component of stress is the mean of the three principal stresses (there are two radial components) and for the axisymmetric stress state of figure 5.2 [17] is given by:

$$p = \frac{1}{3}\left(\sigma_{\mathrm{a}} + 2\sigma_{\mathrm{r}}\right). \tag{5.9}$$

The equivalent stress is related to the principal shear stresses and for the loading of figure 5.2 [17] is given by:

$$q = |\sigma_{\mathrm{a}} - \sigma_{\mathrm{r}}|. \tag{5.10}$$

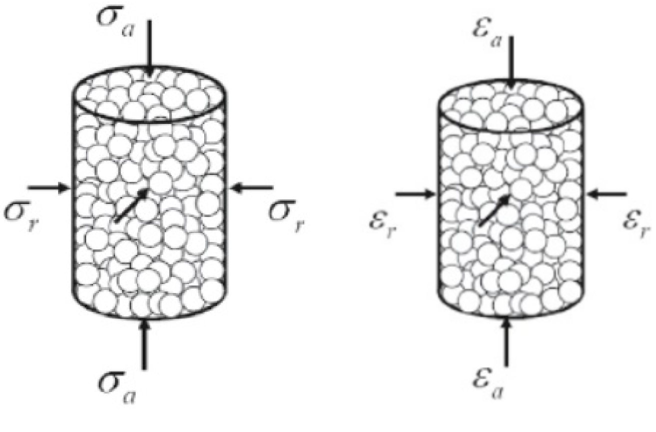

(a) (b)

Figure 5.2: Axial and radial components of (a) stress and (b) strain on an axisymmetric powder compact [17].

Under the axisymmetric loading of figure 5.2 (a) the compact experiences axial and radial strains, ε_{a} and ε_{r}, as show figure 5.2 (b). Considering again elastic response, it proves convenient to define two strain invariants: the volumetric strain, ε_{v}, and the equivalent strain ε_{e}, for the axisymmetric conditions of figure 5.2 (b). For axisymmetric conditions of figure 5.2 (b), the strains are given by equation 5.11 and 5.12 [17].

$$\varepsilon_{\mathrm{v}} = \varepsilon_{\mathrm{a}} + 2\varepsilon_{\mathrm{r}} \tag{5.11}$$

$$\varepsilon_{\mathrm{e}} = \frac{2}{3}|\varepsilon_{\mathrm{a}} - \varepsilon_{\mathrm{r}}| \tag{5.12}$$

For an isotropic elastic material only two material constants are required to define the constitutive response (the relationship between stress and strain). Application of a pressure results in a volume change, relation 5.13, and the effective stress leads to a shape change 5.14 [17].

$$\varepsilon_{\mathrm{v}} = \frac{p}{K} \tag{5.13}$$

$$\varepsilon_{\mathrm{e}} = \frac{\sigma_e}{3G} \tag{5.14}$$

In the previous relations, K is the bulk modulus and G the shear modulus. The elastic response can alternatively be described in terms of the Young's modulus of equation 5.7 and Poisson's ratio, ν. These are related directly to the bulk (relation 5.15) and shear moduli (relation 5.16) [17].

$$G = \frac{E}{2\left(1+\nu\right)} \tag{5.15}$$

$$K = \frac{E}{3\left(1-2\nu\right)} \tag{5.16}$$

When dealing with plastic deformation under multiaxial loading conditions, it is necessary introduce a number of additional concepts. When considering the uniaxial behaviour it was introduced the concept of a yield stress, a stress below which the response is elastic. Under multiaxial loading, it is possible identify a yield surface, a convex surface in stress space: example is given by figure 5.3. For stress histories within the surface the response is elastic and a compact responds to changes in stress according to 5.13 and 5.14. Plastic deformation can only occur if the stress states lies on the yield surface. The yield surface can be expressed as:

$$f = f(q, p, state) = 0, \tag{5.17}$$

where f is a function of two scalar stress measures, q and p and the current state of the material (which was defined in terms of s, or the accumulated plastic strain under uniaxial loading). As with uniaxial loading the response is elastic if $f < 0$ (i.e the stress state lies within yield) and the state $f > 0$ is not achievable [17].

Now, it is necessary to define how the compact deforms plastically at yield. Since plastic strain can accumulate at any point on the yield surface, it proves convenient to express the response in terms of increments of plastic strain, shown in equations 5.18 and 5.19 for the axisymmetric loading of figure 5.2 [17].

$$d\varepsilon_{\mathrm{v}}^{\mathrm{p}} = d\varepsilon_{\mathrm{a}}^{\mathrm{p}} + 2\varepsilon_{\mathrm{r}}^{\mathrm{p}} \tag{5.18}$$

$$d\bar{\varepsilon}^{\mathrm{p}} = \frac{2}{3}|d\varepsilon_{\mathrm{a}}^{\mathrm{p}} - d\varepsilon_{\mathrm{r}}^{\mathrm{p}}| \tag{5.19}$$

The effective strain increment, $d\bar{\varepsilon}^{\mathrm{p}}$, is always positive, thus effective strain will steadily accumulate:

$$\bar{\varepsilon}^{\mathrm{p}} = \int_0^{\bar{\varepsilon}^{\mathrm{p}}} d\bar{\varepsilon}^{\mathrm{p}}. \tag{5.20}$$

An increment of volumetric strain can be related to the change in volume, V of a sample:

$$d\varepsilon_{\mathrm{v}}^{\mathrm{p}} = -\frac{dV}{V}. \tag{5.21}$$

Integrating this relationship from the initial volume V_0, when the strain is zero and the volume V, when the volumetric strain is $\varepsilon_{\mathrm{v}}^{\mathrm{p}}$, gives relations 5.22 and 5.23.

$$V = V_0 e^{-\varepsilon_{\mathrm{v}}^{\mathrm{p}}} \tag{5.22}$$

$$\rho = \rho_0 e^{\varepsilon_{\mathrm{v}}^{\mathrm{p}}} \tag{5.23}$$

In relation 5.23 ρ_0 and ρ are the initial and current densities of the compact, with the second of these relationships determined from the fact that the mass of the compact remains constant [17].

It is convenient to describe the state of the material in terms of plastic strain at a given instant, i.e, $\varepsilon_{\mathrm{v}}^{\mathrm{p}}$ and $\bar{\varepsilon}^{\mathrm{p}}$, or, since the density is directly related to the volumetric strain, by ρ and $\bar{\varepsilon}^{\mathrm{p}}$. Then, the yield condition takes the form shown in 5.24 [17].

$$f = f\left(q, p, \rho, \bar{\varepsilon}_{\mathrm{v}}^{\mathrm{p}}\right) = 0 \tag{5.24}$$

It is generally assumed that the state can be adequately described in terms of the density. The yield condition can then be written as relation 5.25 [17].

$$f = f\left(q, p, \rho\right) = 0 \tag{5.25}$$

Different types of models and forms of yield surface for powder compacts exist. This section, is focused the model used for this research. The Drucker and Prager's two part yield surface was adopted, which was originally developed to model the behaviour of soils. In the form currently employed, it consists of an elliptic compaction region and a transition region, which simply smooths the response between the compaction and shear-Clayfailure regimes, where normality of the strain increment vector is again assumed [17].

In figure 5.3, the shear failure line has been drawn such that a compact has a finite shear stress, i.e., there is cohesion [17]. A number of extensions of this model have been proposed, however for this research, this plasticity model was adopted and will be fully explained in section 6.4.

5.3.3 Strain Components From Sintering

Sintering is mainly affected by viscoelastic behaviour. This is found in those materials which respond to an applied stress by both recoverable and permanent deformations, which are time dependent. Non-crystalline organic polymers exhibit this behaviour. Time-dependent permanent deformation is termed as viscous flow. When subjected to external stresses many crystalline materials undergo not only elastic deformation

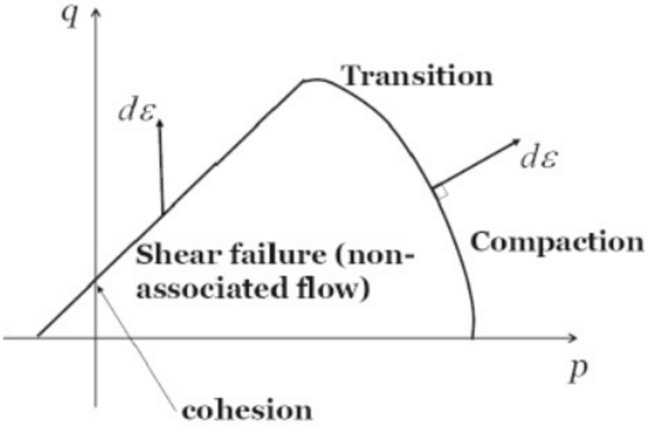

Figure 5.3: The Drucker-Prager two-surface model [17].

but also viscous flow. Viscoelastic mechanical behaviour, is the intermediate behaviour between totally elastic and totally viscous. It may notes that it is analogous to the creep phenomenon in crystalline materials [18].

Viscoelastic creep happens when the stress level is maintained constant. Many crystalline materials are found to be susceptible to time-dependent deformation. Such deformation is termed as viscoelastic creep. This type of deformation may be significant at room temperature and under modest stresses that lie below the yield strength of the material [18].

Thus, the behaviour presented in the sintering stage is called thermo-viscoelastic behaviour. The principals influences come from the elastic strain (ε^{e}) (this elastic strain has the same behaviour as in section 5.3.2), the creep strain ($\varepsilon^{\mathrm{cr}}$), and the thermal strain (ε^{t}). These two last components will be boarded in the next paragraphs.

Creep

Creep is essentially a slow rise of plastic deformation under the action of stress below the yield strength of the material. A typical curve of deformation versus loading time is shown in figure 5.4. The first stage is called the unstable or transient creep (also called initial or primary creep). The second stage is the stage of steady-state, or secondary creep and is characterized by a constant deformation rate. At third stage (tertiary, or accelerated creep), the deformation rate increases up to failure. The third stage is, as a rule, short and should be avoided, since quick failure of parts is inevitable at this stage [18].

A physical explanation of the three stages of creep is as follows:

- *Primary Creep*: This stage is mainly due to dislocation movement. The creep rate decreases with time and the effect of work hardening is more than that of the recovery process [18].
- *Secondary Creep*: The rates of work hardening and recovery during this stage are equal, so the material creeps at a steady state rate(minimum creep rate). Depending upon the state level and temperature, steady state creep may be essentially viscous or plastic character [18].

- *Tertiary Creep*: Creep rate increases with time until fracture occurs in this stage. Tertiary creep can occur due to necking of the specimen or grain boundary sliding at high temperature and this continues until specimen fractures [18].

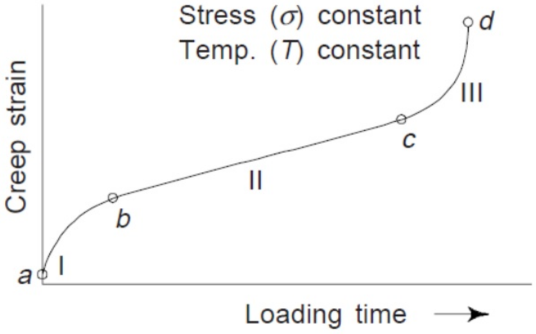

Figure 5.4: Creep curve at constant temperature and stress: I - transient creep stage; II - steady stage creep; III - fracture stage [18].

The development of each stage of creep depends on the temperature and stress. The phenomenon of creep is observable in metals, ionic and covalent crystals, amorphous materials such as glasses and polymers. In polymers, the phenomenon of creep is important at room temperature, in alloys at 100 °C, and in steel above 300 °C. Metals generally exhibit creep at high temperatures. A material subjected to a constant tensile load at an elevated temperature will creep and undergo a time dependent deformation. It is noted that high temperatures lead to rapid creep which is often accompanied by microstructural changes [18].

Mechanisms of Creep

There are many mechanisms of creep, which have been proposed. Creep is a thermally activated process. Some significant mechanisms that play vital roles during the creep process are: dislocation climb; vacancy diffusion and grain boundary sliding [18].

An appreciable atomic movement at high temperature causes the dislocations to climb up and down. In response to the applied stress, the diffusion rate of vacancy may produce a motion by a simple climb of edge dislocation. Obviously, edge dislocations are piled up by the obstacles in the glide plane and the rate of creep is governed by the rate of escape of dislocations past obstacles [18].

Another mechanism of creep is called diffusional creep or diffusion of vacancies. The diffusion of vacancies controls the creep rate, but the mechanism does not involve the climb of edge dislocations. In response to the applied stress, the vacancies move from surfaces of the specimen transverse to the stress axis to the surfaces that are parallel to the stress axis. Over a period of time, this movement would elongate the specimen in the direction of the stress axis and contract it in the transverse direction resulting in creep [18].

The third mechanism of creep is the sliding of grain boundaries, i.e, sliding of neighbouring grains with respect to the boundary that separate them. When compared to individual grains, grain boundaries lose their strength at a lower temperature. This

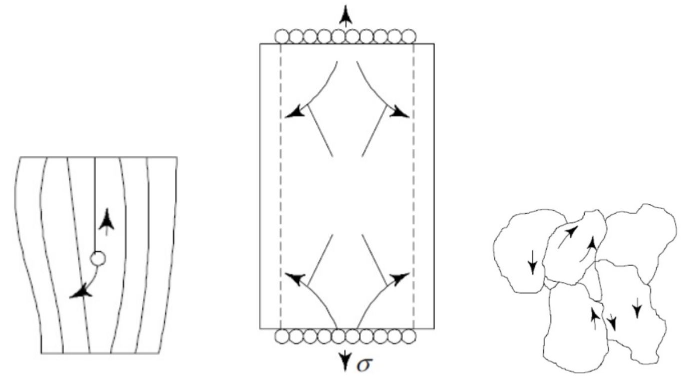

(a) (b) (c)

Figure 5.5: Mechanism of creep [18].

effect arises from the non-crystalline structure of the grain boundaries and grain boundaries play a major role in the creep of polycrystals at high temperatures as they slide past each other or create vacancies. At higher temperatures, ductile metals begin to lose their ability to strain-harden and become viscous to facilitate the sliding of grain boundaries. It is possible to detect that at temperatures above $0.5T_m$ the viscosity of the grain boundaries is small enough for them to behave like a very viscous liquid separating the neighbouring grains and allowing them to slide against each other. At low temperatures, grain boundaries do not flow viscously, but provide effective obstacles to dislocation motion. Obviously, the grain boundaries facilitate the deformation process by sliding at high temperatures, whereas at low temperatures, they increase the yield strength by stopping the dislocations [18].

5.4 Thermal effects

For porous materials that suffer a relatively small amount of densification during solid state sintering, the thermal deformation should not be ignored. Accurate simulations of the entire sintering process require the consideration of not only the creep strain but also the thermal strain.

5.4.1 The sintering cycle

Each material has its own optical sintering cycle. Thus, it is instructive to consider known cycles to establish a starting point for any material. Beyond the parameters of particle size, temperature, and time, there are further influences from the heating rate, process atmosphere, impurity level, and intermediate holds not regularly noted [7].

The sintering cycle is the set-up of thermal conditions specifically for densifying powder metal compacts. Generally, the optimal cycle is material and application dependent. A complex sets of factors needs to be considered for the determination of an appropriate sintering cycle. Some essential factors are some like heating rate, maximum temperature hold time, and atmosphere [7].

The sintering cycle selected for this research is shown in figure 5.6. It begins with heating at a rate of 10 °C to a maximum temperature of 1350 °C. After a one hour hold, the part is cooled at 10 °C. However, the actual sintering cycle might differ a little bit from the designed one due to the capability of the furnace. Especially, the cooling rate might not be as expected. If the densification is near complete after the hold, slight variation in the cooling should not have a significant influence on the final shrinkage [1]. A comparison of the prescribed sintering cycle and an actual one can be seen in figure 5.6.

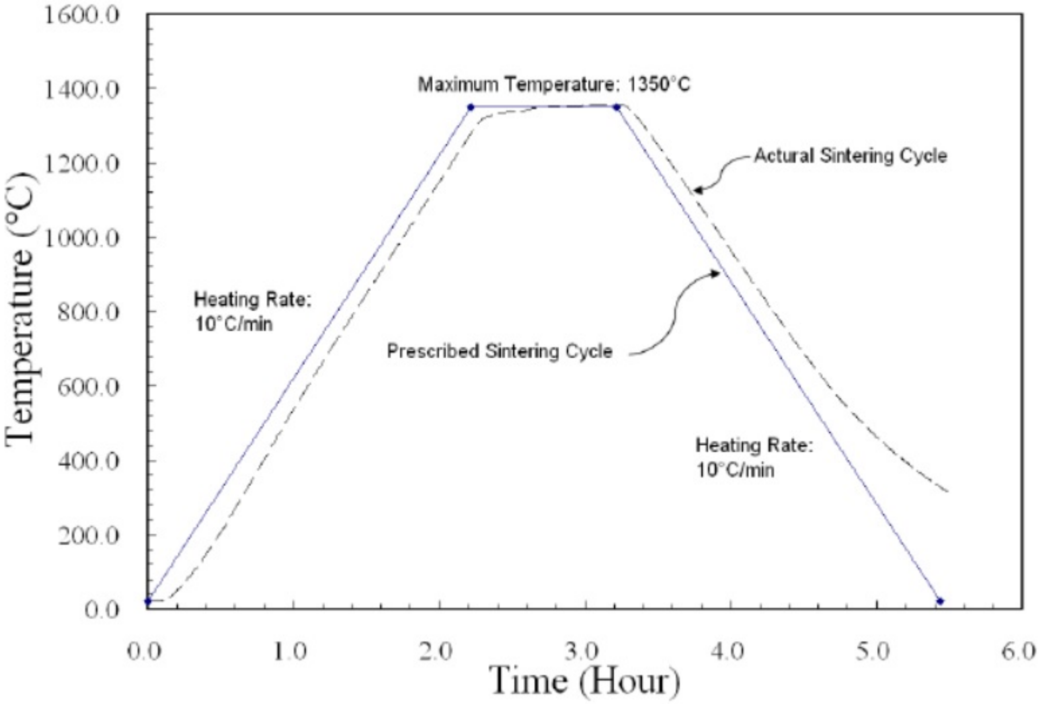

Figure 5.6: Sintering cycle [1].

Part II

Numerical Methodology and Implementation

Chapter 6

Numerical Methods

6.1 Introduction

Nowadays, with a constant evolution of competitive economy, the industrial processes have to be adapted to the evolution of modern demands. Therefore, through the years, PM industry has adapted to the new tools that engineering offers. With the evolution of computers and finite element analysis, the PM industry had the necessity of abandoning the trial and error process and starting to resort to FEM. Over time, many researchers have had the ability of adapting an industrial physical process to a finite element model and started to study the numerous phenomenons which occur during the process based in numerical models. In this research, the compaction and sintering processes are reproduced resorting to ideal models and using the finite element program as an auxiliary tool.

In this chapter, an allusion to the FEM and to the finite element program (Abaqus) is done. However, the major objective is to describe the models of the compaction and sintering processes.

In the compaction process, an elasto-plastic model is used that is initial referred in section 5.3.2 and is presented in section 6.4. In the sintering process, the model adopted for simulating the solid phase of sintering in a finite element program is a viscoelasticity model. The viscoelasticity model and the parameters that influence the model in sintering are exhaustively described in section 6.5.

6.2 Finite Element Method (FEM)

The finite element method (FEM) is a powerful numeric analysis tool and enables problem resolution from various study areas, usually in an approximate form. However, this method should be an alternatively when there are analytical approaches of solving the problem. Additionally, when this method is used, error estimation should be taken into consideration [14].

Essentially, FEM consists in a subdivision of continuous systems into discrete elements, in which it is possible to establish constitutive laws. This subdivision process is designated discretization and each one of the discretized elements is designated finite element. The several elements that constitute the solid are linked by nodes and in the calculation process there is a necessity to extrapolate the individual model to the global model, which is called assembling. In FEM, many types of elements can be applied depending on the type of problem. In the bidimensional problems, the elements usually applied are quadrilateral and triangular. In the tridimensional problems they are usually hexahedrons, tetrahedrons and pentahedrons [14].

Approaching the method from the user viewpoint, it is possible to define three different steps. These steps are commonly called: pre-process, analysis and post-process [14].

The pre-process step is connected to the model creation and the discretization of the conditions submitted. Commercial software includes many graphic tools that facilitate the task of creating the model. The finite element global analysis quality is strongly dependent to the user's capability to extrapolate the problem for the computation reality, because it is necessary to do some simplifications and to define modelling strategies. Sometimes, there are complex models to generate and it is common to resort to a specialized software to create the models. This is designated CAD program (Computer Aided Design). So, the necessity of pre-processing appears, for having the ability of interpreting and translating models from other softwares [14].

The analysis step is the most important part, because it is where all the numeric calculation is done. However, from the user's point of view, this step is used like a "black box". During this stage, many files are generated with all the results that are wanted by the user [14].

The last stage is about interpreting the files referred in the previous paragraph and show them in a user friendly form. Typically, the results are presented under color maps, which present a friendly way to interpret the results [14].

6.3 Abaqus

The finite element code adopted for this research is the Abaqus program because it has numerous applications and good calculation power, specifically in thermo-mechanical models. The Abaqus/CAE program uses a graphic interface, where the pre-processing is made, and it allows to implement all the simulation architecture, starting with the geometry, passing through temporary integration, as well as problem discretization. In this stage, the code allows the definition of several necessary aspects and at the end it generates an ASCII text file with INP extension, which the calculation engine processes [14].

The analysis step is done by Abaqus/Standard or by Abaqus/Explicit, depending on the temporal integration choice that was made in the pre-processing step. However, in the context of this work, it is used the Abaqus/Standard, due to implicit integration that shows more stability in the calculation process. Independently of time integration chosen, the calculation engine generates several output files during the simulation, like result files, error messages or warnings and the several time increments' description considered by the calculation engine [14].

Finally, the post-processing is realized through the Abaqus/Viewer that operates the results file and allows the user to visualize the obtained results [14].

6.4 The Modified Drucker-Prager/Cap Model

In the first stage of the present work, for understanding the compaction phase, it was modelled and simulated using the FEM with Abaqus. Process simulations resorting to FEM program may be useful for controlling the shape of final PM components and can provide the distribution of green density and stresses of the compacted parts [19] [20].

In order to have a reliable numerical simulation it is necessary to perform two tasks. The first task is to chose an appropriate constitutive model for modelling the compaction process in a FEM program. Secondly, well defined calibration experiments are carried out for an easy identification of the constitutive model parameters of the powder material [20]. This second task was not reproduced in the present work. The constitutive model parameters used for implementing the model in the FEM program were taken from the literature.

In the past decades, many constitutive models including micro-mechanical and macro-mechanical models have been studied. The compaction of metals and ceramic powders can be simulated using phenomenological elasto-plastic continuum models from soils mechanics. These models are typically implemented in finite element codes and have been used to investigate the macroscopic property distributions in powders during compaction. Specifically, in this work, it was chosen the phenomenological modified Drucker-Prager/Cap (DPC) constitutive model which was originally intended to model geological materials, it has been modified and adapted for metal powder compaction. The modified Drucker-Prager/Cap model defines the behaviour of powder rearrangement and consolidation during compaction processes very well [20].

6.4.1 Description of the constitutive model

In the analysis to be made in part III, the modified Drucker-Prager/Cap elasto-plasticity model is adopted to model the uniaxial compaction of metal powders. This model is implemented in the library of the commercially available finite element program Abaqus. This type of model allows the effect of the stress states to be addressed during the unloading (removal of the upper punch) and after the ejection (removal of the compacted component from the die) as well as during the compression model itself [21]. In elasto-plastic materials with work hardening, it is necessary to consider a constitutive model that consists primarily in three parameters: the yielding criterion, the flow potential and the hardening criteria that govern the evolution of the cap as a function of volumetric strain [22]. The modified Drucker-Prager/Cap elasto-plasticity model allows the computation of the density distribution and the prediction of the redistribution of the density after the load removal and during the ejection modes [21]. A typical yield surface that characterizes this model is represented in figure 6.1. This surface is plotted in a stress space characterized by:

$$p = \frac{1}{3}\left(\sigma_1 + \sigma_2 + \sigma_3\right), \tag{6.1}$$

$$J_2' = q = \frac{1}{6}\left[(\sigma_1 - \sigma_2)^2 + (\sigma_2 - \sigma_3)^2 + (\sigma_3 - \sigma_1)^2\right]. \tag{6.2}$$

The equations shown in 6.1 and 6.2 represent the coordinates where the equivalent pressure or hydrostatic pressure is p and the von Mises equivalent or effective stress (also

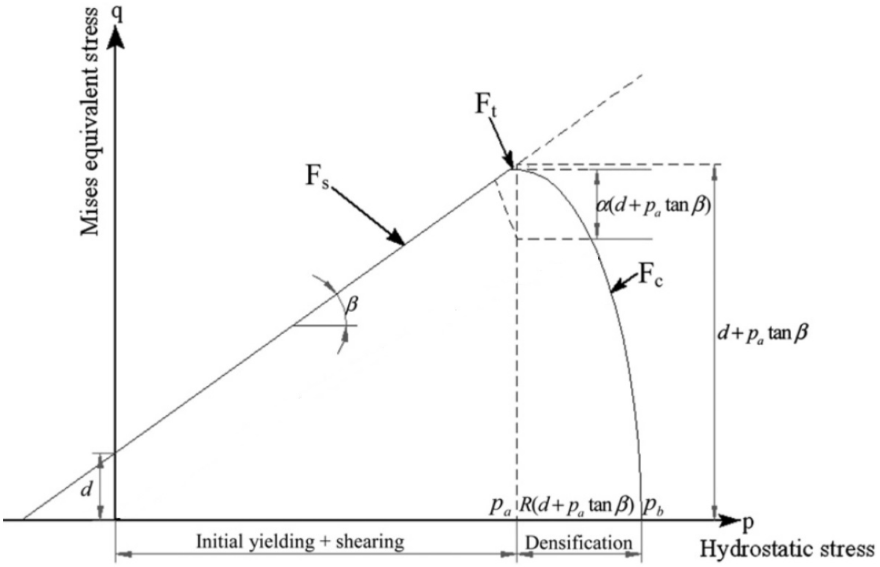

Figure 6.1: Drucker-Prager/Cap model; yield surfaces in the $p-q$ plane [22].

called the second invariant of the deviatoric stress) is $\sqrt{J_2'}$. Also, in equation 6.1 and 6.2 σ_1, σ_2 and σ_3 are the principal stresses (compression assumed positive) [21].

In the modified Drucker-Prager/Cap model, the yield surface includes two main segments: a shear failure surface, providing predominately shear failure (F_s) and a cap which intersects the hydrostatic stress axis (F_c) (figure 6.1). There is also a transition region between these segments (F_t), which is introduced to provide a smooth surface. The cap line serves two main purposes. It bounds the yield surface in pure hydrostatic compression, thus providing an inelastic hardening mechanism to represent the plastic nature of the compaction. It also controls the volume dilatancy when the material yields in shear, by providing a softening as a function of the inelastic volume increases created as the material yields on the shear failure and the transition yield surfaces [21].

Now, the essential components of the current model are demonstrated. A linear strain rate decomposition is assumed in the form:

$$d\varepsilon = d\varepsilon^{\mathrm{el}} + d\varepsilon^{\mathrm{pl}} \tag{6.3}$$

where $d\varepsilon$ is the total strain rate, $d\varepsilon^{\mathrm{el}}$ is the elastic strain rate, and $d\varepsilon^{\mathrm{pl}}$ is the inelastic (plastic) strain rate. The elastic behaviour may be modelled as linear elastic, or by using various types of non-linear elastic models [21]. In the current numerical analysis the elastic response is assumed to be linear.

The yield function for admissible stresses, in the modified Drucker-Prager/cap model, is established by three surfaces in the p-q plane. The shear surface F_s rules the initial compaction and densification during powder compaction [22]. This criterion describes the shear stress required for simple slip, depending on the cohesion and hydrostatic pressure. This shear surface is defined by:

$$F_\mathrm{s}(q,p) = q - d - p.\tan(\beta) = 0, \tag{6.4}$$

where d is the material's cohesion and β is the material's internal friction angle. The parameters β and d are often given some physical significance [21] but in this research are simply regarded as unique material properties.

The cap surface, F_c is responsible for controlling the densification/hardening of the material at large compaction pressures. The cap surface hardens or softens as a function of the volumetric strain: volumetric plastic compaction (when yielding on the cap) causes hardening (in a triaxial stress), while volumetric plastic dilation (when yielding on the shear failure surface) causes shear induced softening. The cap surface is represented in figure 6.1 and is modelled as an ellipse with a constant eccentricity in $p-q$ space [21] [22]. The cap surface, F_c is given by:

$$F_\mathrm{c}(q,p) = \left((p-p_a)^2 + \left[\frac{R\times q}{1+\alpha+\alpha/\cos\beta}\right]^2\right)^{1/2} - R\left(d+p_a.\tan\beta\right) = 0, \tag{6.5}$$

where the constant R is the material parameter that controls the shape of the cap (equal to the ratio of the major and minor axes of the elliptical cap), p_a is an evolution parameter that represents the volumetric plastic strain driven hardening/softening effects and α is a constant that ensures a smooth transition between the shear and cap surfaces. It is assumed that the cap surface is a continuous family of ellipses and each one corresponds to a value of inelastic strain rate, i.e, the relative density of the compact. A hardening/softening law must be defined which relates the hydrostatic compaction yield stress, p_b, and the corresponding volumetric plastic strain $\varepsilon_\mathrm{vol}^\mathrm{pl}$ (figure 6.2) [21]. The evolution parameter p_a is defined in the form:

$$p_a = \frac{p_b - Rd}{(1+Rtan\beta)}, \tag{6.6}$$

where the parameter α is a small number (typically 0.001 to 0.05) used to provide a smooth transition surface between the shear failure surface and the cap [21].

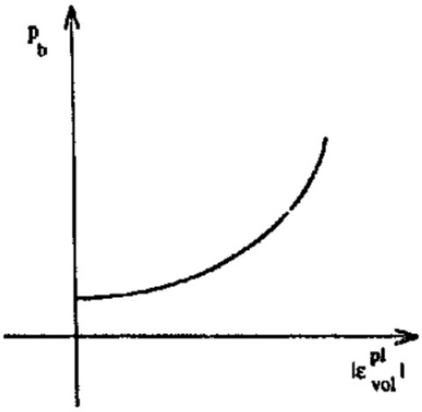

Figure 6.2: Typical cap hardening [21].

With the objective to obtain a smooth yield surface, a transition region is defined between the shear failure line and the cap surface using α.

$$F_\mathrm{t}(q,p) = \{(p-p_a)^2 + [q-(1-\alpha/\cos\beta)\,(d+p_a.\tan\beta)]^2\}^{1/2} - \alpha\,(d+p_a.\tan\beta) = 0 \tag{6.7}$$

This smooth transition between the cap and failure yield surfaces is necessary for preventing the corners between these two yield surfaces and also avoid numerical instabilities while transitioning the shear and the cap yield surfaces [22].

Plastic flow is defined by a flow potential that is associated in the deviatoric plane, associated on the cap in the meridional plane and non-associated on the failure surface and the transition surface in the meridional plane [21]. The flow potential, which is similar to the yield locus, must be described in a powder compaction model, being necessary to study the evolution of inelastic deformation that results from densification and plastic deformation of particles. The direction of the plastic strain is controlled by the shape of plastic flow potential [22]. The flow potential surface in the meridional plane is shown in figure 6.3.

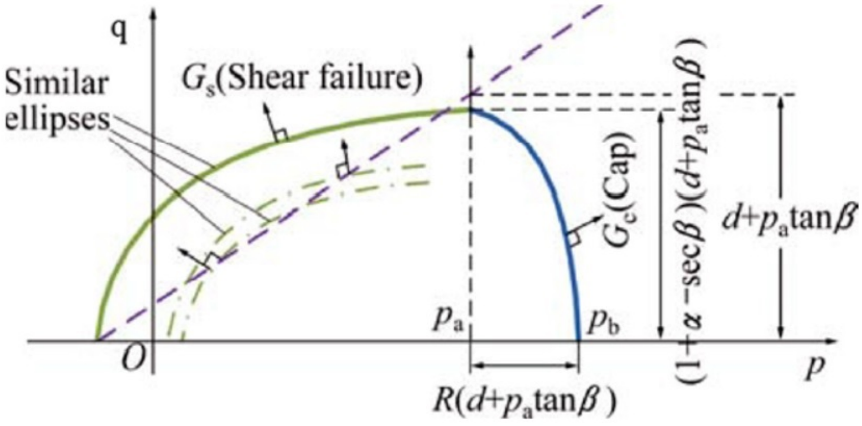

Figure 6.3: Flow potential in $p-q$ plane [20].

The flow potential is made up of an elliptical portion in the cap region (equation 6.8) that is identical to the cap yield surface (equation 6.5). Another elliptical portion in the failure and transition regions that provides the non-associated flow component in the model is given by:

$$G_\mathrm{c} = F_\mathrm{c}(q,p) = \left((p-p_a)^2 + \left[\frac{R \times q}{1+\alpha+\alpha/\cos\beta} \right]^2 \right)^{1/2} - R\left(d + p_a \tan\beta\right) = 0, \qquad (6.8)$$

$$G_\mathrm{s} = \{[(p-p_a)\tan\beta]^2 + q^2\}^{1/2}. \qquad (6.9)$$

The two elliptical portions G_c and G_s form a continuous and smooth potential surface [21].

6.5 Linear Viscoelasticity Theory

As can be deduced from its name, viscoelastic materials possess both viscous and elastic properties in varying degrees. Linear viscoelasticity is the simplest response of a viscoelastic material [15].

The linear theory of viscoelasticity was primarily applied on polymeric materials to study their behaviour [1]. In general, research on viscoelastic behaviour of polymeric materials and their composites are well advanced when compared to powder metallurgy components, even though their application is extensive [23]. Materials within the scope of viscoelasticity theory possess a capacity to store and dissipate mechanical energy. For these materials, a state of stress induces an instantaneous deformation followed by a flow process which may or may not be limited in magnitude as time grows. The external loads could influenced not only by mechanical forces or stresses, but also by thermal induced loadings, such as the hydrostatic sintering stress [1].

Since a viscoelastic material exhibits both an instantaneous elasticity effect and creep characteristics, the material response is not determined only by the current state of stress, but also by all past states of stress. The incremental theory of plasticity also accounts for the history dependent material behaviour. However, the underlying difference between the theories of plasticity and viscoelasticity is that the first is independent of the time scale involved in loading and unloading while the second has a specific time or rate dependence [1].

At high temperatures associated with sintering, the porous material presents elastic and viscous types of behaviour. During pressure or pressureless whether there is a constant or zero mechanical loading, a time-dependent strain will emerge during the long process. This thermal induced strain is called the sintering strain, viscous strain, or creep strain. This creep strain is similar to the traditionally defined creep strain which results from constant mechanical loading and is both permanent time dependent. Therefore, the viscoelasticity theory can be used to simulate the sintering process [1].

6.5.1 Viscoelasticity Models

As was said before, viscoelasticity indicates a material with the features of both a viscous fluid and an elastic solid. The term elastic and viscous nature is the represented action of spring and the response of a putty system. In the first case, the return of spring to its original position when stretched and then released is an example of elastic action. In the second case, the retaining capability of the extended state when it is pulled is an example of viscous nature. Materials with a combination of these properties are called viscoelastic [23].

Many viscoelasticity models have been developed to describe a wide range of deformation behaviours. These models are composed by elastic and viscous components in various configurations. Usually, the elastic component can be represented by an elastic spring and the viscous component by a dashpot, a pot that contains a viscous liquid that can flow under the action of a piston. A representative illustration of the deformation behaviour of the components is shown in figure 6.4. The equations which describe the responses of figure 6.4 are given by:

$$\sigma = E\varepsilon \quad \text{and} \tag{6.10}$$

$$\sigma = \eta \left(\frac{d\varepsilon}{dt} \right), \tag{6.11}$$

where σ is the tensile stress, E is Young's modulus and η is the viscosity [1].

Different forms of the yield components lead to different models. A very well known is the Maxwell model. This model consists of a spring and a dashpot placed in series. The overall strain rate is the sum of the contributions from both components, and the

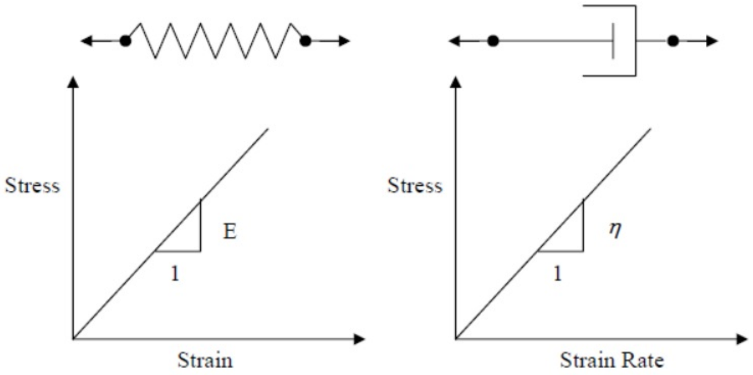

Figure 6.4: Spring and dashpot components and their mechanical response [1].

constitutive equation is given by:

$$\dot{\varepsilon} = \frac{\dot{\sigma}}{E} + \frac{\sigma}{\eta}, \tag{6.12}$$

where the first part of the right hand side corresponds to the equivalent elastic strain rate, while the second part is the creep strain rate. It is relevant to note that the equivalent elastic strain rate is a function of the stress state, which can change with time during sintering [1].

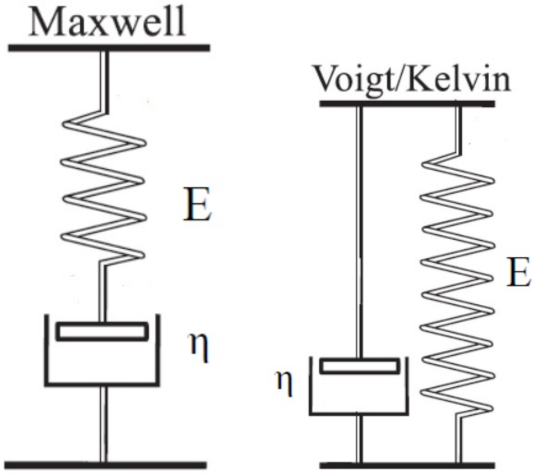

(a) The Maxwell model of a spring and dashpot in series

(b) The Kelvin model of a spring and a dashpot in parallel

Figure 6.5: The Maxwell and Kelvin models [24].

An alternative to the Maxwell model (figure 6.5 (a)) is the Voigt or the Kelvin model (figure 6.5 (b)) that is characterized by a spring and a dashpot in parallel. In this model, the strains on the two components are always the same and the overall stress is the sum of the stresses on the spring and dashpot [1]. The corresponding constitutive equation is given by:

$$\sigma = E\varepsilon + \eta\dot{\varepsilon}. \tag{6.13}$$

6.5.2 Constitutive Equations

For this research, a set of constitutive equations based on the Maxwell model were adopted, which is more suitable for describing the deformation behaviour of metals at high temperature.

For the phenomenological model of sintering, the constitutive equation is selected as a nonlinear viscous incompressible model containing uniformly distributed voids. The strain rate is subdivided in a component of equivalent elastic strain rate $\dot{\varepsilon}^{\mathrm{e}}$, thermal strain rate $\dot{\varepsilon}^{\mathrm{t}}$, and creep strain rate $\dot{\varepsilon}^{\mathrm{cr}}$ and is given by:

$$\dot{\varepsilon} = \dot{\varepsilon}^{\mathrm{e}} + \dot{\varepsilon}^{\mathrm{t}} + \dot{\varepsilon}^{\mathrm{cr}}. \tag{6.14}$$

In the right hand part of equation 6.14, the elastic strain portion is assumed to be linear and isotropic. Thus, it can be represented by:

$$\dot{\varepsilon}^{\mathrm{e}} = \frac{\dot{\sigma}}{C}. \tag{6.15}$$

Equation 6.15 can be expressed by the rate form of Hooke's law, as is shown in equation 6.16 [1].

$$\dot{\sigma} = C\dot{\varepsilon}^{\mathrm{e}} = C\left(\dot{\varepsilon} - \dot{\varepsilon}^{\mathrm{t}} - \dot{\varepsilon}^{\mathrm{cr}}\right) \tag{6.16}$$

The stress can be calculated from the integral of equation 6.16 [1].

$$\sigma = \int \dot{\sigma} dt = \int C\dot{\varepsilon}^{\mathrm{e}} dt = \int C\left(\dot{\varepsilon} - \dot{\varepsilon}^{\mathrm{t}} - \dot{\varepsilon}^{\mathrm{cr}}\right) dt \tag{6.17}$$

Thermal strain is proportional to the change in temperature of the material and is the same in all directions for an isotropic material. It can be calculated as:

$$\varepsilon^{\mathrm{t}} = \alpha \cdot \Delta T, \tag{6.18}$$

where, the parameter α represents the thermal expansion coefficient, which is usually a function of temperature, ΔT is the difference between the current and reference temperatures [1].

The creep strain rate, applied in this work, consists in two parts: the ratio between the deviatoric stress σ' and shear viscosity modulus, η_{s} , and the ratio between the equivalent volumetric stress and bulk viscosity modulus η_{b}. In order to analyse the dimensional change of the sintering body, the creep strain rate is given by:

$$\dot{\varepsilon}^{\mathrm{cr}} = \frac{\sigma'}{2\eta_{\mathrm{s}}} + \frac{tr\left(\sigma\right) - 3\sigma_{\mathrm{s}}}{9\eta_{\mathrm{b}}} I, \tag{6.19}$$

where σ_{s} is the sintering stress (sintering driving force), $tr(\sigma)$ is the trace of the stress tensor and I an identity matrix. In the right side of equation 6.19, the first term represents the shape distortion of the sintering body, and the second one determines the

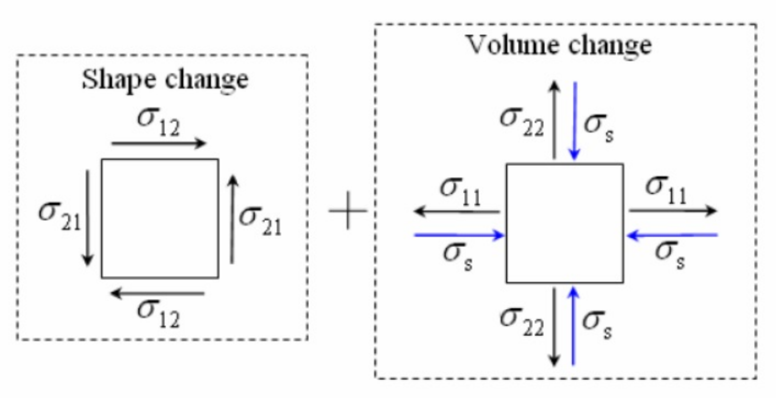

Figure 6.6: A diagram to show the local stress state of the sintering body that undergoes shape and volume changes [9].

volume change or density evolution. In the sintering model, the local stress equilibrium is presented under zero external loading [1]. The local stress can be shown in figure 6.6.

The η_s, η_b and σ_s are the material parameters. Generally, they are influenced by factors such as relative density, temperature, grain size and pore size, as well as the physical parameters of the material such as the diffusion coefficient and activation energy [9].

6.5.3 Viscosity Modulus

Viscosity is the material resistance to viscous flow. Usually, the viscosity modulus is temperature-dependent. During sintering, temperature has a wide variation, therefore, the material response is expected to vary. For this study, it is reasonable to consider the viscous flow of a thermal activated process, therefore it is employed the Arrhenius equation given by:

$$\eta = \eta_0 e^{\frac{Q_v}{RT}}, \tag{6.20}$$

where Q_v is the activation energy for viscous flow, η_0 is a pre-exponential material constant, R is the universal gas constant and T is the absolute temperature. When the material starts to behave more like a liquid, at high sintering temperatures, the Arrhenius relation is expected to be more accurate [1].

For a porous material, because of the existence of pore area, the parameters in the continuous viscoelasticity theory should be modified before they can be employed. Most of these parameters are functions of porosity. The shear viscosity modulus η_s and bulk viscosity modulus η_b are defined as:

$$\eta_s = (1-\theta)^2 \eta \quad \text{and} \tag{6.21}$$

$$\eta_b = \frac{4}{3}\frac{(1-\theta)^3}{\theta}\eta, \tag{6.22}$$

where θ is the porosity defined as the ratio of void and bulk volumes, and η is the apparent viscosity defined in equation 6.20 [1].

6.5.4 Sintering Stress

Sintering stress has an important impact on the sintering kinetics. Sintering stress, σ_{s}, also named sintering driving force, is the equivalent hydrostatic pressure caused by local capillary stresses in porous structures. The resulting stress gradient provides a driving force for mass flow to the neck formed between contacting particles so that the pore area fills with material and the density increases [1]. Sintering stress arises from interfacial energies acting over curved surfaces and in many equations proposed by several researches, for predicting the sintering stress, it is in function of porosity, surface energy, particle shape and particle size [1] [9]. The expression of sintering stress proposed by Olevsky is given by:

$$\sigma_{\mathrm{s}} = \frac{C\rho^2}{r_0}. \tag{6.23}$$

The sintering stress is widely used for numerical simulation of stainless steel sintering, where r_0 is the average radius of the powder particles, C is a material constant dependent of the surface energy of material. Equation 6.23 is proposed for the initial sintering stage but it is also used for the intermediate and final stages in many researches [9]. Another way to present equation 6.23 is given by:

$$\sigma_{\mathrm{s}} = \frac{3\gamma_{\mathrm{s}}}{\bar{r}}\left(1-\theta\right)^2, \tag{6.24}$$

where, θ is the porosity, which is defined as the ratio of the volume of pores to the total volume, and $\bar{r}$ denotes the average void size or average particle radius [1].

For many crystalline materials, the dominant mass transport mechanism is through grain boundary diffusion, which is developed in the intermediate stage of solid-state sintering. In this research, the sintering behaviour of the selected material is dominated by grain diffusion, so the sintering stress relationship considered to be the most appropriate is one that incorporates surface tension, relative density and average grain size. For this research, sintering stress is defined as:

$$\sigma_{\mathrm{s}} = \frac{6\gamma_{\mathrm{s}}}{G}\left(1-\theta\right)^2, \tag{6.25}$$

where G is the average grain size representing the influence of grain boundary diffusion [1].

6.5.5 Grain Growth Models

Grain growth plays an important role in sintering because excessive grain size will not only obstruct the densification, but it also influences the final mechanical properties of the sintered components [9]. With the objective to apply the grain growth in FEM simulation of the sintering process, it was necessary to find an empirical equation that can accurately describe the grain size change during sintering.

Various empirical models of grain growth have been developed for different materials and based on different mechanisms. For normal grain growth, a parabolic law and a power law have been used in many studies. The ideal grain growth law relates the mean grain size to initial grain size and time. The relation is called the parabolic law model and is given by:

$$G^2 - G_0^2 = K_1 t, \tag{6.26}$$

while the power law is governed by:

$$G = K_2 t^n, \tag{6.27}$$

where the parameter G means the mean grain size at time t, G_0 is the initial mean grain size, K_1 and K_2 are material constants, and n is the grain growth exponent. The parabolic law and power law predict the grain growth in ceramics, such as alumina [1].

Here, the concern is to understand grain growth behaviour for metal alloys such as austenitic stainless steels. It is assumed that atomic diffusion in grain growth is a simple thermally activated process, therefore an Arrhenius-type grain growth equation fits well in this study. Based on different experiments, various forms of Arrhenius-type grain growth equations have been developed. For this specific case of grain growth in solid state sintering, a short description is presented (in table 6.1) for different Arrhenius-type equations in different stainless steels [1].

Table 6.1: Grain growth equation for continuous material stainless steel [1].

Number	Equation	Material	Q_G (kJ/mol)
1	$G^n - G_0^n = Atexp(-Q_G/RT)$	Austenitic Stainless Steel	310
2	$G - G_0 = At^n exp(-Q_G/RT)$	NdFeB	215
3	$\frac{dG}{dt} = \frac{Aexp(-Q_G/RT)}{G}$	Steel SS316L & SS316LB SS316 SS316L	208 316/50 280 246

In table 6.1, the parameter n is an assumed integer that, in case of austenitic stainless steel, ranges from 3 to 5, A is a material constant, Q_G is the activation energy for grain growth, R is the universal gas constant and T is the absolute temperature [1]. The grain growth Arrhenius equation chosen for this study was the number 3, given by:

$$\frac{dG}{dt} = \frac{Ae^{-\frac{Q_G}{RT}}}{G}. \tag{6.28}$$

This type of Arrhenius equation was chosen because of its good match in grain growth phenomena in stainless steel 316L.

For this differential equation it was necessary to search for experimental parameters. The parameter A is a pre-exponent constant, Q_G is the activation energy for grain growth, R is the universal gas constant, T is the absolute temperature and G is the instantaneous grain size. The pre-exponent constant is determined experimentally. In this research, the only interest is to understand the grain growth behaviour in computational simulation. Thus, it is assumed a pre-exponent factor A from the literature. Now focusing on activation energy for grain growth, it is known for stainless steel the activation energy shifts from an upper level to a lower level after a transition temperature is reached [25]. The parameters values are presented in subsection 7.3.3.

Chapter 7

Implementation

7.1 Introduction

As has been mentioned, this research is divided in two major areas: the compaction stage and the sintering stage.

For compacting the loose powder in a certain shape to form a porous body it is necessary to select a suitable model. Therefore, the modified Drucker-Prager/Cap elasto-plastic model for implementing the compaction stage was selected. It is the most adopted model for reproducing compression of a loose powder in a finite element program. This model works largely in the inelastic zone, so the elastic behaviour in the compaction stage is minimal, being predominantly characterized by the plastic behaviour. In addition to the Drucker-Prager implementation, the objective is also to estimate the density gradients. Therefore, the UVARM subroutine in conjunction with the modified Drucker-Prager/Cap elasto-plastic model is implemented, in the finite element program.

The sintering stage, which is a long process due to its slow evolution, which may last hours, follows. However, it is time-dependent and it is considered as a quasi-static problem. For implementing the sintering process considering the solid-state of sintering, many mechanisms important in sintering are taken into account. All the sintering mechanisms are implemented resorting to a user's subroutine, which is the CREEP subroutine. The implementation of this subroutine is based on the concepts presented in section 7.3. The compaction and sintering processes and auxiliary tools that were implemented in this research are explained in the following sections.

7.2 Modified Drucker-Prager/Cap Model in ABAQUS

The Drucker-Prager/Cap model is provided within the library of the commercial finite element program Abaqus. Therefore, in order to use the soil plasticity model, in the compaction stage, it is only needed material parameters. In chapter 6.4 the three surfaces that define the model were characterized: a pressure-dependent Drucker-Prager shear failure surface (F_s), a series of compression yield surfaces (F_c), and a transition surface (F_t). Volumetric strain hardening is defined by moving the cap along the hydrostatic axis. The purpose of the transition surface is to remove any singularities during numerical computations when moving from the yield surface to the failure surface. Figure 6.1 shows the surfaces defined by the modified Drucker-Prager/Cap model in ABAQUS. The three surfaces are described by the equations 6.4, 6.5 and 6.7 [4]. In this three equations, it is necessary to define the material parameters, given by:

- β is the angle of internal friction;
- d is the material cohesion;
- t is the deviatoric stress measure;
- p is the equivalent pressure stress;
- R is the cap eccentricity parameter;
- $p_a\left(\varepsilon_{\mathrm{vol}}^{\mathrm{pl}}\right)$ represents the volumetric plastic-strain-driven hardening
- α is the transition parameter

The hardening law is defined by a piecewise linear function relating the hydrostatic compression yield stress, p_b, to the volumetric plastic strain $\varepsilon_{\mathrm{vol}}^{\mathrm{pl}}$ as shown in figure 6.2. $\varepsilon_{\mathrm{vol}}^{\mathrm{pl}}|_0$ is the initial volumetric plastic strain beyond which the work hardening yield surfaces are defined. The evolution parameter, p_a is related to p_b by equation 6.6 [4].

7.2.1 UVARM Subroutine

The subroutine UVARM is used in the compaction phase. This subroutine is defined at the material part and is applied when there is a necessity of defining a user output variable. The UVARM subroutine is called at all integration points, being called multiple times for each material point in an increment, as Abaqus iterates to a converged solution [26].

In this study, the UVARM subroutine was used because there was a necessity to define output quantities that are function of any of the available integration point quantities listed in the output variables. Therefore, with the purpose of studying the density gradients the UVARM subroutine was employed.

In order to extract the values of density at every integration point it was applied a simple model that combines strains with densities. In compaction, the external physical change is a decrease in volume, so the equation that translates this assumption is given by:

$$\varepsilon_{\mathrm{z}} + \varepsilon_{\mathrm{r}} + \varepsilon_{\theta} = \frac{V_0 - V_1}{V_0}. \tag{7.1}$$

Equation 7.1 represents the fractional change in the initial volume, where ε_{z}, ε_{r} and ε_{θ} are the strains in the axial, radial and tangential directions, respectively and V_0 and V_1 are volumes of the green compact before and after the compaction respectively [21]. The expression presented in 7.1 can be manipulated and written as:

$$\varepsilon_{\mathrm{z}} + \varepsilon_{\mathrm{r}} + \varepsilon_{\theta} = \varepsilon_{\mathrm{total}} = \frac{\rho_0 - \rho_1}{\rho_1} \tag{7.2}$$

Equation 7.2 is the fractional change in the final mean density, where ρ_0 and ρ_1 are the initial and final densities of the green body. Thus, the local density distribution may be calculated from the total strain value, $\varepsilon_{\mathrm{total}}$ being defined as [21]:

$$\rho_1 = \frac{\rho_0}{1 + \varepsilon_{\mathrm{total}}} \tag{7.3}$$

The UVARM subroutine uses equation 7.3. This subroutine is an Abaqus/Standard utility that allows the determination and visualization of the density gradients. These gradients are essential to finish the compaction phase and start the sintering phase.

7.3 Sintering Stage

In this section, all the parameters necessary to implement the sintering simulation are defined. The major parameters that influence the sintering behaviour are defined: i) the elasticity and viscosity; ii) the sintering stress and transition temperature parameters; iii) the grain growth and iv) the porosity and thermal strain. All these parameters are implemented in the CREEP subroutine that is established in the sintering simulation and which is described in section 7.3.6.

7.3.1 Elasticity and Viscosity

The elastic modulus can vary directly with temperature. In other words, with the increasing of temperature the elastic modulus decreases. Additionally, the elastic modulus of a porous material is smaller than that of the bulk solid material. Many attempts have been made to relate parameters like elasticity modulus with the porosity because in the sintering stage some parameters are directly related with average porosity. However, some researches demonstrated with numerical experiments that the final result of the sintering simulation is not sensitive to small changes in elastic modulus. The constant Young's modulus is determined by:

$$E = E_0 \rho^Y, \tag{7.4}$$

where E_0 is the full density elastic modulus which will decrease as temperature increases and is approximately 140 GPa at 500 °C and the exponent Y equals 3.4 for sintered steel. For this research, ρ, the bulk density is equals to 62%. Furthermore, the constant Young's modulus equals 69.3 GPa. Additionally, a constant Poisson's ratio, 0.28, is used [1].

The apparent viscosity in a thermally activated viscous flow was modelled by the Arrehnius temperature, equation 6.20. Some material parameters constants are employed in the Arrhenius temperature relation, which are the pre-exponential factor, η_0, that usually takes the value of 790 MPa.s and the activation energy, Q_v, that is equal to 20.0 kJ/mol [1].

7.3.2 Porosity/Relative Density

In every time increment, the porosity/relative density is updated using the strain component. In the sintering stage, geometric nonliearity should be accounted for, due to large deformation during the evolution of the sintering cycle. The relative density can be described in terms of logarithmic strain components as:

$$\rho = \rho_0 e^{(-\varepsilon_{\mathrm{kk}})}, \tag{7.5}$$

where ρ_0 is the initial relative density, ρ is the final relative density, and $\varepsilon_{\mathrm{kk}}$ is the volumetric strain. When this relation is implemented in CREEP subroutine, $\varepsilon_{\mathrm{kk}}$ is approximated by the swelling strain $\bar{\varepsilon}^{\mathrm{sw}}$, which is updated at the beginning of each increment [1].

7.3.3 The Grain Growth Model

The grain size is updated using the Arrhenius type equation grain growth that is shown in equation 6.28. For this empirical differential equation, some material constant parameters must be defined. The pre-exponent constant, A, is determined experimentally. In this research, the only interest is understanding the grain growth behaviour in computational simulation. Therefore, a pre-exponent for stainless steel powder was adopted, in this case equal to $6,75 \times 10^{-13}$ m^2/s. The activation energy for grain growth, Q_G, is 316 kJ/mol for temperatures less than approximately 1200 °C and 50.0 kJ/mol when temperatures are greater than approximately 1200 °C.

7.3.4 Sintering Stress

The sintering stress used in the sintering stage is described by equation 6.25. This sintering stress, σ_s, is related directly with surface tension energy, average grain size and relative density. The relative density is updated using the volumetric strain components (relation 7.5). The surface tension energy, γ_s, is a constant parameter and in the sintering stage a value of 2.0 J/m^2 is applied.

7.3.5 Thermal Strain

The thermal strain, $\Delta\varepsilon^\mathrm{t}$, is caused by expansion/contraction and it can be expressed by:

$$\Delta\varepsilon^\mathrm{t} = \alpha\Delta T, \tag{7.6}$$

where α is the thermal expansion coefficient and ΔT is temperature increment. Based on the assumption of the transition temperature for sintering stress, the thermal expansion dominates at low temperatures, i.e, temperatures below the transition temperature. The temperature dependent behaviour of the thermal expansion coefficient can be determined by experiments carried out in the dilatometer. For this research, experimental data is adopted from the literature. In the literature, the conclusion was that the thermal expansion coefficient of a porous material is in general slightly smaller than that of the fully dense material. For this research, the major concern is in the deformation due to sintering, considering that the thermal deformation is not the main concern taking into account the deformations acting in the sintering stage. So, a linear empirical equation is applied to describe the thermal expansion coefficient as a function of temperature by:

$$\alpha = c_1 T + c_2, \tag{7.7}$$

where C_1 and C_2 are measured material constant taken from experiments. For this research, and for a material like stainless steel, C_1 assumes the value $4.47 \times 10^{-9} K^{-2}$ and C_2 is $12.1 \times 10^{-6} K^{-1}$ [1].

7.3.6 CREEP subroutine

In order to employ the model presented in section 6.5, the Abaqus subroutine CREEP is used. User subroutine CREEP will be called at all integration points of elements for which the material definition contains user-subroutine-defined metal creep and time-dependent volumetric swelling, during procedures that allow viscoelastic response of the types referenced to occur (such as the quasi-static procedure). The user subroutine is applied to define a material behaviour that can be used in the coupled-temperature displacement.

For metals, the incremental creep strain routine allows swelling and creep as defined in 7.8 [1].

$$\Delta\varepsilon^{\mathrm{cr}} = \frac{1}{3}\Delta\bar{\varepsilon}^{\mathrm{sw}}\mathbf{R} + \Delta\bar{\varepsilon}^{\mathrm{cr}}\mathbf{n} \tag{7.8}$$

Equation 7.8 is defined as $\Delta\bar{\varepsilon}^{\mathrm{sw}}$ being the incremental volumetric swelling strain and $\Delta\bar{\varepsilon}^{\mathrm{cr}}$ the uniaxial equivalent creep strain. The incremental volumetric swelling strain and the uniaxial equivalent creep strain are defined by the user in the subroutine based on the creep model. For isotropic swelling $\mathbf{R}$ becomes the unit matrix $\mathbf{I}$. The gradient of the deviatoric stress potential $\mathbf{n}$ is defined in relation 7.9 [1].

$$\mathbf{n} = \frac{\partial\tilde{q}}{\partial\boldsymbol{\sigma}} = \frac{3\boldsymbol{\sigma'}}{2\tilde{q}} \tag{7.9}$$

In relation 7.9 the deviatoric stress is given by:

$$\boldsymbol{\sigma'} = \boldsymbol{\sigma} + p\boldsymbol{I}, \tag{7.10}$$

where $p = -\frac{1}{3}tr(\boldsymbol{\sigma})$ is the equivalent pressure stress. The equivalent deviatoric stress is given by:

$$\tilde{q} = \sqrt{\frac{3}{2}\boldsymbol{\sigma'}\boldsymbol{\sigma'}}. \tag{7.11}$$

In this thesis, the creep rate equation (6.19) is shown as the incremental form of the creep strain rate:

$$\Delta\varepsilon^{\mathrm{cr}} = \frac{tr(\boldsymbol{\sigma})\Delta t - 3\sigma_{\mathrm{s}}\Delta t}{9\eta_{\mathrm{b}}}\boldsymbol{I} + \frac{\boldsymbol{\sigma'}\Delta t}{2\eta_{\mathrm{s}}}. \tag{7.12}$$

A comparison between equations 7.8 and 7.12 leads to the following relations: 7.13 and 7.14.

$$\frac{tr(\boldsymbol{\sigma})\Delta t - 3\sigma_{\mathrm{s}}\Delta t}{9\eta_{b}}\boldsymbol{I} = \frac{1}{3}\Delta\bar{\varepsilon}^{\mathrm{sw}}\boldsymbol{R} \tag{7.13}$$

$$\frac{\boldsymbol{\sigma'}\Delta t}{2\eta_{\mathrm{s}}} = \Delta\bar{\varepsilon}^{\mathrm{cr}}\boldsymbol{n} = \Delta\bar{\varepsilon}^{\mathrm{cr}}\frac{3\boldsymbol{\sigma'}}{2\bar{q}} \tag{7.14}$$

Therefore, the incremental volumetric swelling strain $\Delta\bar{\varepsilon}^{\mathrm{sw}}$ and the uniaxial equivalent creep strain $\Delta\bar{\varepsilon}^{\mathrm{cr}}$ can be written as shown in 7.15 and 7.16.

$$\Delta\bar{\varepsilon}^{\mathrm{sw}} = \frac{tr(\boldsymbol{\sigma}) - 3\sigma_{\mathrm{s}}}{3\eta_{\mathrm{b}}}\Delta t = -\frac{p + \sigma_{\mathrm{s}}}{\eta_{\mathrm{b}}}\Delta t \tag{7.15}$$

$$\Delta\bar{\varepsilon}^{\mathrm{cr}} = \frac{\tilde{q}}{3\eta_{\mathrm{s}}}\Delta t \tag{7.16}$$

The equivalent pressure stress p and the Mises equivalent deviatoric stress $\tilde{q}$ are internal variables in the creep soubroutine. They are applied in the subroutine from the main program in every increment. In the subroutine, the shear viscosity modulus η_{s}, the bulk viscosity modulus η_{b}, and the sintering stress σ_{s} are also introduced and all are based in equations 6.21, 6.22 and 6.23. The sintering stress is called at all integration points of the element at each time increment [1].

7.3.7 Creep Subroutine Architecture

The creep subroutine was implemented into the sintering stage. In the creep subroutine was essentially written the viscoelastic model described in 6.5.1. The viscoelasticity model was built under a conventional model presented in the next topics. Thus, the implementation of the viscoelasticity model in the subroutine followed a specific order:

First Load the material constants, which are: initial grain size (G_0); pre-exponent factor (A); activation energy for viscous flow (Q_v); a pre-exponential material constant (η_0) and the universal gas constant (R);

Second The grain growth behaviour. The Arrhenius equation that controls the grain size is applied (equation 6.28) and the activation energy (Q_G) in function of the transition temperature is written;

Third The surface tension energy (γ_{s}). Surface energy is activated when temperature is above of the transition temperature;

Fourth In this point, the principal mechanism written in the creep subroutineis explained. The objective is to determine the porosity, and consequently the density. In the sintering simulation the density is updated at every increment using the relation refereed in 7.5. In the creep subroutine, the parameter $\varepsilon_{\mathrm{kk}}$ is assumed to be equal to the swelling strain $\bar{\varepsilon}^{\mathrm{sw}}$ and it is known that the swelling strain that is updated at the beginning of each increment is given by equation 7.15. The swelling strain is directly dependent on the viscosity modulus (6.22) and on the sintering stress (6.25). On the other hand, the viscosity modulus and the sintering stress are directly dependent on the viscous flow (equation 6.20), and on the average grain size (equation 6.20), that are also dependent of porosity (θ) and surface tension energy (γ_{s}). With this description it is noticed that all equations are dependent on one of the others for certain parameters, and one of them is the porosity that are intimately connected with density. Therefore, it was necessary to resort to an iteration method to estimate the value of porosity, and with that, calculate all the material equations refereed before. Thus, the bissection method was applied for estimating the value of porosity. With the porosity estimated, the viscous flow (η) was easily calculated followed by the viscosity modulus (η_{b}). Next, the sintering stress (σ_{s}) is calculated based on the estimative of porosity (θ) and the second and the third topics, already described, were also calculated. With these values, the swelling strain($\bar{\varepsilon}^{\mathrm{sw}}$) necessary for determining the density is calculated. When the value of density (ρ) is determined, the porosity (θ) value is calculated and that value is used for calculating another iteration using the bissection method;

Fifth Update the value of the volumetric swelling strain $\Delta\bar{\varepsilon}^{\mathrm{sw}}$ (equation 7.15) and calculate the value of the uniaxial equivalent creep strain $\Delta\bar{\varepsilon}^{\mathrm{cr}}$ (equation 7.16);

Sixth Define the values of relevant parameters in solution-dependent variables (SDV).

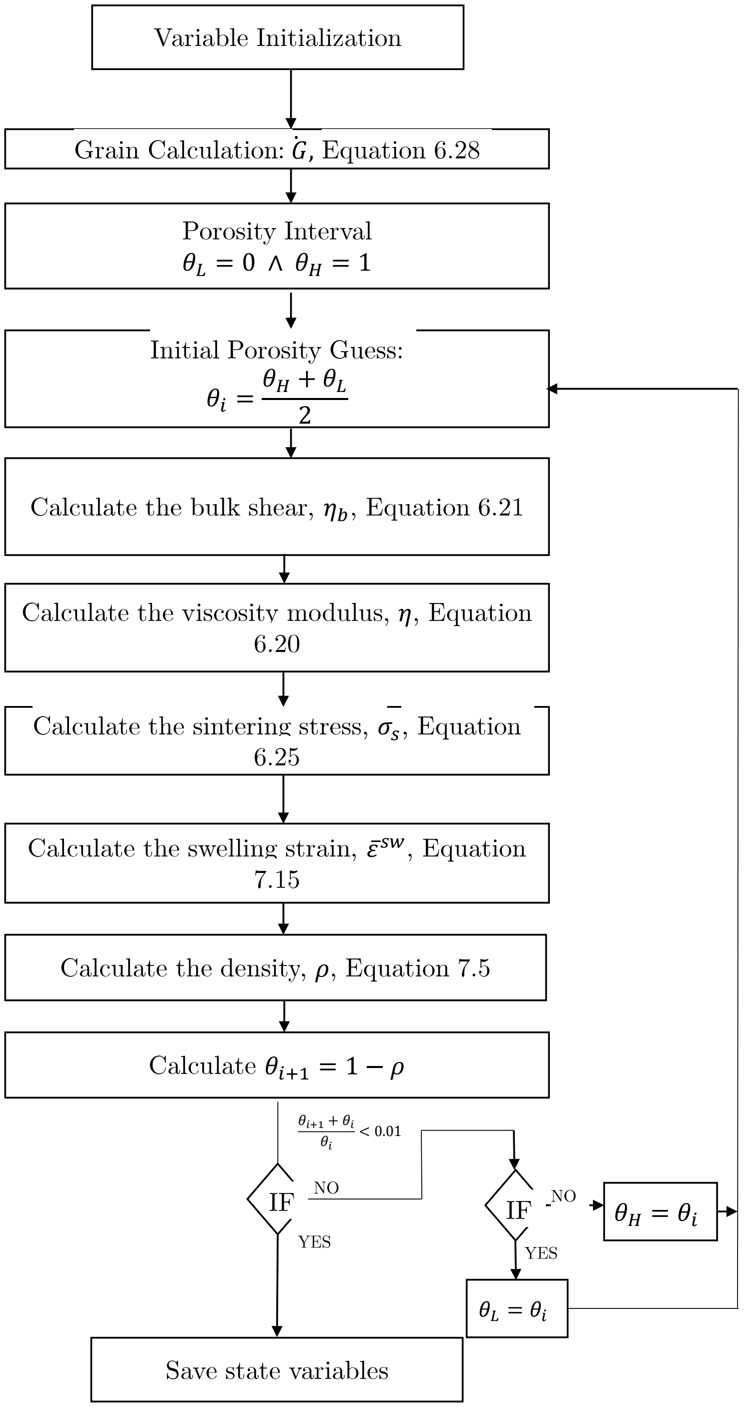

Figure 7.1: Schematic for the iteration process.

7.3.8 Bissection Method

As was refereed before, the implementation of the viscoelastic model follows a specific order in the calculation process. It should be noticed that the shear modulus, the viscosity and the sintering stress are dependent of porosity. However, the porosity variable is determined in the last part of calculations in the creep subroutine. Consequently, an iterative process is required and an initial estimative has to be made. In order to implement a robust and methodical iterative process the bissection method is used. This method consists in building subintervals, $I_k = [a_k, b_k] \in I$, through successive divisions in the middle of the interval. Thus, the value that is to be estimated is confined in intervals as small as we wish.

The algorithm that describes this method is:

1. $I_0 = [a_0, b_0] = [a, b]$;

2. $I_k = [a_k, b_k]\,, k = 1, 2, ...$, and consider x_{k+1} the midpoint of the interval I_k,

$$x_{k+1} = \frac{a_k + b_k}{2} \tag{7.17}$$

Considering, in equation 7.17, that it is possible to define $a_{k+1} = a_k$ and $b_{k+1} = x_{k+1}$, and, on the other hand define $a_{k+1} = x_{k+1}$ and $b_{k+1} = b_k$. In these two scenarios, a new interval $I_k = [a_{k+1}, b_{k+1}]$ is built, where the precise value that is wanted is contained. The new subinterval has a length, that is half the length of the previous subinterval, which is shown in relation:

$$|a_{k+1} - b_{k+1}| = \frac{1}{2}|a_k - b_k|. \tag{7.18}$$

In summary, this method generates from the initial interval $I_0 = [a, b]$ successive intervals $I_{k k=1,2,...}$ verifying $I_0 \supset I_1 \supset I_2 ...,$, where there is an $\alpha \in I_k, k = 0, 1, 2, ...$, such that $f\,(\alpha) = 0$.

7.4 Implementation

In the previous sections, the models used in the compaction and sintering stages were demonstrated. Now, the kinetics of the two stages is presented, resorting to a schematic in figure 7.2, and the work developed in the implementation is explained with special focus in the applied subroutines. All the research work was done resorting to a finite element program and, essentially, using subroutines as auxiliary tools.

Beginning on the compaction stage, the main goal was to compact the loose powder. For compacting the loose powder the criteria of soils plasticity was applied. The main goal was to study the density gradients at the end of the compaction stage, when the specimen is free of rigid bodies. Therefore, to study the density gradients it was necessary to apply a subroutine, UVARM, on the model. It was important to save the densities in a database because in the second stage there is an input of the density gradients from the compaction stage. Therefore, a subroutine called WRITE was created for writing the density values from every element in the final of compaction stage. At this point, the compaction stage ends and the sintering stage begins. Before starting the sintering stage an input of the information needed from the previous stage was made. The orphan mesh and residual stresses were loaded from the compaction simulation. These two informations were placed in the sintering input file. The density values written in database from the last increment of the compaction stage were also loaded for the sintering simulation. For loading the values, another subroutine, called READ, was created. This subroutine has the task of reading the values of density that were in database. The READ subroutine was placed into the main subroutine CREEP. The subroutine CREEP along with the subroutine READ and the information loaded from the compaction stage were fundamental for creating the sintering simulation.

It is possible to see the previous explanation of the implementation work in schematically in figure 7.2. The user subroutines UVARM and CREEP are described more detailed in sections 7.2.1 and 7.3.6.

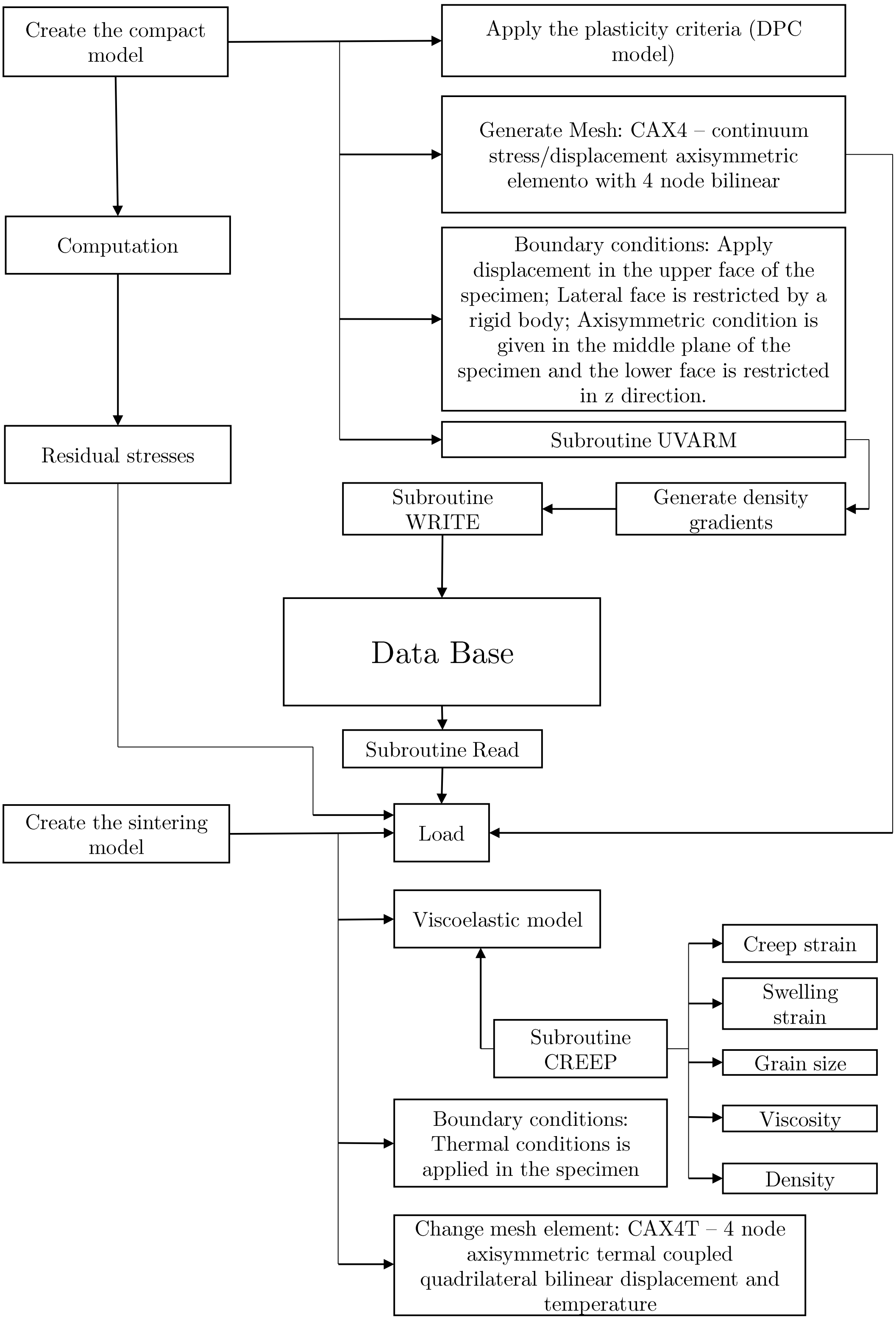

Figure 7.2: Schematic of the developed implementation.

7.5 CREEP Subroutine Validation

The implemented models validation is crucial. For material models implemented using user's subroutine (CREEP) is extremely important to perform some control tests. Thus, in a first phase, the CREEP subroutine is validated in a simple model. After the CREEP subroutine is calibrated for this model, it is then applied in the case study presented in section 8.2.

Therefore, the test is realized in a specimen with a unitary dimension. For validating this test, a minimum number of elements is applied just for avoiding locking effects. For this test, four elements CAX4T were applied. This test consists in a displacement in the vertical direction. The bottom of the specimen is restricted in x and y directions. For testing the temperature field, a temperature starting at room temperature, around 18 °C and growing until to 1000 °C is applied.

Here, the main concern is to understand the subroutine's mechanical behaviour. So, the creep and the swelling strain were taking into account for analysing the results, consistency and verifying the implementation. The results are presented in a graphic way like shown in figure 7.4 and 7.5. They represent the swelling and creep strain control along the heat cycle.

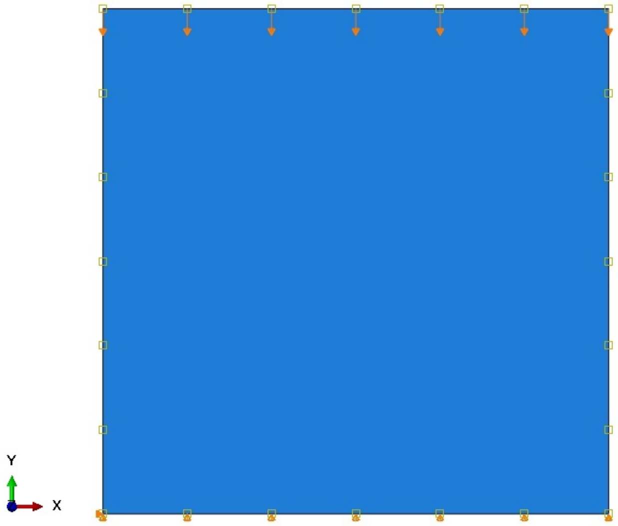

Figure 7.3: Boundary conditions of the specimen.

In the initial tests, the values of swelling and creep strain were extremely exaggerated. This was due to the material parameters not being in a coherent unit scale. After calibrating the material parameters, new tests were performed, and a new problem in calculating the porosity was identify. In a first phase, the porosity value was not correct, and with incorrect value in porosity, others parameters were influenced and with that, the swelling and creep strain were also influenced. Therefore, a calibration of the iterative method for extracting the correct value of porosity was performed. With that, the creep and swelling values starting assuming the values as presented in figure 7.4 and 7.5.

Furthermore, the swelling and creep strain represent the most important variables in the subroutine CREEP. The swelling and creep strains increments are given by relations 7.15 and 7.16 referred in section 7.3.6. The swelling strain is not represented in absolute value, so assumes negative values, like represented in figure 7.4. In relation 7.15 it is obvious that the swelling strain is directly dependent of the equivalent pressure stress (p), of the sintering stress (σ_{s}) and of the viscosity modulus (η_{b}). Therefore, in this test, an initial pressure in the upper surface was applied, like shown in figure 7.3. This pressure was applied with the objective to start the swelling strain behaviour at 0 seconds. If this initial pressure did not exist the swelling strain would just start when the transition temperature was reached, because that is when the sintering stress starts to have effect. At this point, the interest is not in a typical sintering behaviour but in accurate values. In the graphic 7.4, the swelling strain takes values relatively acceptable for this initial test. So, it is also concluded that the viscosity modulus, which is influenced by the Arrhenius equation is working well. The sintering cycle does not have much influence in this test, because it was just given a ramp of heating to 1000 °C and the sintering stress just starts to work at 918 °C. So, the control on the sintering stress may not be accurate.

The creep strain is dependent on the equivalent deviatoric stress and on the shear modulus. Like was explained in the swelling strain, applying an initial pressure influenced the creep strain. The creep strain's behaviour, like in the swelling strain, starts at 0 seconds influenced by the equivalent deviatoric stress. Here, the concern was to control the shear modulus, that is given by the porosity and Arrhenius equation. Therefore, the control in the creep strain was precise in the porosity and in the Arrhenius equation. So, while for the swelling strain the adjustments had to be made, in the creep strain this was not necessary.

This validation test was mainly general, not fully demonstrating the actual influence of the CREEP subroutine in the sintering process simulation. Here, the objective was for adjusting material parameters, adjusting the units, calculating the porosity with the bisection method and observing how the creep and swelling strain behave. In fact, there is not a reference value for comparing the values presented in figure 7.4 and 7.5, so they were assumed correct for implementing the creep subroutine in the case study.

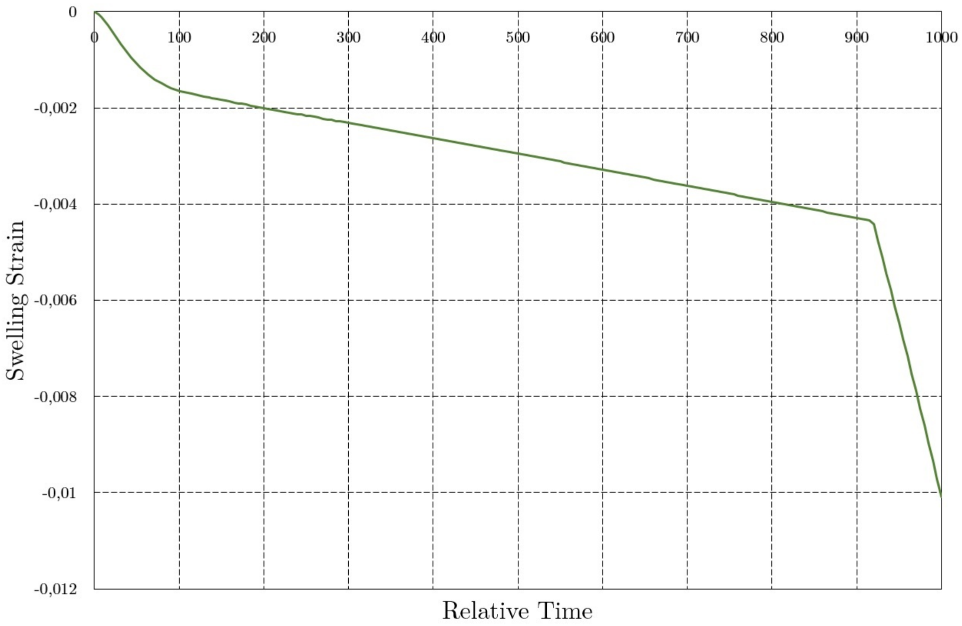

Figure 7.4: Swelling strain behaviour along the heat step.

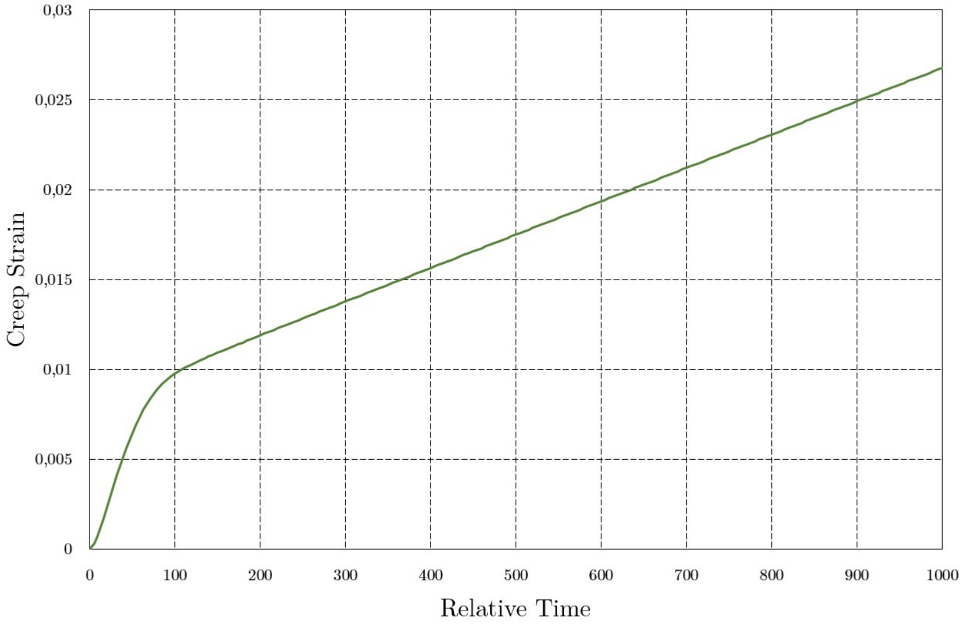

Figure 7.5: Creep strain behaviour along the heat step.

Part III

Results and Discussion

Chapter 8

Problem Description and Discretization

8.1 Introduction

In this chapter, the geometrical model is discretized, where the compaction and sintering models presented in sections 7.2 and 7.3, were validated. It starts with simple geometries, for validating a material model, like described in subsection 7.3.6. Most of the geometrical models used for validating subroutines like the one used in this work (CREEP subroutine) are axisymmetrical models. Usually, the geometrical model is a simple disk, that is subjected to a compaction test and, subsequently, to a sintering process. The disk could have a simple geometry, i.e., without an interior section or be more complex and have a cavity. For this work, it is also adopted a simple disk, without any cavity, because it is the most used geometrical model for beginning studies in this field.

Furthermore it is also important to describe the model in what comes to the level of steps and boundary conditions applied in the finite element program. As it was said along this work, it is important to define the problem in a compaction process and in a sintering process. Firstly, the boundary conditions in the compaction process are presented. These are mainly mechanical conditions and are presented in subsection 8.2.1. Following on, the thermal conditions used in the sintering process are presented in section 8.2.2.

8.2 Case study

The model adopted for implementing all the concepts that were described in previous chapters was an axisymmetric model, more specifically a cylindrical specimen as shown in figure 8.1.

8.2.1 Compaction Simulation

In the specimen shown in figure 8.1, an elasto-plastic criteria based on the modified Drucker-Prager/Cap described in 7.2 was implemented. A user's UVARM subroutine

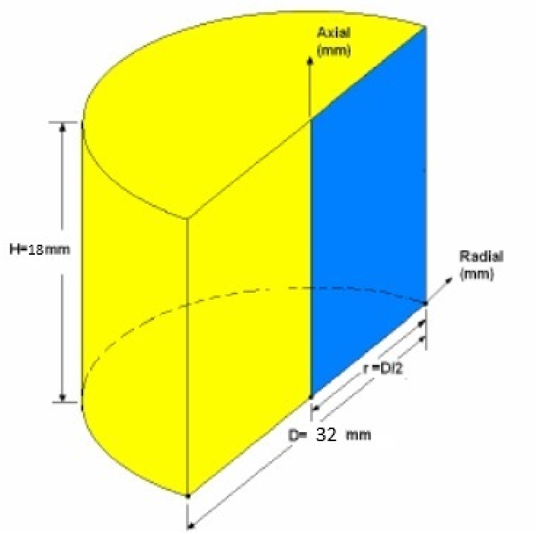

Figure 8.1: Specimen geometry, adapted from [1].

was also implemented and is described in 7.2.1. These two topics, explained in chapter 7, describe the material behaviour along the compaction simulation.

Uniaxial die compaction in a single act was applied in the loose powder. Therefore, the upper punch performs the movement of compressing the loose powder. The lower punch and the die do not move along the process of compaction, except in the end of the of compaction stage, when the powder is already compacted and the punches release the green body.

For simulating the compaction process 3 steps were necessary, and each one had a relative time of 1 second. In the first step the tools were assigned. The objective here was to reproduce the contact of the punches and of the die cavity with the loose powder (the specimen). Therefore, an interaction on the die surface with the specimen was used and the condition for the lower and upper punches was applied. In the compaction simulation process, the rigid tool that simulates the lower punch for holding the specimen was substituted for a boundary condition, where the displacement in the $z - direction$ was restricted. In the second step, the compaction movement was realized, this is, the upper punch realized the movement of compression on the loose powder. In this step, the loose powder gained the shape of the die cavity. For that, a displacement in the upper surface was applied to simulate the movement of the punch compacting the specimen. At last, in step 3 the tools were released, and left the specimen relaxation. In this step, the movement of the upper punch was deactivated. A displacement was applied in the die surface with 3 mm in the $r - direction$ and the lower punch stayed, with the boundary condition of the first step applied, in the bottom of the specimen. In figure 9.19, the movements of the tools in the simulation of the compaction process are graphically represented .

Like was said in the previous paragrapher, in an attempt to simplify the compaction simulation process, the upper punch and the lower punch were substituted for rotation/displacement boundary conditions. This solution simplified the global convergence of the simulation, because the contact interactions were limited to the die and the specimen, where there is a real interest in understanding the friction between these two surfaces. Therefore, the convergence in contact interactions is faster, simplifying the global convergence of the problem. For the compaction simulation, the boundary conditions and loading conditions are represented in figure 8.2.

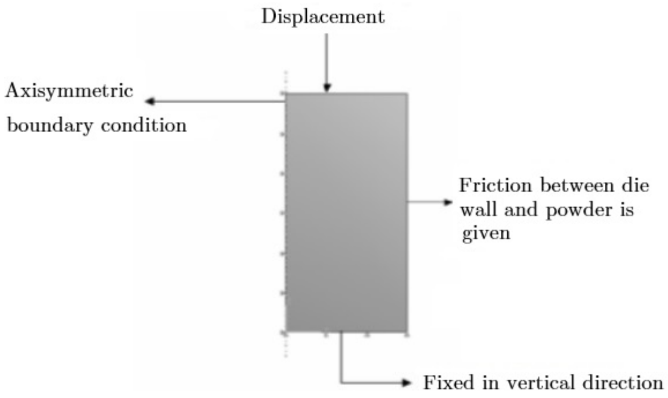

Figure 8.2: Boundary conditions for single acting compaction process, adapted from [27].

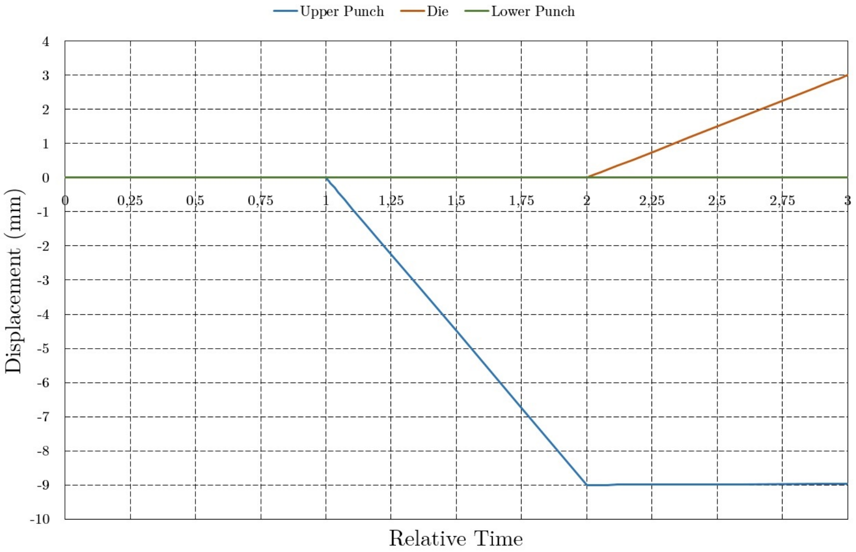

Figure 8.3: Movement of the punches.

The case study presented in figure 8.1 is an axisymmetric specimen, thus, the element types available are restricted to axisymmetric elements. In axisymmetric problems, it is necessary to consider that coordinate 1 is r and coordinate 2 is z. At $\theta = 0$ the $r - direction$ corresponds to the global $x - direction$ and $z - direction$ corresponds to the global $y - direction$. This is important when data is given in global directions [26]. So, the element type applied in this case study was a continuum stress/displacement, axisymmetric with nonlinear and 4 nodes bilinear that defines the element CAX4. It was selected complete integration instead of reduced integration because the accuracy with complete integration is better than with reduced integration. In reduced integration, there is just one point of calculation in all the element, therefore the computation time is faster comparatively to complete integration which has four points of calculation in all the element.

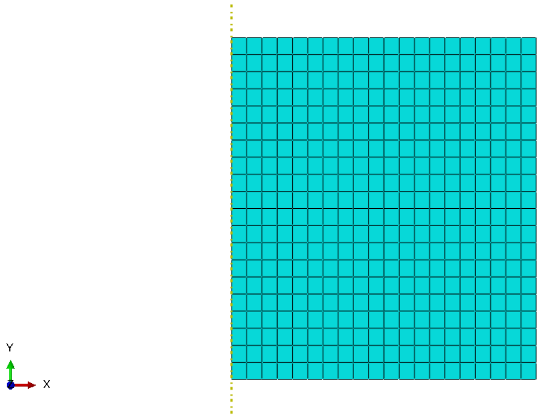

Figure 8.4: Specimen meshed with CAX4 elements.

With the objective of having an accurate simulation, in a first phase an intermediate mesh was established, i.e., neither a coarse mesh, that leads to low accuracy results, neither a mesh with excessive elements, that requires a larger computational time. For this case study a mesh with 648 elements and 700 nodes was used, concluding that will be the most adequate mesh to obtain results.

8.2.2 Sintering Simulation

In the sintering process simulation, the geometry adopted was imported from the compaction process simulation. Therefore, after the compaction simulation the model is passed to the sintering simulation. In practical terms, the specimen where the sintering behaviour is applied is shown in figure 8.5.

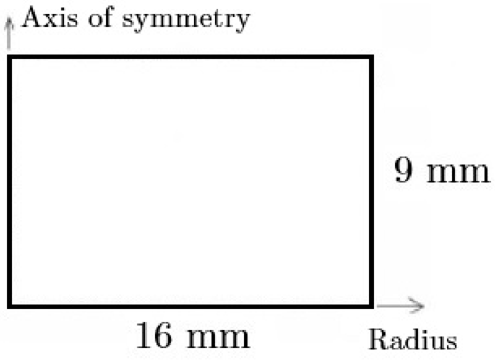

Figure 8.5: Geometry for the sintering simulation.

The boundary conditions applied on the green body are divided into two parts, as expressed by:

$$\Gamma = \Gamma_c + \Gamma_f, \tag{8.1}$$

where Γ is the total surfaces of the sintering body, Γ_c is the surfaces contacted with the surface of the chamber, Γ_f is the free surfaces exposed in the sintering atmosphere [9]. Equation 8.1 is illustrated in figure 8.6.

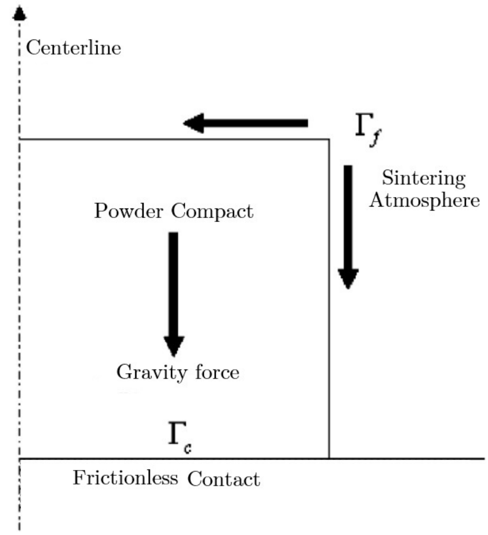

Figure 8.6: Description of boundaries in the sinterning model.

Relatively to thermal boundary conditions it is established that the temperature of the sintering body changes with the thermal cycle in the furnace. The parts absorb the heat via thermal conduction, convection and radiation. The thermal boundary conditions can be expressed as:

$$\forall \bar{X} \epsilon \Gamma, T = f\left(\bar{X}, t\right), \tag{8.2}$$

where $f\left(\bar{X}, t\right)$ is the temperature distribution function, $\bar{X}$ is the spatial position in the model and t is the time. For the sintering of small components, the temperature gradients in the sintering body are small unless the heating process is very quick. However, there are, usually, temperature gradients in the furnace [9].

The sintering process simulation were divided in two steps defined by coupled temp-displacement. In the first step, the heating ramp and the holding time were applied, so this step had a time period of approximately 11592 seconds corresponding to 2 hours and 20 minutes of heating ramp at 10 °C and 1 hour of holding time. The second step is the cooling step, where another 2 hours and 20 minutes of cooling ramp were applied. The two steps applied in this sintering process simulation have basis on the ideal sintering cycle shown in figure 8.7.

Relatively to the mesh of the specimen in the sintering simulation, as was previously referred, the geometry was imported from the compaction simulation. So, the mesh was also imported from the compaction stage. Therefore, after the compaction simulation finished the deformed mesh is imported to the sintering simulation, so the number of nodes and elements stays constant. The only change is due to the type of element.

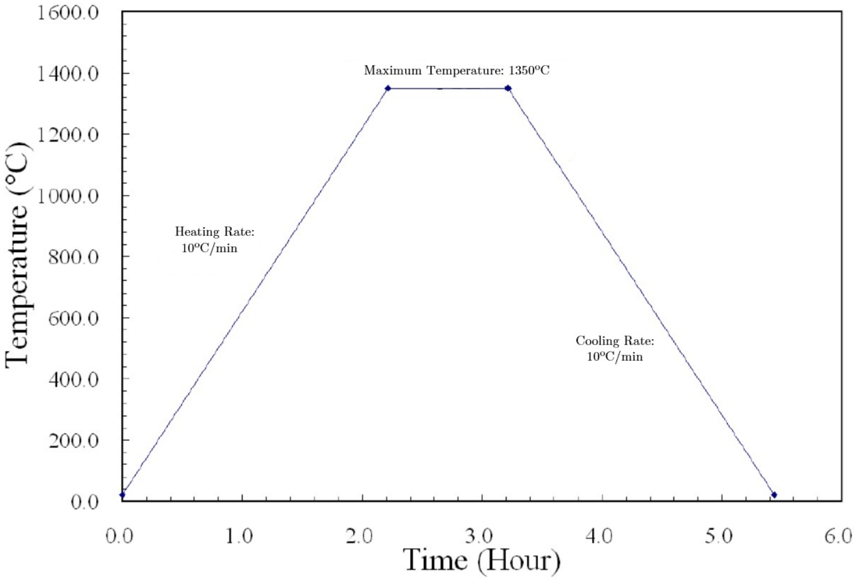

Figure 8.7: The ideal sintering cycle applied in the sintering process simulation, adapted from [1].

For sintering simulation, a coupled thermal/displacement element like the CAX4T was applied. This element is characterized for 4-node bilinear displacement temperature.

8.3 Model Validation

After all descriptions presented in previous sections about the implementation of powder metallurgy, it is now necessary to validate the model. Therefore, an initial validation with a single element in the disk model in section 8.2 was conducted considering all the conditions explained in subsections 8.2.1 and 8.2.2. This validation test is essential before starting the analysis of the model with all sensibility considerations. It is not possible to validate the compaction and sintering model for an exhaustive analysis if the model is not controlled for the simplest case. After an initial validation and understanding that all the mechanisms implemented are properly controlled, it follows the same proceeding for the disk case.

This validation process starts with the compaction process simulation. The model of compaction is presented in figure 8.8. In this first part of the work it is necessary to interact the UVARM subroutine with the compaction simulation, with the objective to control the density increase along the compaction process. Other variables like von Mises stresses, and total strains are also important to take into account.

The control made in this phase was about the variables that were necessary to monitor in the compaction process. Therefore the control of relative density (figure 8.9), plastic volumetric strain (figure 8.10) and axial pressure (figure 8.11) is presented.

In figure 8.9, the relative density behaviour increased as expected. The relative density increased, essentially, during the second step, when the loose powder was compacted. The increase in relative density, is intimately related with the plastic volumetric strain. Therefore, when the plastic volumetric strain started to increase the relative density

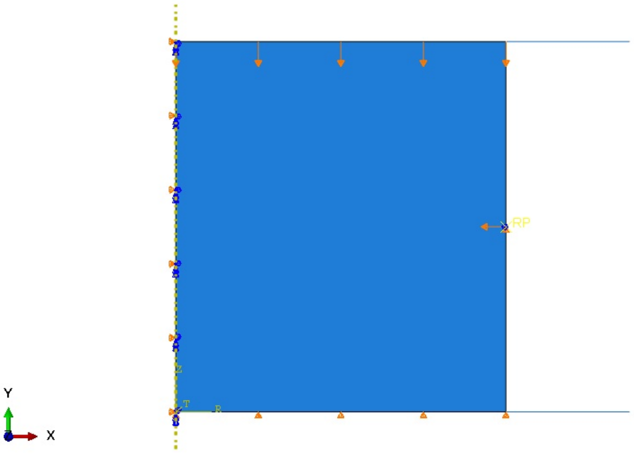

Figure 8.8: Compaction model for the validation test.

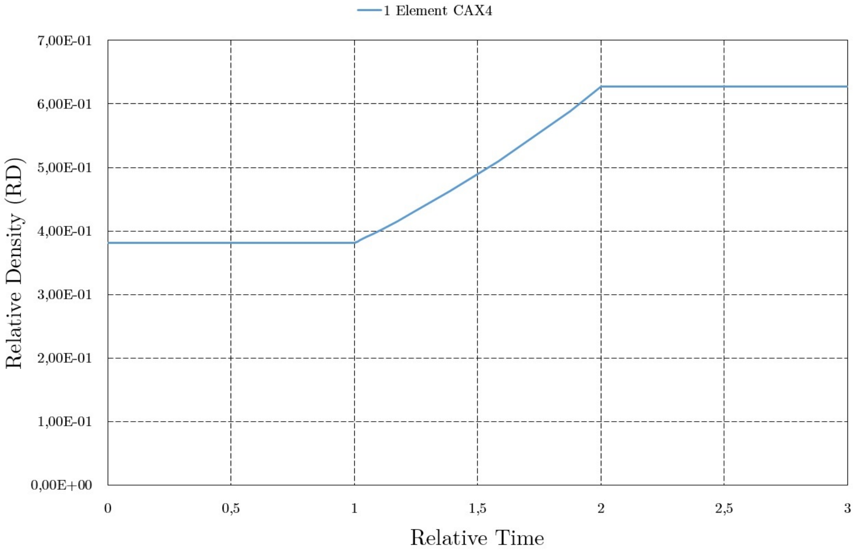

Figure 8.9: Relative Density along the compaction process simulation.

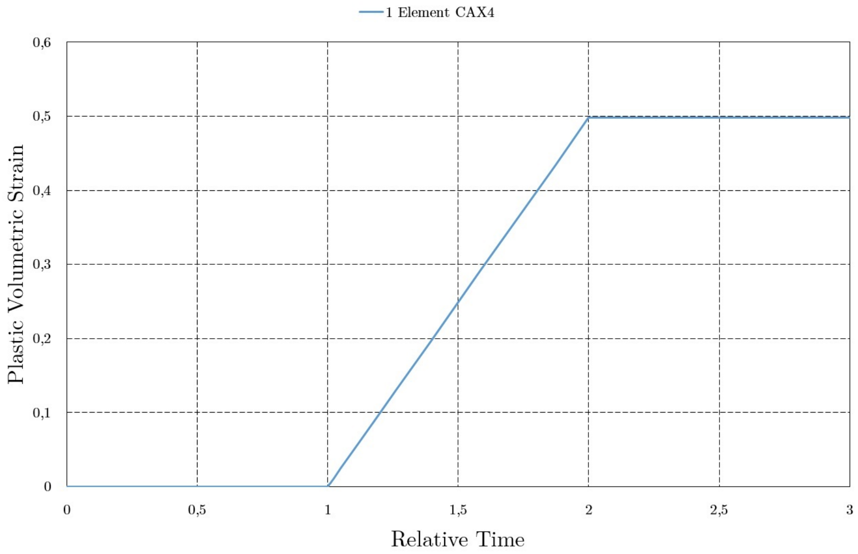

Figure 8.10: Plastic volumetric strain behaviour in the compaction process simulation.

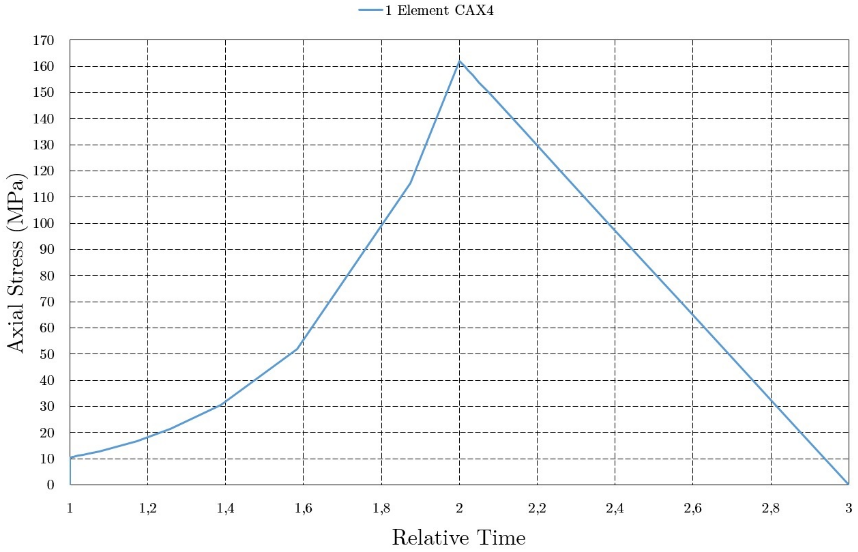

Figure 8.11: Axial stress behaviour in the compaction process.

also started increasing. The plastic volumetric strain behaviour (figure 8.10) matched perfectly with the relative density behaviour (figure 8.9). Finally, in this validation test, the axial stress was verified. The axial stress (figure 8.11) had the expected behaviour, this is, it increased along the compaction movement, and decreased when the compact is released. Hence, the compaction simulation model had the expected behaviour, and were created conditions in the compact for starting the sintering process simulation.

After controlling the model in the compaction process simulation, it is now necessary to control the model in the sintering stage. The sintering stage is more critical than the compaction stage because there are some material variables to control. Therefore, a first approach was made in subsection 7.5 for controlling the model material variables (CREEP subroutine), but for a insignificantly example. In this stage, the objective is to control the sintering variables for 1 element model for controlling the CREEP subroutine, but for a sintering process done after the compaction stage. Therefore, two variables, in specific, were controlled: the swelling and creep strain that are essential for the good behaviour of the sintering process simulation. After this control, just for prevention, the relative density was analysed, demonstrating that the relative density still increases in the sintering process.

It is noted in figure 8.12 and 8.13 that the strains had an acceptable behaviour for the implemented material model. At this point, it was not an objective to enter in details about the behaviour of these two strains, but it is noted that the swelling and creep strains started increasing when the Arrhenius equation had influence in the sintering process and the porosity started decreasing with the beginning of grain growth. This led to the start of the relative density in the sintering process simulation.

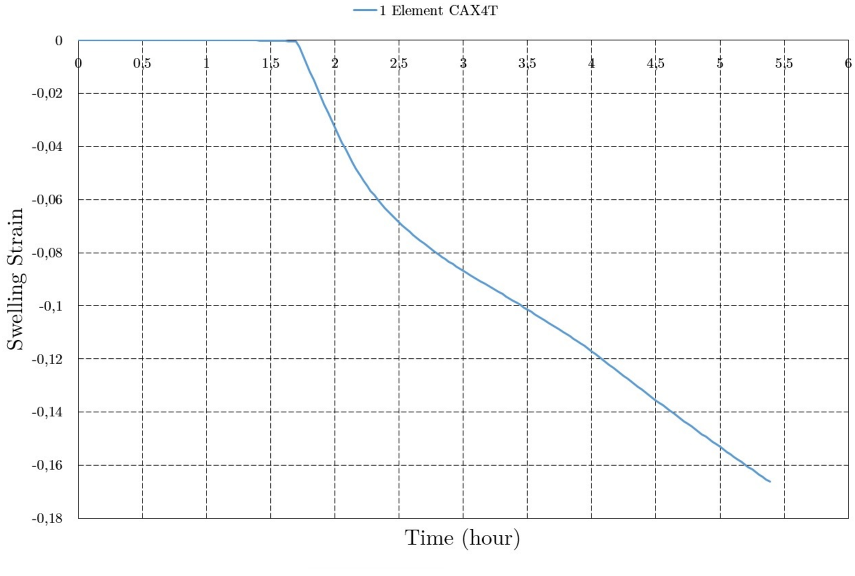

Figure 8.12: Swelling strain during the sintering process simulation.

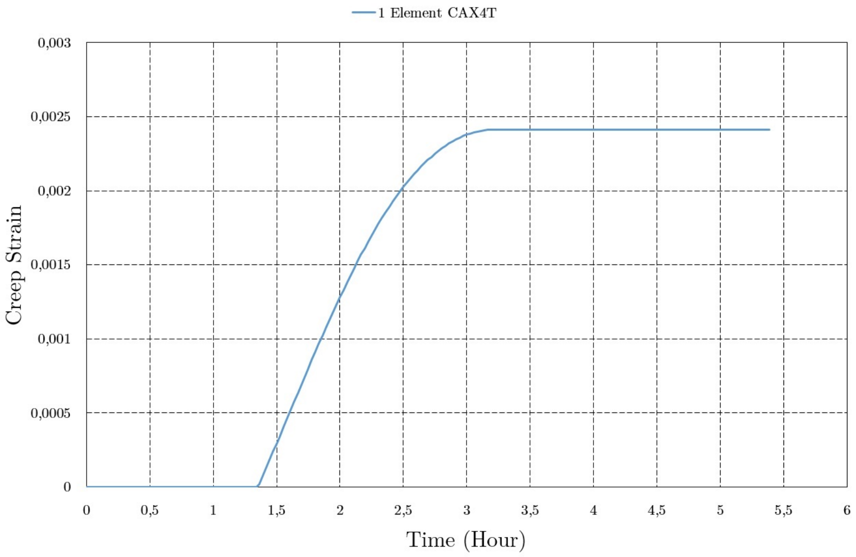

Figure 8.13: Creep strain during the sintering process simulation.

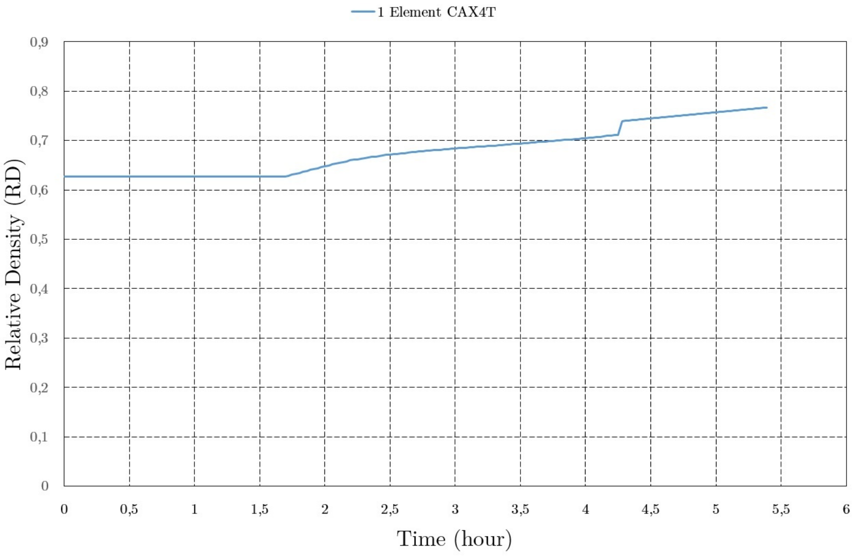

Figure 8.14: Relative density increases during the sintering process simulation.

Chapter 9

Case Study Analysis

9.1 Introduction

After all implementation tests were validated, it is now time for validating the model with the necessary conditions for a careful analysis in the compaction process simulation (section 9.2), and in the sintering process simulation (section 9.3). All the model discretization was done in chapter 8. This chapter is essentially presented for an assertive discussion of results. In a first phase, the compaction stage and the following sintering stage are discussed in detail. First, this discussion is focused on the accuracy of the mesh, like was explained in section 8.2.1, where four selected elements were analized (figure 9.1). Following, a sensitivity study is made (section 9.4), where the objective is now focused on the mesh accuracy.

9.2 Compaction Stage Analysis

In order to start the compaction stage analysis, the centroids of four elements of the mesh applied on the specimen were chosen. The elements selected for this analysis can be seen in figure 9.1.

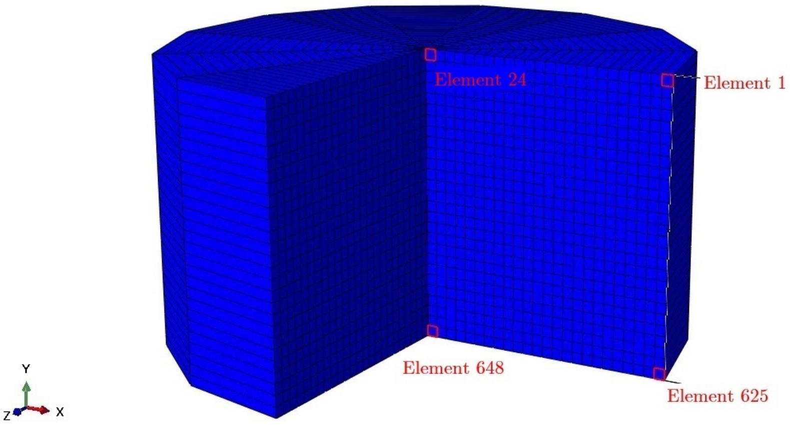

Figure 9.1: Four critical elements selected.

The initial relative density is established at 0.381. When the compaction process begins, the relative density behaviour tends to increase, i.e., when the upper punch starts the downward movement, the density automatically starts to increase.

Initially, there is a completely porous body. At the beginning of the process, the die cavity is filled with metallic powder so, the porosity is high and the density is low. At the moment in which the metallic powder starts to be compacted the void spaces start being less, the porosity starts decreasing and the density increasing until the porous specimen or green body with the shape of the die cavity is obtained. In figure 9.2, it is possible to see the initial dimensions of the specimen (the contour line in black) and the dimensions in the final of the compaction stage (the green body with mesh applied). As it is possible see in the legend, the displacement is around 9 mm, so the specimen was compacted to half of the initial heigh.

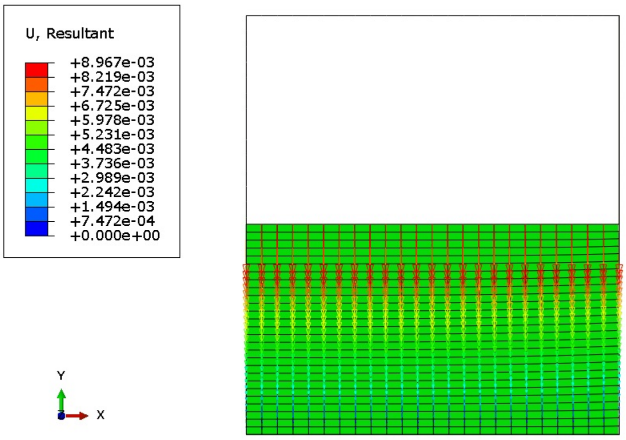

Figure 9.2: The compaction stage, at the beginning and at the end of the process.

The relative density (RD) gradients at the end of the compaction stage, i.e., after the loose powder is compacted and the tools released, are shown at figure 9.4. For comparing, it is shown in figure 9.3 the plastic volumetric strain ($\varepsilon_{\mathrm{v}}^{\mathrm{pl}}$) at the end of compaction stage. The two parameters are intimately connected by relation 2.13. Therefore, the two behaviours are shown in figure 9.3 and 9.4.

As it is possible to see in figure 9.4, the relative density assumes values around 0.6. In fact, looking at figure 9.4, it is noticed that the values of relative density do not change significantly. The relative density presents its higher value in the superior right vortex of the specimen. This value is high in that zone because it is, supposedly, the local where the specimen is in contact with the die wall and, at the same time, with the upper punch vortex that practises the compaction movement. This, associated with the friction between the specimen and the die wall, reflects the higher relative density value in that zone. On the other hand, the lowest relative density value is located in the right bottom vortex of the specimen, where it is in contact with the lower punch vortex and the die wall. Due to the lower punch function of holding the specimen while the upper punch compacts the specimen, and to the friction between the die wall and the specimen, lower values of relative density are obtained at the bottom of the specimen.

For a better analysis of the density, a short study about the density behaviour in the elements was made, which is shown in figure 9.1. This study is addressed in figures 9.5,

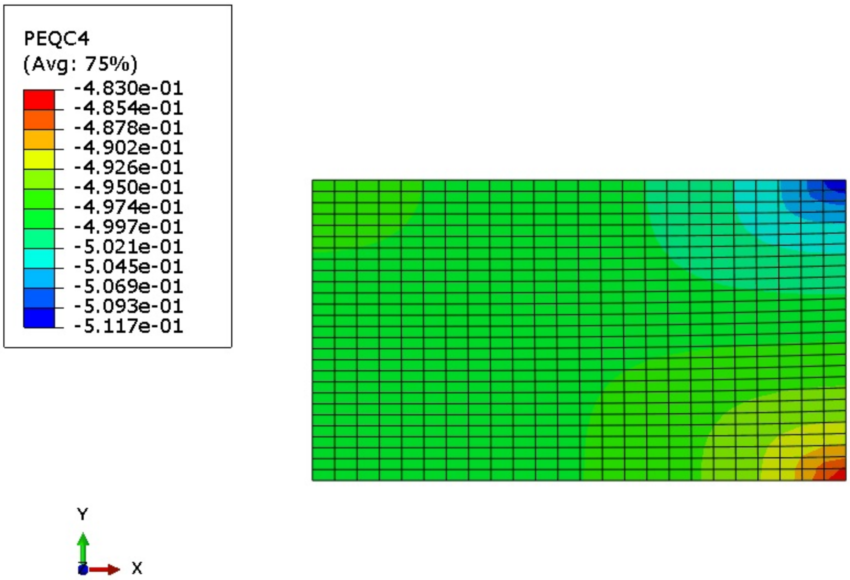

Figure 9.3: Plastic volumetric strain (ε_v^{pl}) at the end of compaction stage.

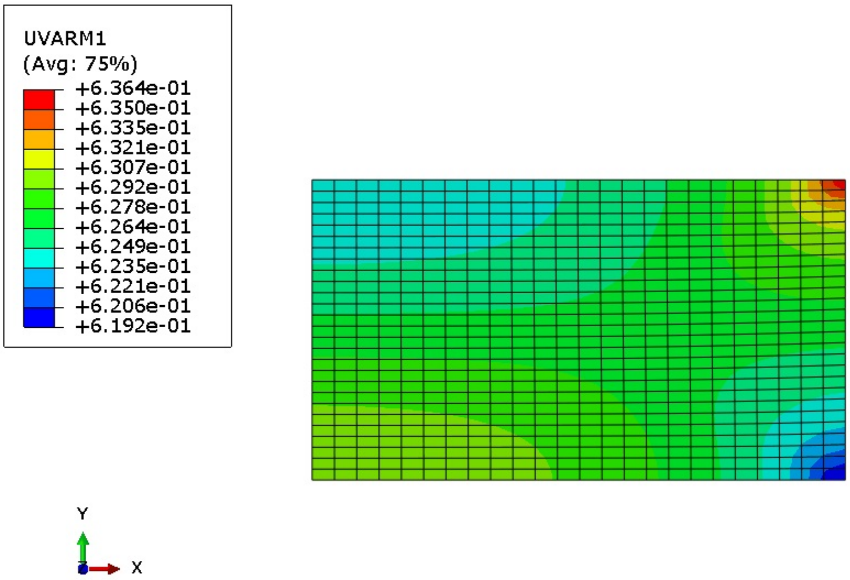

Figure 9.4: Density gradients after compaction stage.

9.6, 9.7 and 9.8.

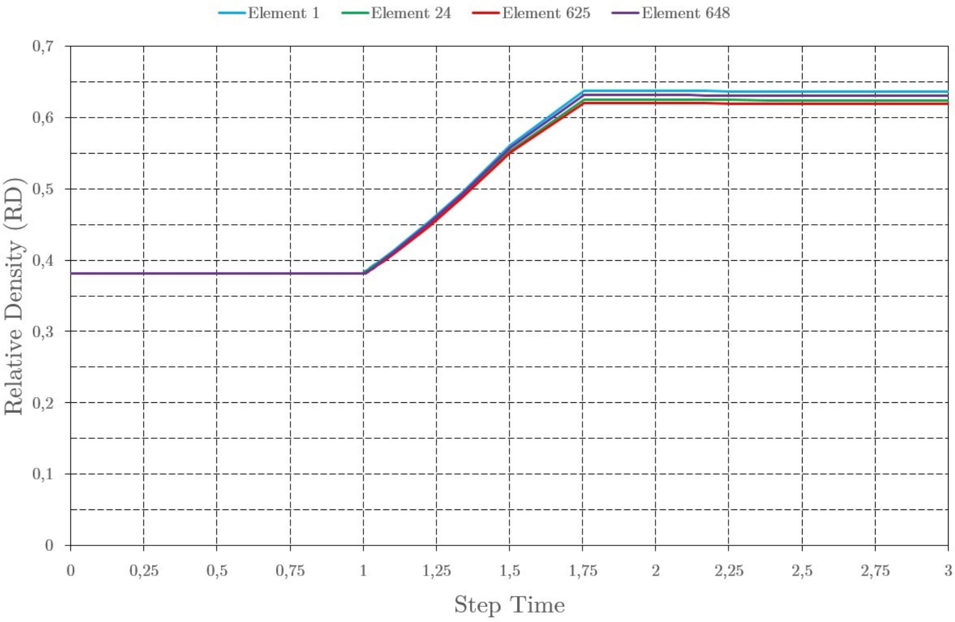

Figure 9.5: Evolution of relative density during the compaction stage.

Looking at figure 9.5, it was noticed that while the plastic volumetric strain did not start, the initial relative density stayed constant. The first step, is a step for establishing contact of the tools with the specimen and for applying the boundary conditions, which explains why the relative density did not change until the step time of 1.

In the second step time, the upper punch started its movement for compacting the loose powder, therefore, the plastic volumetric strain started. With the beginning of the volumetric plastic strain, the relative density started to increase. After the compaction process finished, i.e., after the specimen was converted to half of its original height, the relative density turned to a constant value during the release of the tools. This can be seen in figure 9.5 in the step time from 2 to 3.

In figure 9.6, it is possible to verify that during the compaction process of loose powder, the density is increasing at the same time that the axial stress increases. Therefore, high densities occur when axial stress assumes high values. Note that for obtaining a compaction of 50% of the initial height, an axial stress between 160 MPa and 170 MPa is necessary. This happens in the compaction loading process. In the unloading process the specimen is released from the tools and the axial stress turns to zero.

In figure 9.7, it is verified that in the loading phase the maximum value of axial pressure is registered when the volumetric plastic strain is maximum. This is coherent with what is seen in figure 9.6, since relative density and plastic volumetric strain are intimately related. So, figures 9.6 and 9.7 show the same behaviour during the compaction stage.

In figure 9.8, the stress relatively to step time is analysed. As it is possible to see in figure 9.8, the stress increases exponentially during the compaction stage, i.e, the stress increases during the loading process. The stress reaches its maximum at the end of

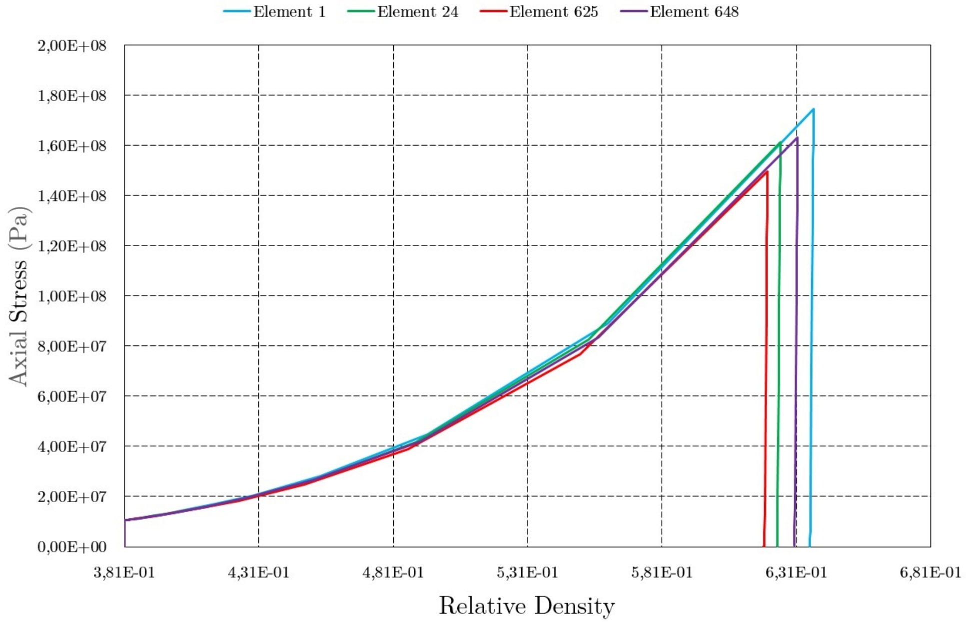

Figure 9.6: Behaviour of density with axial stress.

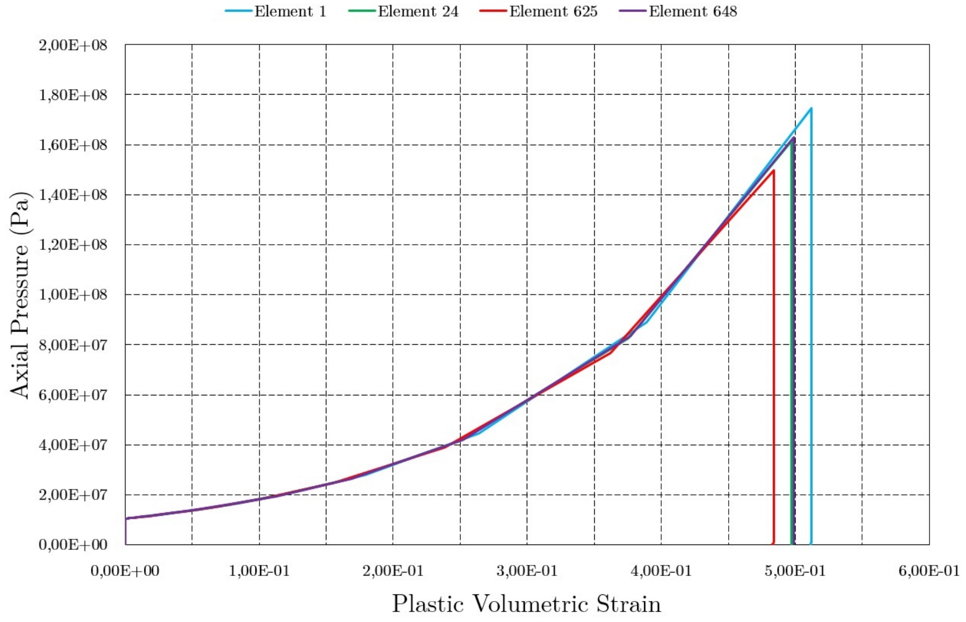

Figure 9.7: Densification behaviour.

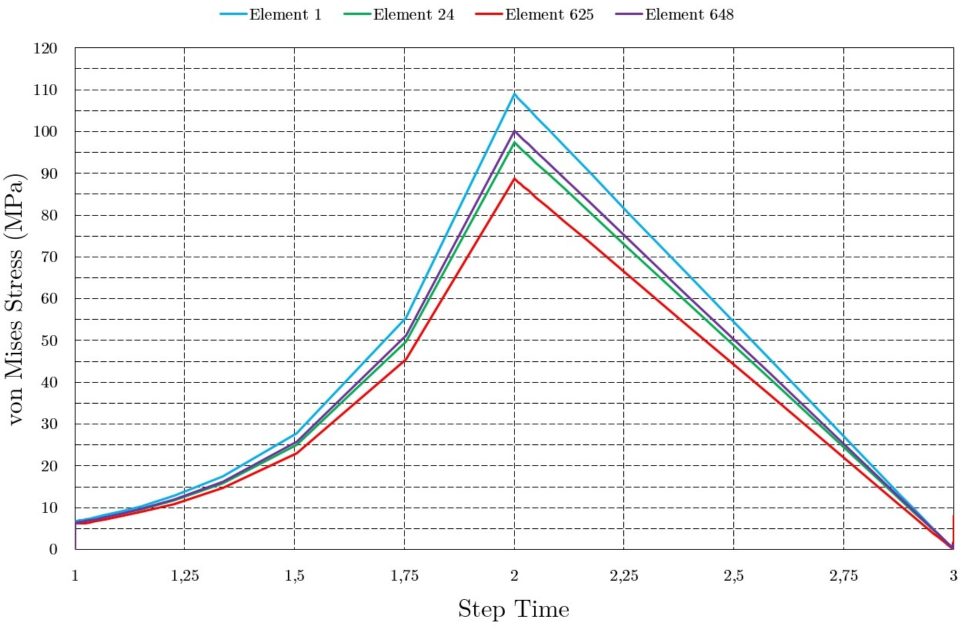

Figure 9.8: von Mises stress during compaction stage.

loading stress. After that, the unloading process starts and the stress decreases linearly remaining, at the end, the residual stress.

9.3 Sintering Stage Analysis

In this section, the behaviour of the specimen during the sintering is analysed. Here, the specimen ended the compaction stage and is at the beginning of the sintering. Therefore, the variables that influence directly the sintering are analysed. For that, the sintering cycle is considered to be the reference cycle for this study. Looking at figure 9.1, the analysis will be made in four elements of the specimen, the same elements that were analysed in the compaction model.

It starts for analysing the contour plot of the density gradients. Thus, in figure 9.9, the density gradients at the beginning of the sintering process simulation (the same gradients as in the end of the compaction stage) and the density gradients at the end of the sintering process simulation (after occurring coarsening and densification) are presented.

Next, the sintering stress is presented (figure 9.10) which affects the specimen during the sintering. Here, is presented the sintering stress that affects the specimen at the transition temperature in the heating ramp and at the transition temperature in the cooling ramp.

The stresses at the beginning of the sintering process are the residual stresses coming from the compaction stage. In the sintering process simulation, the residual stresses are mainly affected by thermal effects. In figure 9.11 it is possible to see the stresses at the beginning of the compaction stage and the residual stress at the end of the sintering stress simulation.

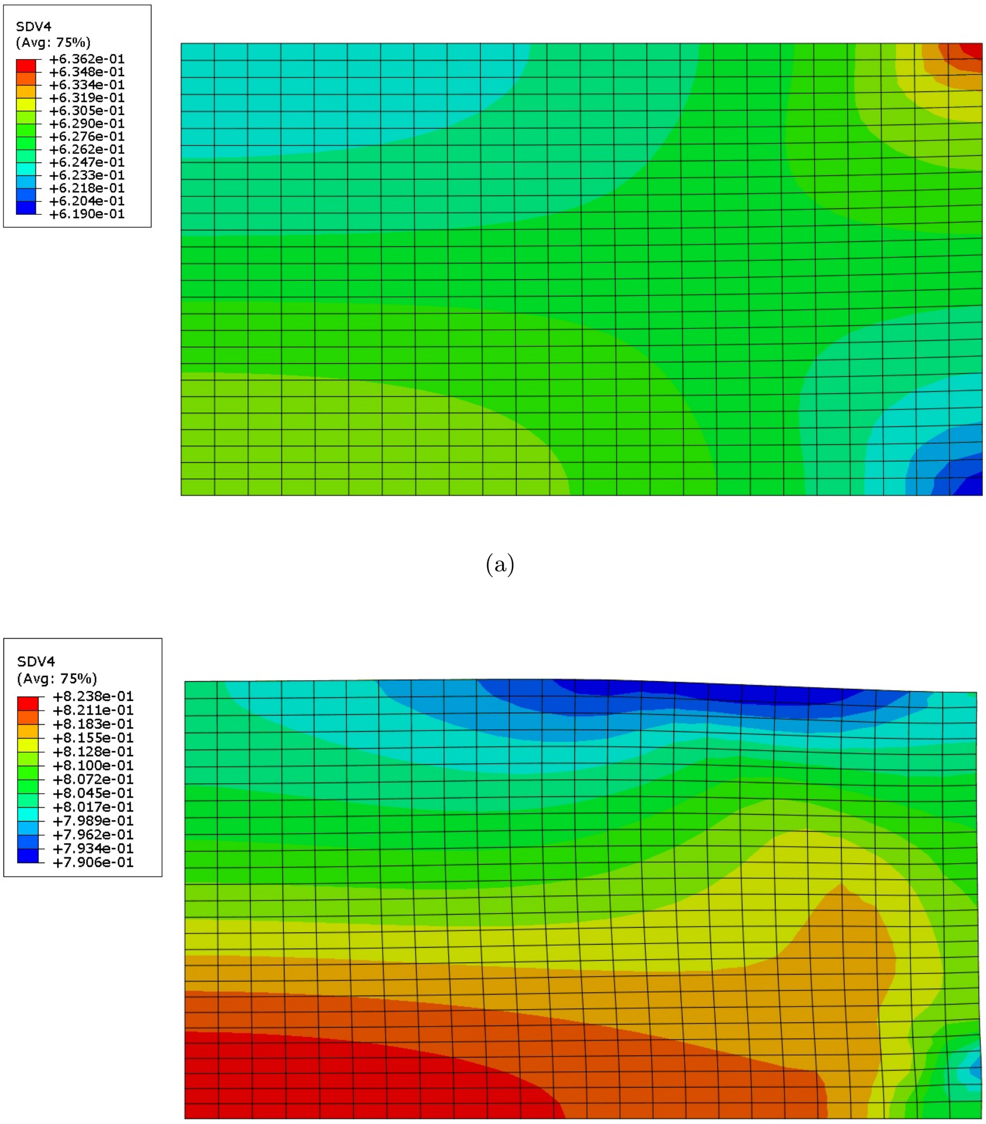

(a)

(b)

Figure 9.9: Evolution of density gradients during sintering (a) Density gradients at the beginning of the sintering cycle (b) Density gradients at the end of sintering cycle.

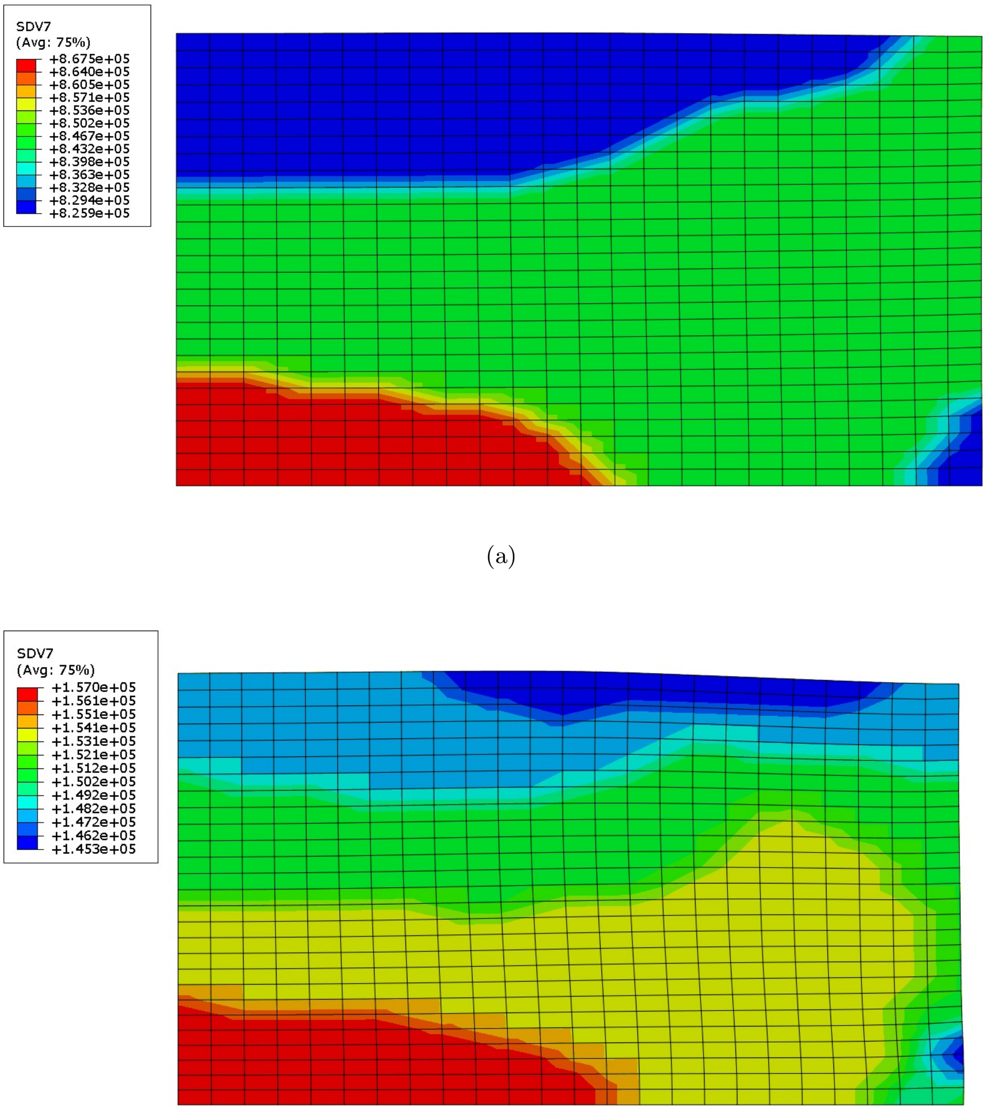

(a)

(b)

Figure 9.10: Sintering stress behaviour, (a) at the transition temperature during the heating ramp (b) at the transition temperature during cooling ramp.

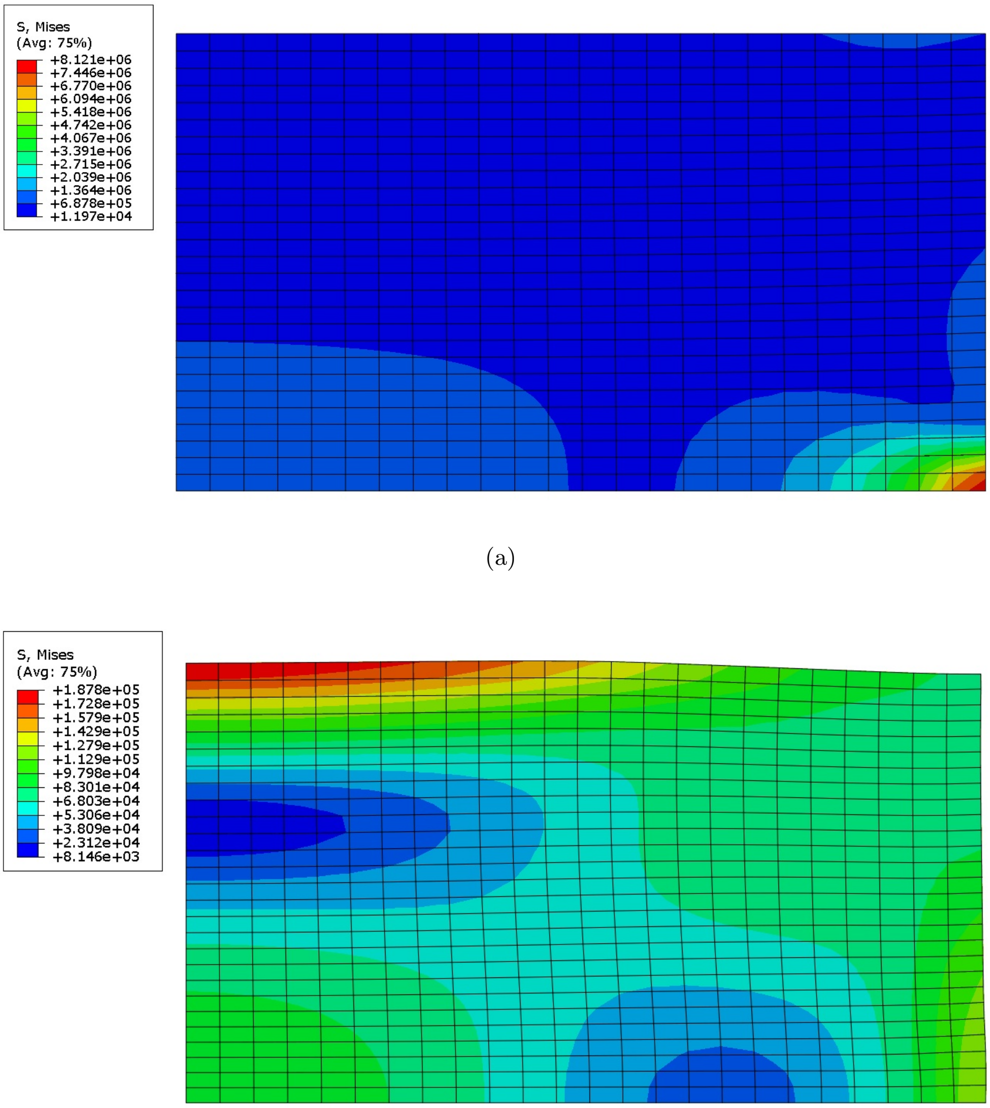

(a)

(b)

Figure 9.11: von Mises stresses, (a) at the beginning of the sintering stage (b) at end of the sintering cycle.

The specimen temperature field at the beginning of the sintering process is at room temperature 20 °C (293 K). As the temperature increases, the compact temperature field stops being an homogeneous field and starts to be an heterogeneous field as figure 9.12 shows. Naturally, the edges that are directly in contact with the sintering atmosphere heat faster than the internal compact (figure 9.12 (a)). On the other hand, during the cooling ramp the internal compact tends to have a slower cooling rate than the edges in direct contact with the sintering atmosphere (figure 9.12 (b)).

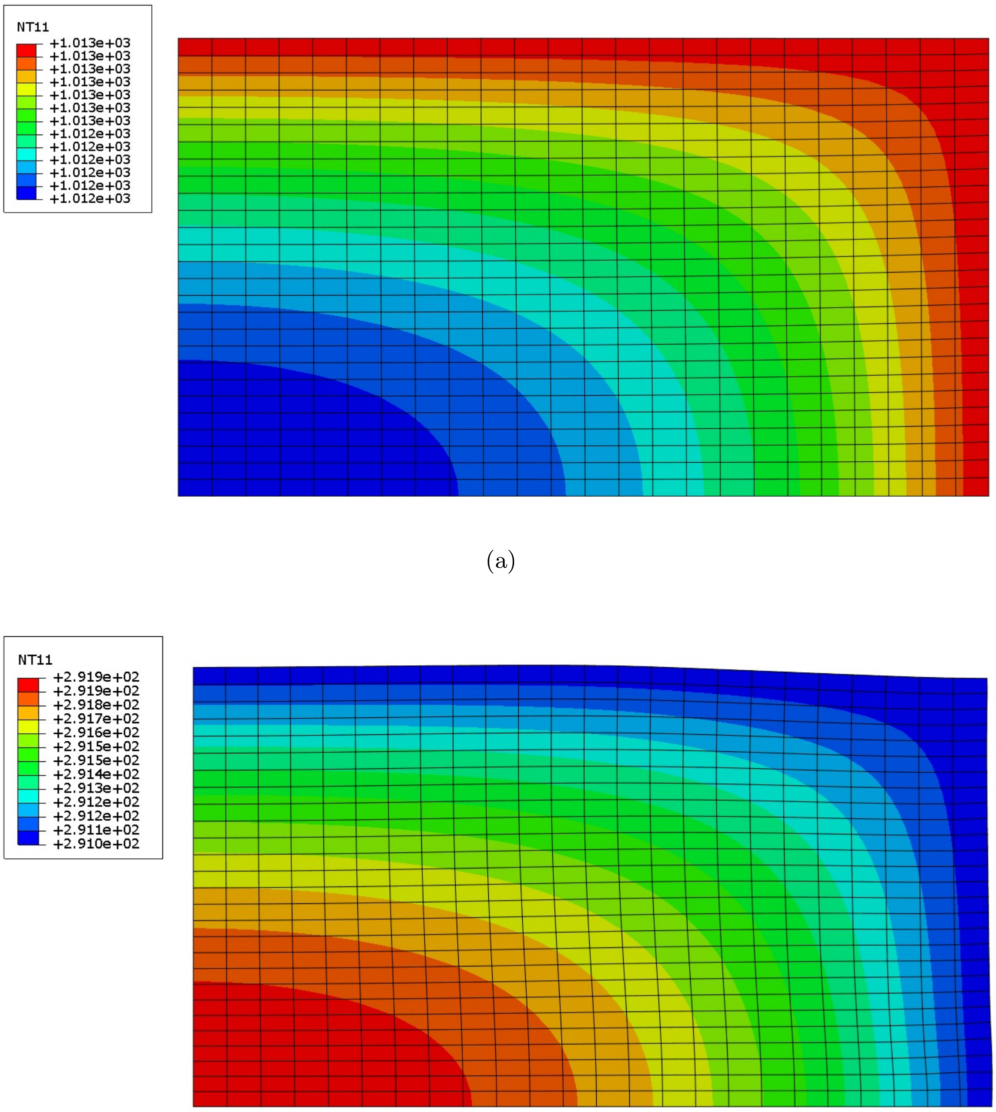

(a)

(b)

Figure 9.12: Tempeature field: (a) during the heating ramp (b) during the cooling ramp.

The grain size is one of the properties that directly affects the compact during sintering. It is necessary to control the grain growth, for minimizing its influence in the densification of the specimen. At the beginning of the sintering stage, the compact grain size was considered to be homogeneous (4.36 μm). At the heating ramp, until the transition temperature is not reached, the grain growth did not affect the sintering. After the transition temperature is reached, the grain starts growing. In the end of the sintering stage, the grain growth is given by the contour plot presented in figure 9.13. Observing figure 9.13 it can be concluded that grain size is bigger in zones that are closer to the sintering atmosphere. In the interior zones of the specimen, the grain size is smaller. However, general, at the end of sintering, the specimen has an homogeneous grain size value, around ($39\mu m$).

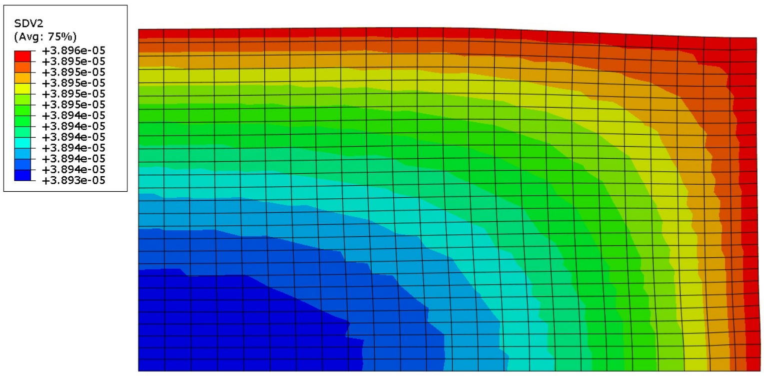

Figure 9.13: Grain size at the end of the sintering stage.

Focus now on the study made in four different elements of the same mesh. It was adopted the four critical elements considered in the compaction analysis (figure 9.1). In this phase, the axial shrinkage study (figure 9.14), the relative density behaviour during the sintering stage (figure 9.15), and the stress studies, the sintering stress (figure 9.16) and von Mises stresses are presented (figure 9.17).

In figure 9.14, independently on the element in analysis, the general shrinkage behaviour starts with a volume expansion (when shrinkage takes negative values it means an expansion takes place, when shrinkage takes positive values occurs contraction). This happens because the specimen has initially accumulated the residual stresses from the compaction process, and also it is also affected by the initially heating ramp, where the thermal expansion effects are more pronounced. Therefore, there is a smooth expansion at the beginning of the sintering cycle. This smooth expansion is more noticeable in elements 1 and 24 and it remains to temperatures around 918 °C. At 918 °C, which is called the transition temperature, is the turning point of expansion to contraction. It is more noticeable in elements 1 and 24, where at 918 °C the expansion stopped and contraction started. In 625 and 648, the contraction started even before the transition point. However, after the transition point, it was noted that the expansion was predominant in the four elements. The expansion increases dramatically after the transition temperature until 1200 °C. This increase is due to the increase in sintering stress, as shown in figure 9.16. After 1200 °C, the sintering stress starts to decrease because the activation energy for grain growth shifts to a lower level and the grain growth rate starts to increase.

Figure 9.15 shows the predicted relative density change during sintering. It is concluded that relative density did not change in the initial heating ramp and in the final cooling ramp. These are zones dominated by thermal expansion/contraction. The rel-

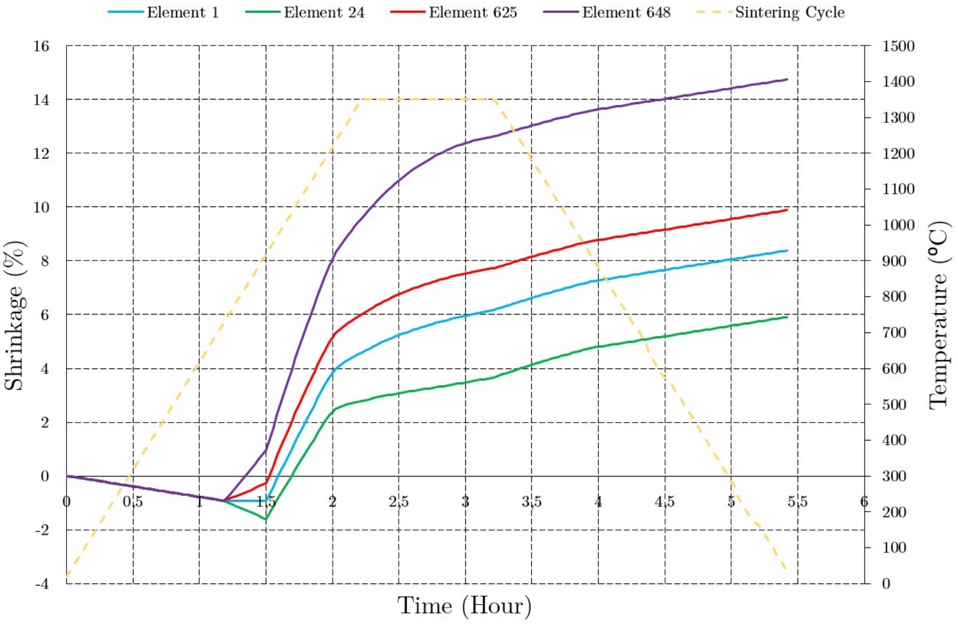

Figure 9.14: Axial shrinkage curves in function of time.

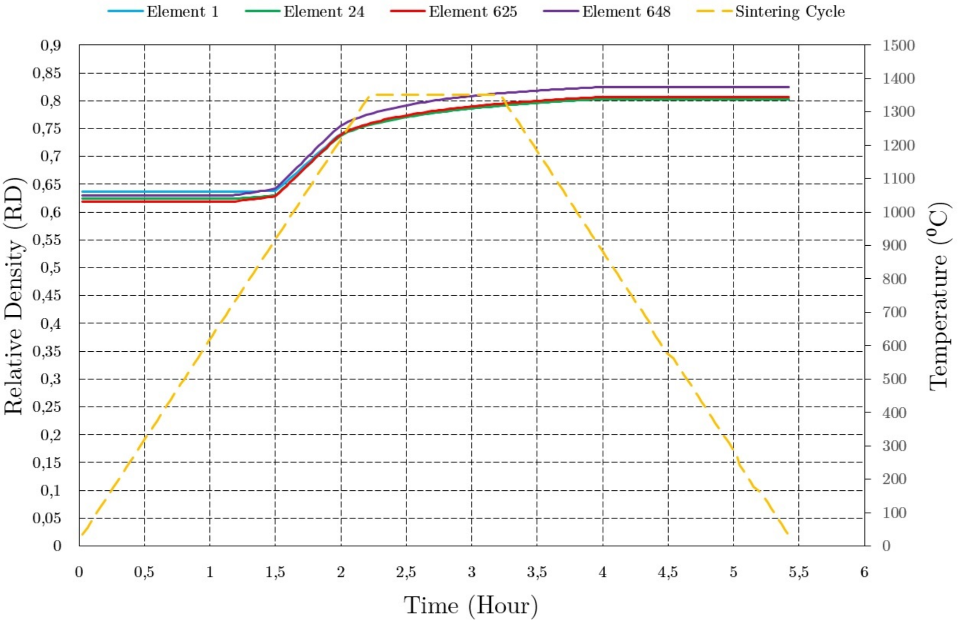

Figure 9.15: Relative density curves predicted by FEM model for Stainless Steel 316L powder compacts.

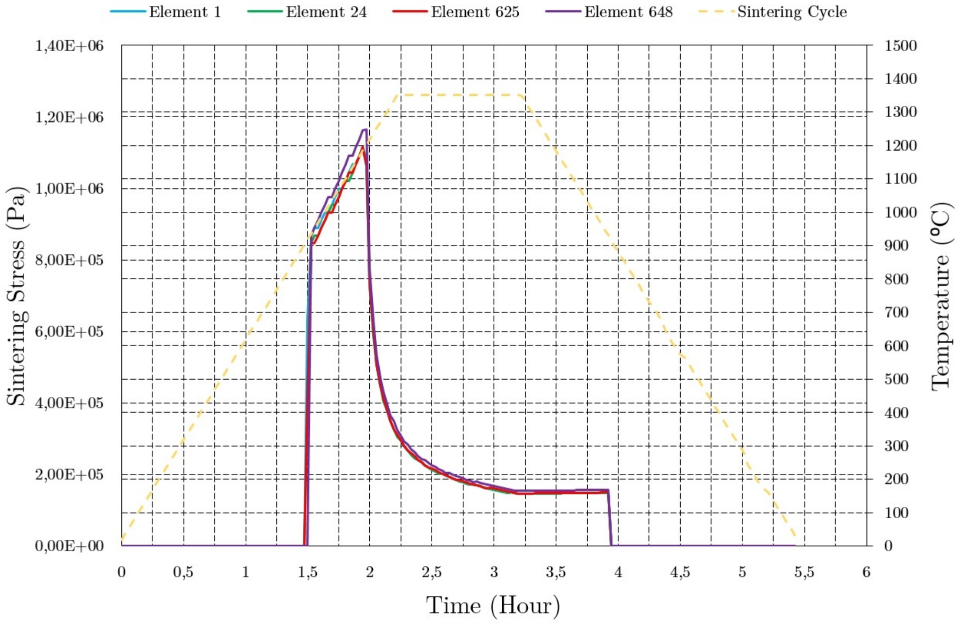

Figure 9.16: Sintering stress changes during sintering.

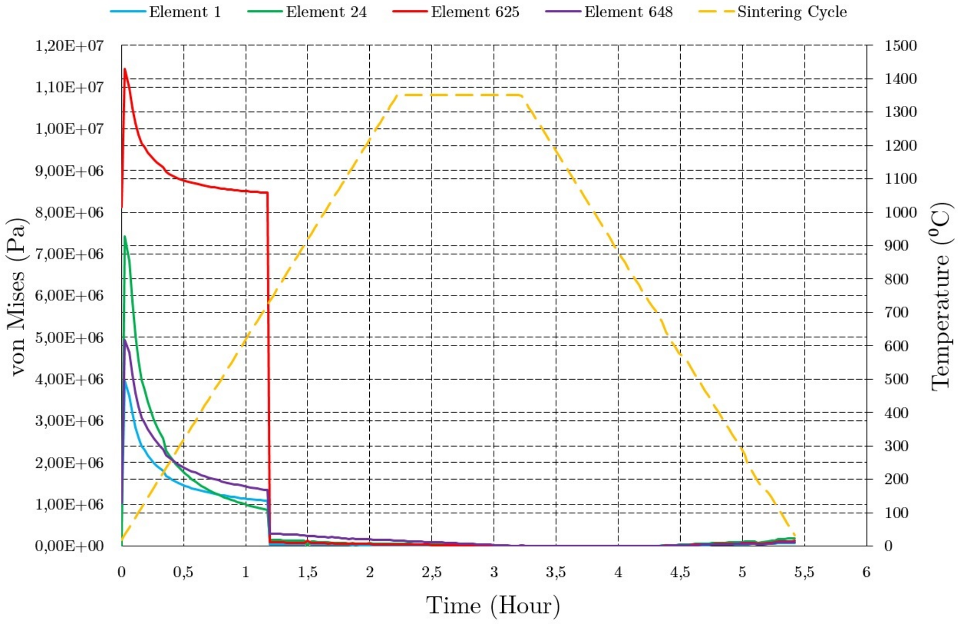

Figure 9.17: von Mises stress during the sintering process.

ative density started to increase when the swelling strain started to be relevant in the sintering cycle. The relative density increased when the transition temperature was reached in the heating ramp final phase, it still increased during the holding time, and when the cooling ramp started the relative density started to smoothly keeping constant, and after the transition temperature at the cooling ramp it simply did not increase anymore. The final relative density reached around 0.8. The element 648 is where the final density reached the highest value, around 0.84.

Looking into figure 9.16, it is shown that sintering stress had the same behaviour independently of the element. The element 648 is the only which has taken higher values. The sintering stress only affect the sintering process when the transition temperature is reached. After 918 °C and until 1200 °C the sintering stress increases. The sintering stress increases due to the grain size maintaining constant in this interval. At 1200 °C, the sintering stress starts decreasing dramatically because the grains start to grow. From the material model implemented, it is known that the sintering stress is proportional to the reciprocal grain size. In the cooling ramp, the sintering stress is only affected by the relative density slowly increasing until the temperature drops down to the transition temperature and sintering stress stops influencing the sintering stage.

In figure 9.17, it is demonstrated how the von Mises stress behaves along the sintering stage. At the beginning of the sintering cycle, the von Mises stress assumes the values from the residual stress of the compaction stage. The von Mises stress reaches a maximum value at the beginning and starts smoothly decreasing while the temperature starts increasing. At this point the sintering stage is dominated by the thermal expansion. Closer to the transition temperature, the sintering stress starts to dominate the stresses in the sintering stage, and the von Mises stresses dramatically decrease. After the transition temperature and during the holding time and the cooling ramp where the sintering stresses dominate, the von Mises stresses assume values near 0. In the end of the sintering cycle, the sintering stress desappears and residual values for the von Mises stress appear. At the end, the von Mises stresses assumes a very low value.

9.4 Sensitivity Analysis

In this section, it is reproduced a sensitivity analysis, which objective is to study the mesh influence in the obtained results. Therefore, it was a study in the compaction and sintering stages was made where, at each process, three different meshes were applied: a coarse mesh; an intermediate mesh and a refined mesh. A coarse mesh with 132 elements; the intermediate mesh from the mesh used in the case study was adopted and it was described in subsection 8.2.1. The intermediate mesh is defined with 648 elements. Finally, a refined mesh with 957 elements was applied. The elements' difference between the intermediate and refined meshes is not so accented as between the coarse and intermediate meshes. Therefore, the results' difference between the intermediate and refined meshes may not be so significant. For the coarse mesh, the elements analysed is represented in figure 9.9 (a). The intermediate mesh, like said before, was adopted from the case study, therefore, the elements analysed are represented in figure 9.1 from section 9.2. Finally, in the refined mesh, the analysed element are represented in figure 9.18 (b). Firstly, the mesh influence in the compaction stage is analysed, after the same analysis is done but for the sintering stage.

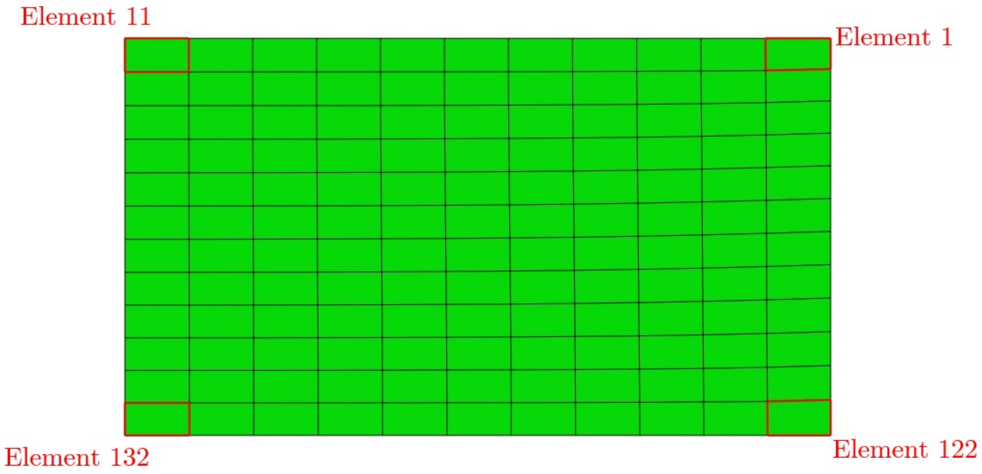

(a) Coarse mesh with the four elements referenced.

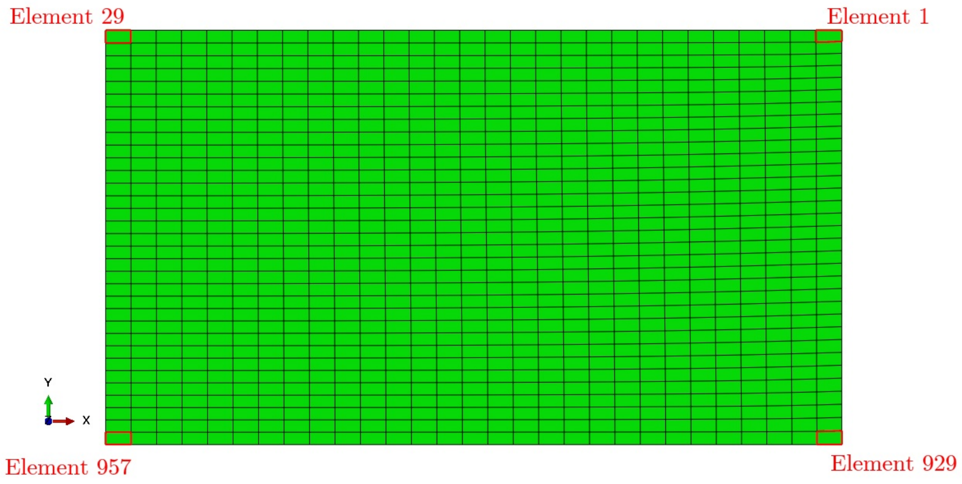

(b) Refined mesh with the four elements referenced.

Figure 9.18: The different meshes applied in the sensitivity analysis.

9.4.1 Compaction Sensitivity Analysis

In this sensitivity analysis some parameters that were analysed in the compaction stage are presented (section 9.2) but now influenced by different meshes. Therefore, a study was made, where four groups of elements were analysed: element 1; elements 11, 24 and 29; elements 122, 625 and 929; elements 132, 648 and 957 from figures 9.18 (a); 9.4 and 9.18 (b), respectively. This elements are analysed in the study of the mesh influence relatively to the punch force for compacting the loose powder, the von Mises stress and axial stress in function of relative density. Firstly, a study is presented about the force necessary to compress the loose powder for half of initial height, like was presented in figure 8.5. In the punch force study, it was analysed how the reaction force behaved in each node of the upper edge. The analysis is presented in figure 9.19.

Following, the behaviour of the von Mises stress along the relative time is presented in figures 9.20 and 9.21. Figure 9.20 presents the two upper edge elements from figure 9.18, and figure 9.21 presents the study of the two bottom elements, also from figure 9.18. This architecture of results' presentation is maintained for the study of the next parameters that are presented in this section. The number of graphics presented in this chapter is very exhaustive due to a coherency question of maintaining the decision of analysing the four critical elements like was made in sections 9.2 and 9.3. Therefore, in each parameter analysed, there are four graphics corresponding to each of the four elements for the three different meshes.

In figures 9.22 and 9.23, the evolution of the axial stress in function of the relative density is presented. Figure 9.22 presents the two elements of the upper edge and figure 9.23 presents the two elements of the bottom edge.

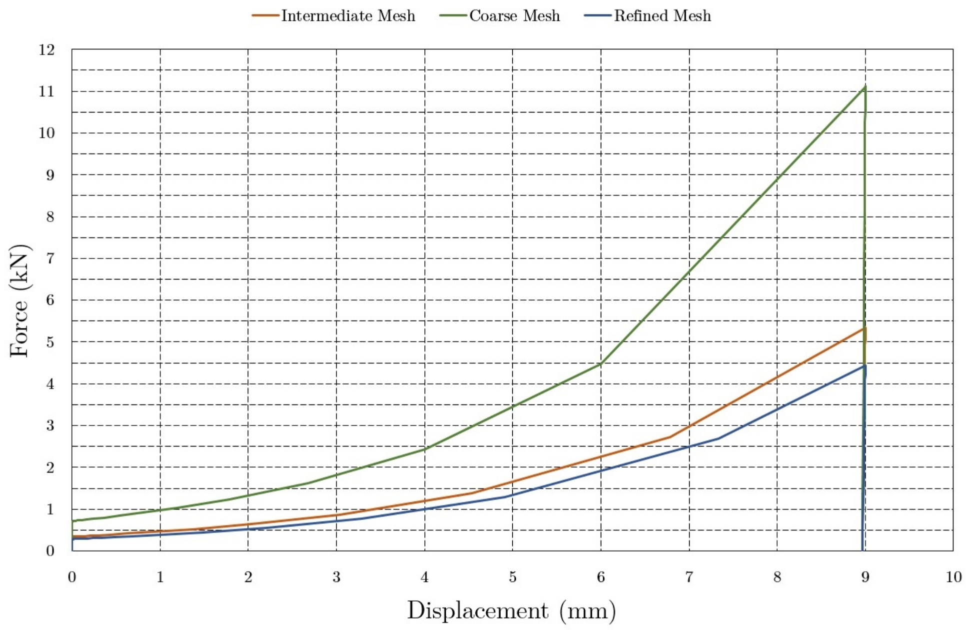

Figure 9.19: Punch force analysis in fuction of mesh types.

In figure 9.19 it is possible to observe the punch force evolution as long as the loose powder is pressed. Once again, it is necessary to explain that, for simplifying

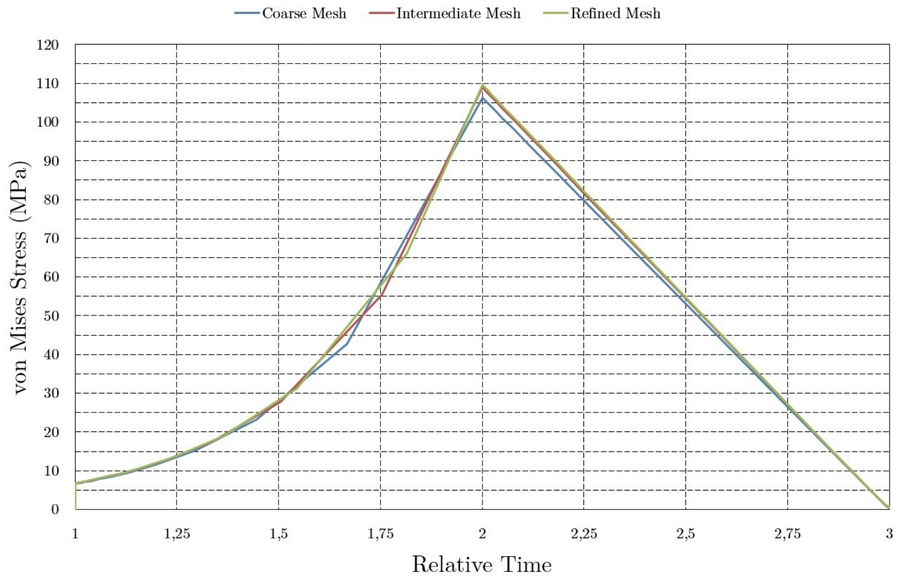

(a) von Mises stress analysis for element 1 with different refined meshes.

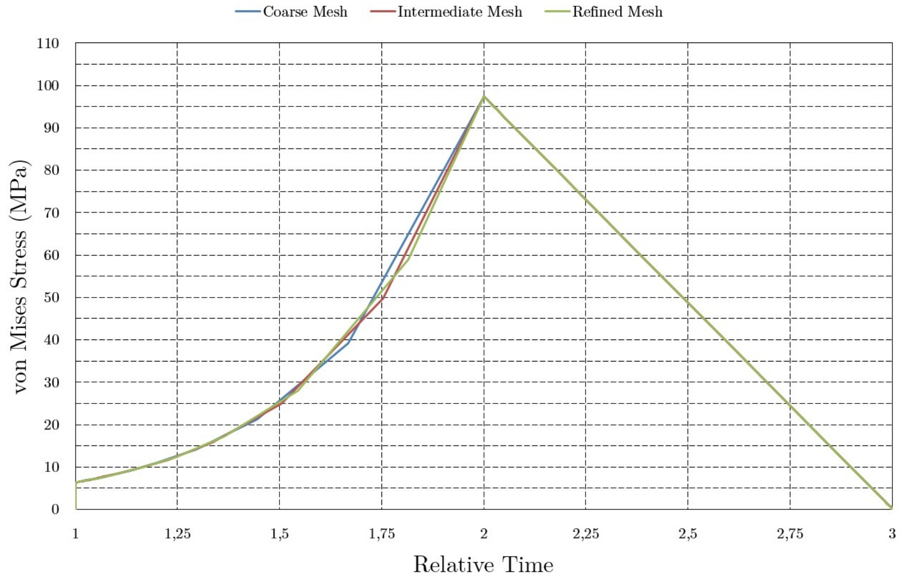

(b) von Mises stress analysis for elements 11; 24 and 29 for different refined meshes.

Figure 9.20: von Mises stress for the two first elements.

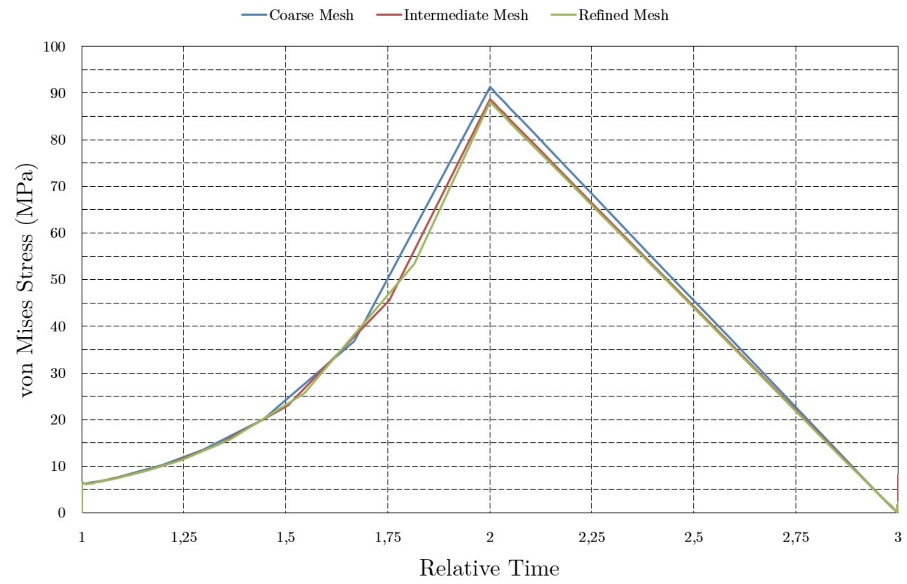

(a) von Mises stress analysis for elements 122, 625 and 929 with different refined meshes.

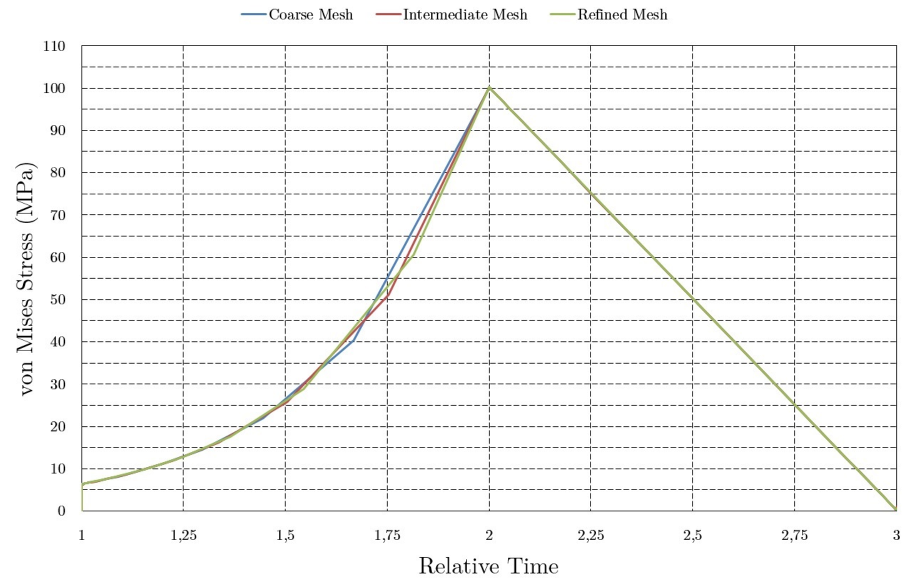

(b) von Mises stress analysis for elements 132; 648 and 957 for different refined meshes.

Figure 9.21: von Mises stress for the two last elements.

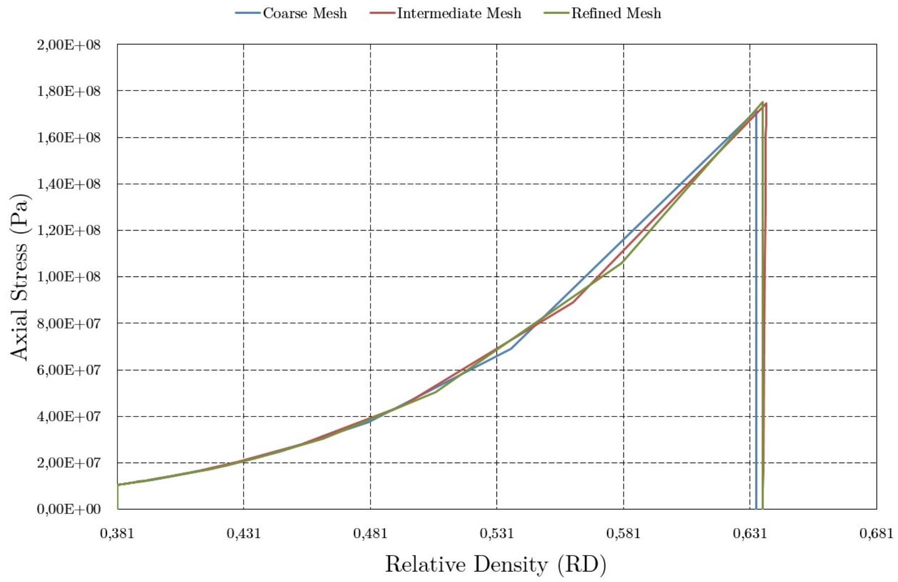

(a) Axial stress evolution along the relative density increasing in element 1 for different mesh types.

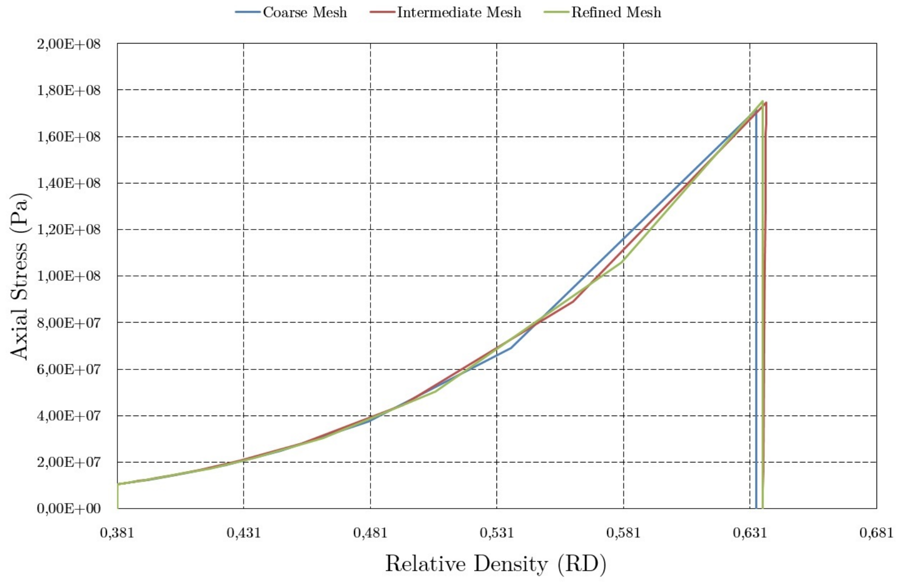

(b) Axial stress evolution along the relative density increasing in elements 11; 24 and 29 for different mesh types.

Figure 9.22: Axial stress evolution along the relative density for the elements in the upper edge.

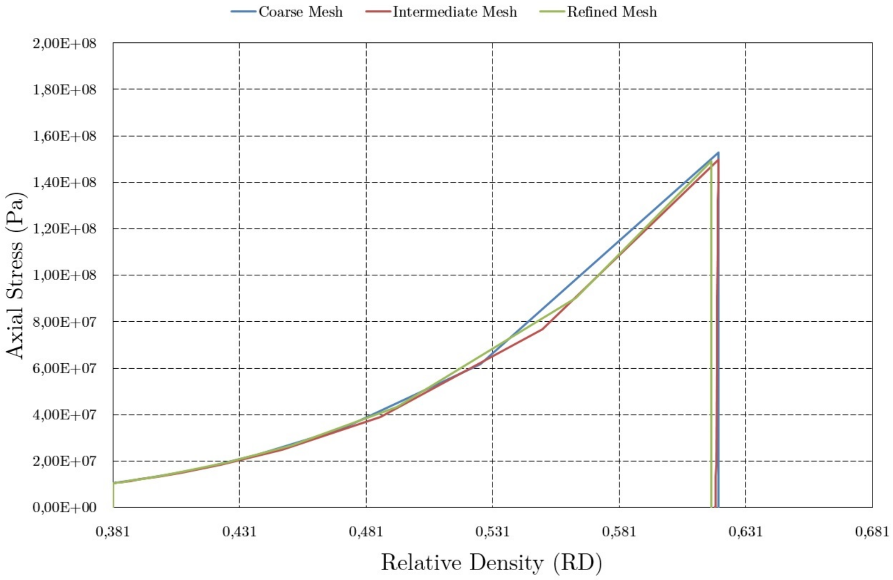

(a) Axial stress evolution along the relative density increasing in elements 122; 625 and 929 for different mesh types.

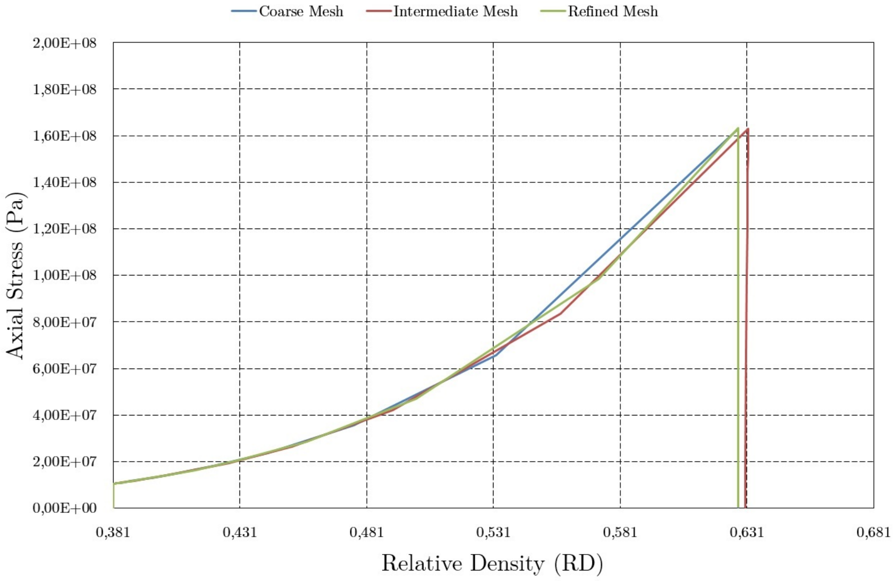

(b) Axial stress evolution along the relative density increasing in elements 132; 648 and 957 for different mesh types.

Figure 9.23: Axial stress evolution along the relative density for the elements in the bottom edge.

the problem, the upper punch, which is responsible to compress the loose powder, was substituted for a displacement condition in the upper surface of the specimen in the finite element program. Therefore, it explains the fact that when a displacement of 9 mm is reached, an abrupt decrease from a maximum force to 0 happens because when it reaches 9 mm the displacement conduction is inactivated. However, analysing figure 9.19 it is possible to conclude that the force necessary for pressing the powder increases along the displacement, and the maximum force is reached at 9 mm, when the compaction ends. This is the general punch force behaviour independently of the mesh type.

Relatively to the mesh influence, it is noticed that with a refined mesh the maximum force necessary to compact the disk to half of the initial heigh is approximately 4.5 kN, or, in other terms, it is necessary approximately 450 kgf to compress the loose powder. In the intermediate mesh, the maximum force increases to approximately 5.5 kN, which is approximately 550 kgf. The major difference is in the coarse mesh, with few elements, a punch force much higher than in the intermediate and refined meshes is recorder. In the coarse mesh it is registered around 11 kN for compacting the powder, so, it takes about 1.1 ton to compress the powder. For this analysis, it is concluded that when the mesh is more refined, more accurate is the value relatively to the force imposed for compacting the powder. Therefore, for the mesh with most accuracy, the lowest is the force needed for compacting the loose powder.

Focus now in the von Mises stress along the compaction process evolution. The curves' behaviour, in figures 9.20 and 9.21, was already discussed in section 9.2. Here, the objective is to understand if the mesh types have different behaviours. As can be seen in figure 9.20 (a) for the element 1, it is evident that the three different meshes: the coarse mesh; the intermediate mesh and the refined mesh; do not have a big difference between them. The three curves have the same behaviour along the compaction process, and this conclusion is a constant for figures 9.20 (a) and (b) and 9.21 (a) and (b). In the element 1 (figure 9.20 (a)) the intermediate and refined meshes reach the von Mises stress maximum at around the same value, 109 MPa for the intermediate mesh, and 110 MPa for the refined mesh. The coarse mesh takes a lower value, around 106 MPa. It is noticed that the intermediate and refined meshes assumes higher values relatively to the coarse mesh at the relative time from 2 to 3. In the elements 11, 24 and 29 (figure 9.20 (b)) the three different meshes had the same behaviour, they reached their maximum at around 97 MPa. During the relative time from 1 to 2, there are some differences but they are insignificant, because it is during the compression process period. In the elements 122, 625 and 929 (figure 9.21 (a)) it is possible to see that the coarse mesh assumes higher values relatively to the intermediate and refined meshes. Along the compaction process, the coarse mesh has a von Mises maximum of 91 MPa higher than the intermediate and refined meshes, which have 88 MPa. In the ejection period from 2 to 3 the coarse mesh still takes higher values relatively to the intermediate and refined meshes. For the elements 132, 648 and 957, the same behaviour as in figure 9.20 (b) can be seen. There is no significant difference between the three meshes. All the three meshes assume the von Mises maximum at 100 MPa and the ejection step from 2 to 3 has the same behaviour. In conclusion, it is interesting that the elements analysed close to the symmetric line have the same behaviour, in other words, do not have any change with the different meshes. On the other hand, the elements close to the die surface are where the refined or coarse meshes have a detached behaviour in relation to the other mesh. The von Mises stress is higher in the element 1 and elements 132, 648 and 957, and the von Mises stress is lower at elements 11, 24 and 29, and elements 122, 625 and 929.

Another study made for verifying the mesh sensitivity at the compaction stage was the relation between the increasing axial stress versus the relative density. Figure 9.22 shows the two elements' behaviour in the upper surface and in figure 9.23 the two elements' behaviour in the bottom surface is shown. In the study of element 1, (figure 9.22 (a)) it is shown that the three different meshes have a similar behaviour. In the loading phase, the axial stress increases as well as the relative density. In the unloading phase, the displacement of the upper punch was deactivated and the axial stress started to decrease down to a residual value. The coarse mesh had its axial stress maximum at 172 MPa for a relative density of 0.634. The intermediate and the refined meshes have their maximum axial stress value at 175 MPa for a relative density of 0.636. Therefore, the mesh influence is not significant for this type of study. It is concluded that in the element 1, the coarse mesh registered the lowest value but it was very close to the values registered in the intermediate and refined meshes. The elements 11, 24 and 29 (figure 9.22 (b)) have the same behaviour of the figure 9.22 (a) therefore, the conclusion presented previously is maintained for this study of mesh influence. In the elements 122, 625 and 929 (figure 9.23 (a)) it is shown that the axial stress assumes lower values than in figure 9.23. However, it is perfectly normal due to being analysed the elements are the ones in the bottom of the sample. It is noticed that the coarse mesh assumes higher values in the loading phase but it is the refined mesh that has the lowest relative density value in the end. The coarse mesh has an axial stress maximum of 153 MPa for a relative density of 0.620. The intermediate mesh has an axial stress maximum of 150 MPa for a relative density of 0.620 and the refined mesh has an axial stress maximum of 148 MPa for a relative density of 0.617. Once again, there are some differences but nothing very significant. The three different meshes still have a similar behaviour, and in figure 9.23 (a) it is the refined mesh that assumes the lowest value for the axial stress and corresponding relative density. In the elements 132, 648 and 957 the behaviour is as shown in figure 9.22 (a). During the loading, the coarse mesh presents the highest values. For the coarse mesh, it presents the axial stress maximum at 163 MPa for a relative density of 0.626. The intermediate mesh and the refined mesh also present the axial stress maximum at 163 MPa but for the intermediate mesh the relative density is around 0.631 and in the refined mesh it is around 0.626. Thus, the discrepancy, here, is in the intermediate mesh that assumes the same value of axial stress maximum but for a relatively high density in relation to the coarse and refined meshes.

In the compaction stage were these parameters presented previously, for studying the influence of mesh type in the behaviour of von Mises stress, the axial stress with relative density and the punch force. It was verified that in the punch force the difference in mesh type influences the values. However, in the von Mises stress and in the axial stress versus relative density the difference was minimum.

9.4.2 Sintering Sensitivity Analysis

In this subsection it is presented the relevant parameters in the sintering stage for a sensitivity analysis relatively to the mesh type. All the assumptions presented in sections 9.4 and 9.4.1, and the form in which the results are presented remains the same in this subsection.

Firstly, it is presented the axial shrinkage evolution along the time. Here, like was made in the case study, the results are presented always in relation to the sintering cycle. In figure 9.24 (a) and (b) the axial shrinkage evolution for the two elements of the upper surface is shown. On the other hand in figure 9.25 (a) and (b), the axial shrinkage evolution for the two elements of the bottom surface is shown. Another study is performed to understand the relative density along the sintering cycle with different meshes and it is shown in figure 9.26 (a) and (b) and figure 9.27 (a) and (b). Finally, in this sensitivity study, an analysis with the three different meshes on the sintering stress is made. The results with different mesh types are presented in figure 9.28 and in figure 9.29.

The description of the typical axial shrinkage curve behaviour was made in section 9.3, therefore it is not the main objective to explain the curve behaviour but rather explain whether the meshes have a major or a minor influence in the axial shrinkage. Starting by analysing the figure 9.24 (a), where it is shown that the three meshes curves demonstrated an initial expansion in the compact until the transition temperature was reached. After that, the three curves start the contraction behaviour, and at the end of the sintering cycle the coarse mesh has the highest axial shrinkage value corresponding to 8.49%. The intermediate mesh reaches an axial shrinkage value of 8.38% and the refined mesh has an axial shrinkage of 8.19%. Thus, the axial shrinkage, for a coarse mesh, takes a higher value than for a refined mesh. The difference is not very large but in the element 1, the refined mesh gives the lowest axial shrinkage value which should be more properly. In elements 11; 24 and 29, the three different meshes have the same behaviour as in figure 9.24 (a). Starting with an expansion until the transition temperature and beginning the contraction after the transition temperature. In figure 9.24 (b), the refined mesh assumes an axial shrinkage value around 7.0%. The intermediate mesh registers the lowest axial shrinkage value, 5.91%, and the coarse mesh assumes a value between the refined and intermediate meshes, 6.84%. In elements 11; 24 and 29, the idea of the coarse mesh gives the lower accurately value and the refined mesh gives the most accurately value did not confirm. In elements 122; 625 and 929 from figure 9.25 (a) it is shown that the intermediate mesh assumes the highest axial shrinkage value. In fact, the axial shrinkage behaviour, in the intermediate mesh, starts with an expansion even before the transition temperature. At the end of the sintering cycle, the intermediate mesh assumes an axial shrinkage value around 9.9% while the coarse and refined meshes assume 8.06% and 8.35%, respectively. In the elements 132; 648 and 957, for the three different meshes, the specimen starts to expand and after starts to contract before the transition temperature. The three mesh types start the contraction before the transition temperature. The contraction starts to increase and the intermediate mesh registers the highest value at around 14.77%. The refined and the coarse meshes register the values of 13.6% and 12.5%, respectively.

Following, the relative density evolution along the sintering cycle is studied. It is concluded that independently of the element number in the analysis, the behaviour of the different types of meshes is very similar, more in figure 9.26 (a) and (b) than in figure 9.27 (a) and (b). In figure 9.27 (a) and (b) it is noticed that the intermediate mesh behaves with higher density along the sintering cycle than the coarse and refined meshes. The intermediate mesh reaches a relative density around 0.806 and 0.824 for figure 9.27 (a) and (b) respectively. The coarse and the refined mesh reaches 0.789 and 0.788 and 0.806 and 0.808 also for figure 9.27 (a) and (b), respectively.

Analysing the figure 9.28 (a) and (b) and figure 9.29 (a) and (b), it is concluded,

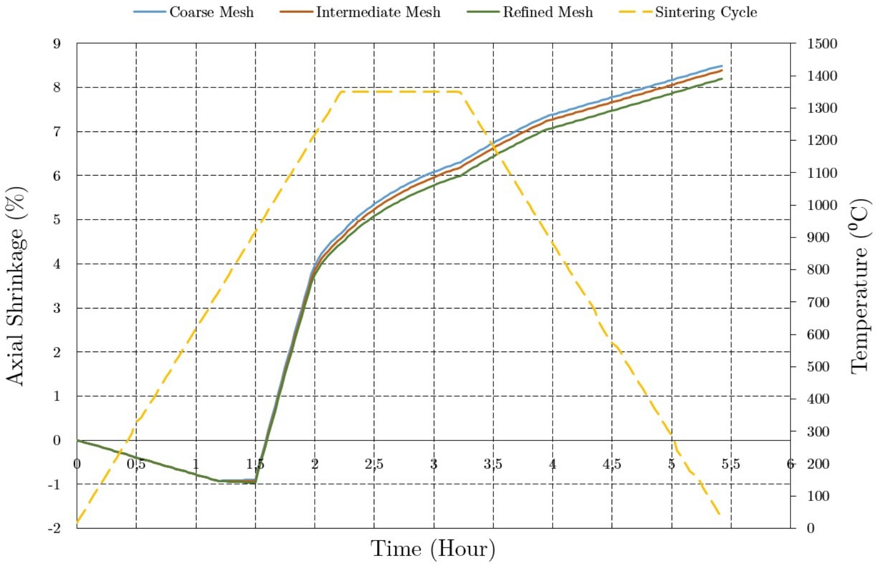

(a) Axial shrinkage evolution along the sintering cycle in element 1 for different mesh types.

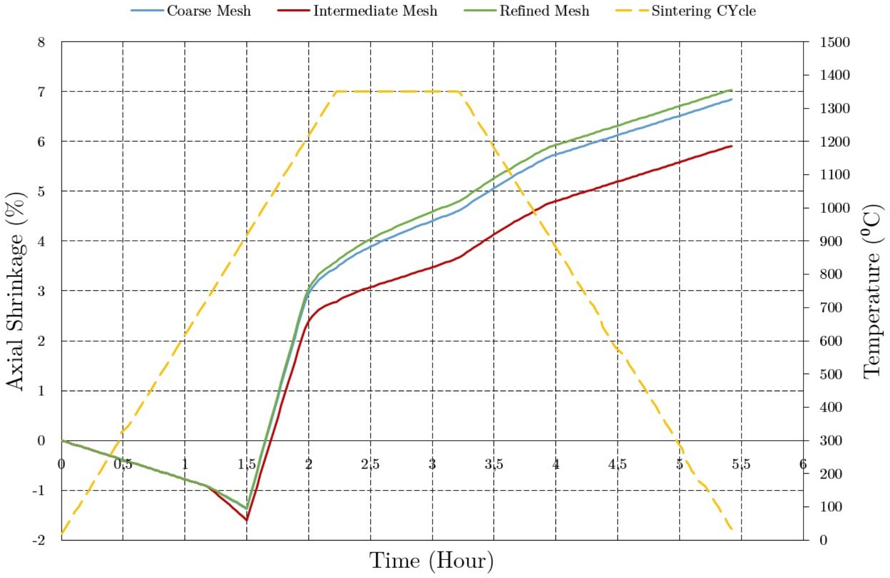

(b) Axial shrinkage evolution along the sintering cycle in elements 11; 24 and 29 for different mesh types.

Figure 9.24: Axial shrinkage evolution along the sintering cycle for the elements in the upper edge.

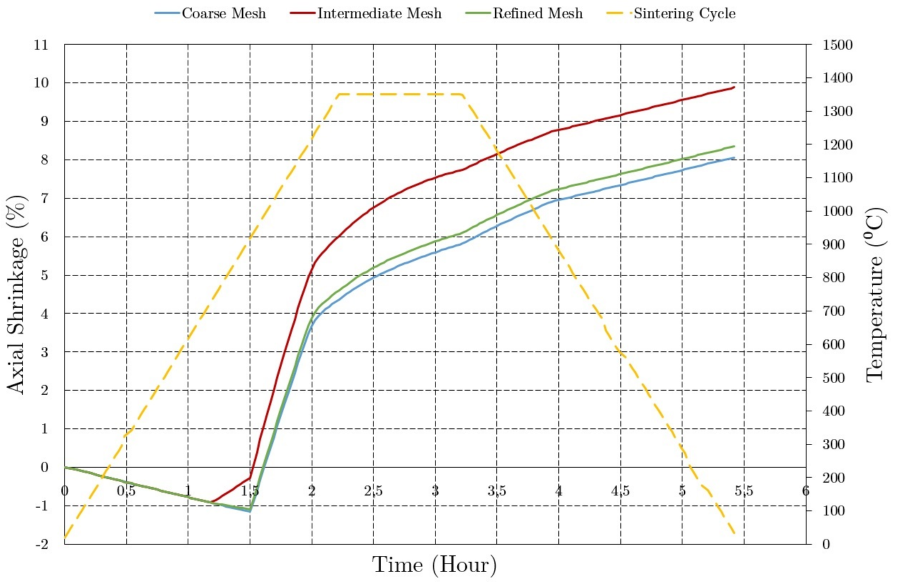

(a) Axial shrinkage evolution along the sintering cycle in elements 122; 625 and 929 for different mesh types.

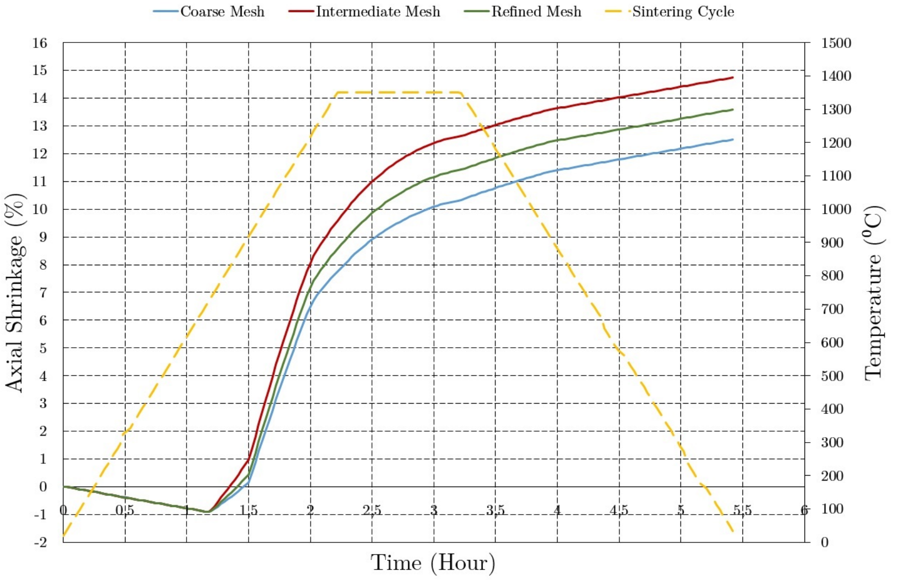

(b) Axial shrinkage evolution along the sintering cycle the elements 132; 648 and 957 for different mesh types.

Figure 9.25: Axial shrinkage evolution along the sintering cycle for the elements in the bottom edge.

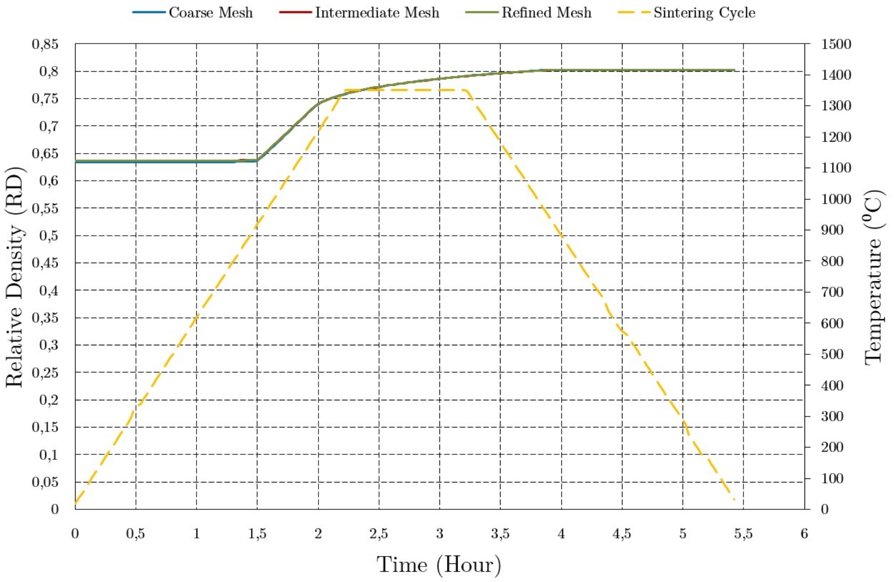

(a) Relative density evolution along the sintering cycle in element 1 for different mesh types.

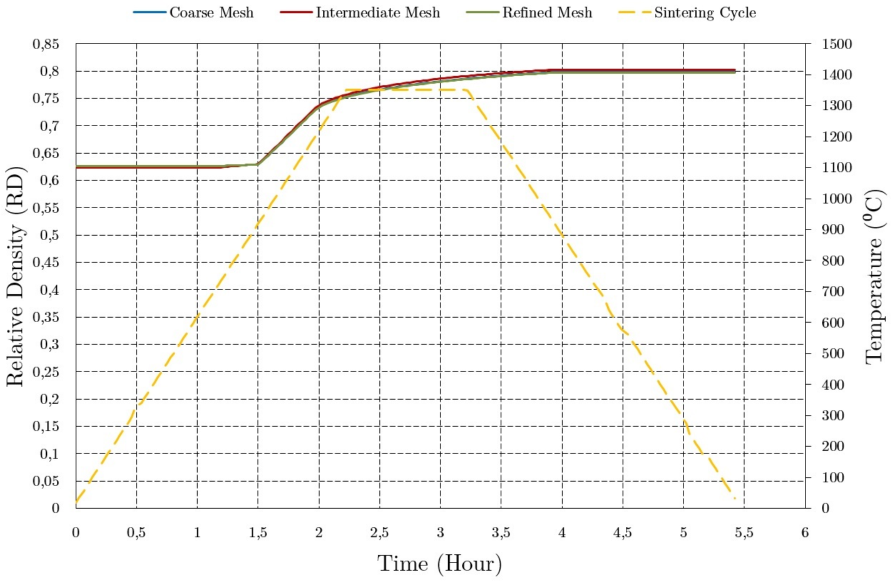

(b) Relative density evolution along the sintering cycle in elements 11; 24 and 29 for different mesh types.

Figure 9.26: Relative density evolution along the sintering cycle for the elements in the upper edge.

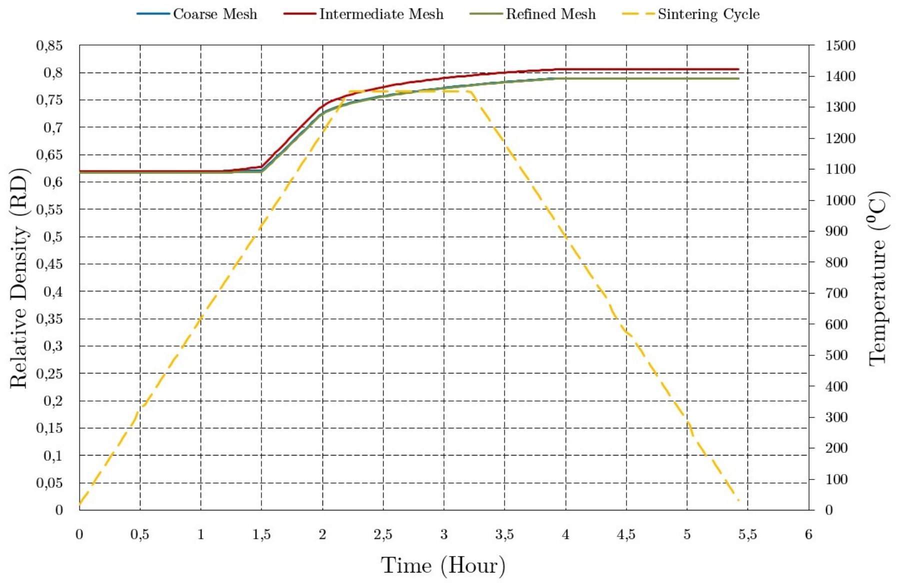

(a) Relative density evolution along the sintering cycle in elements 122; 625 and 929 for different mesh types.

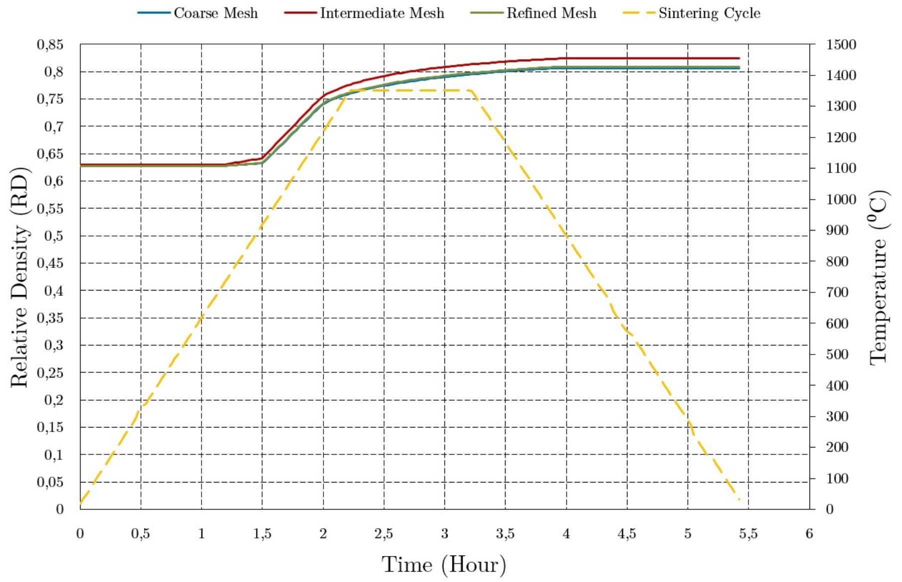

(b) Relative density evolution along the sintering cycle in elements 132; 648 and 957 for different mesh types.

Figure 9.27: Relative density evolution along the sintering cycle for the elements in the bottom edge.

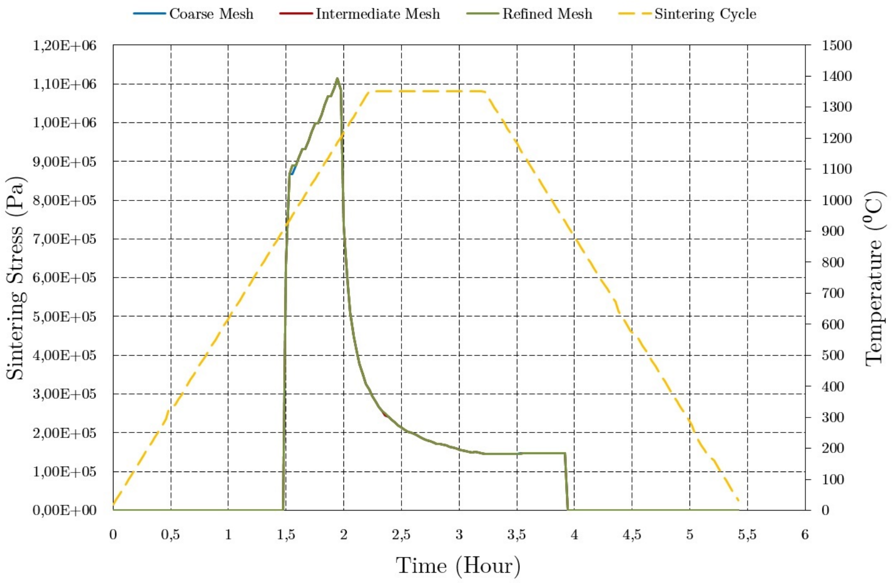

(a) Sintering stress (σ_s) evolution along the sintering cycle in element 1 for different mesh types.

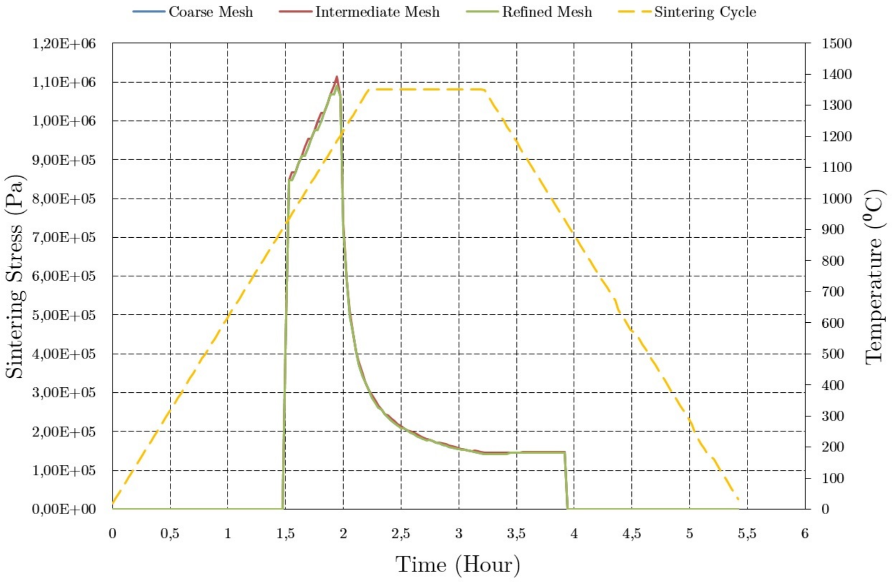

(b) Sintering stress (σ_s) evolution along the sintering cycle in elements 11; 24 and 29 for different mesh types.

Figure 9.28: Sintering stress evolution along the sintering cycle for the elements in the upper edge.

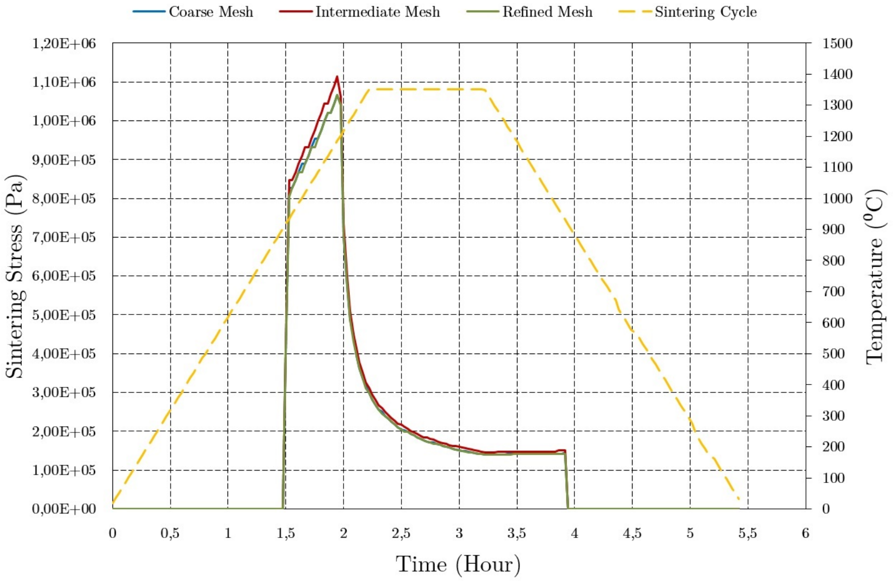

(a) Sintering stress (σ_s) evolution along the sintering cycle in elements 122; 625 and 929 for different mesh types.

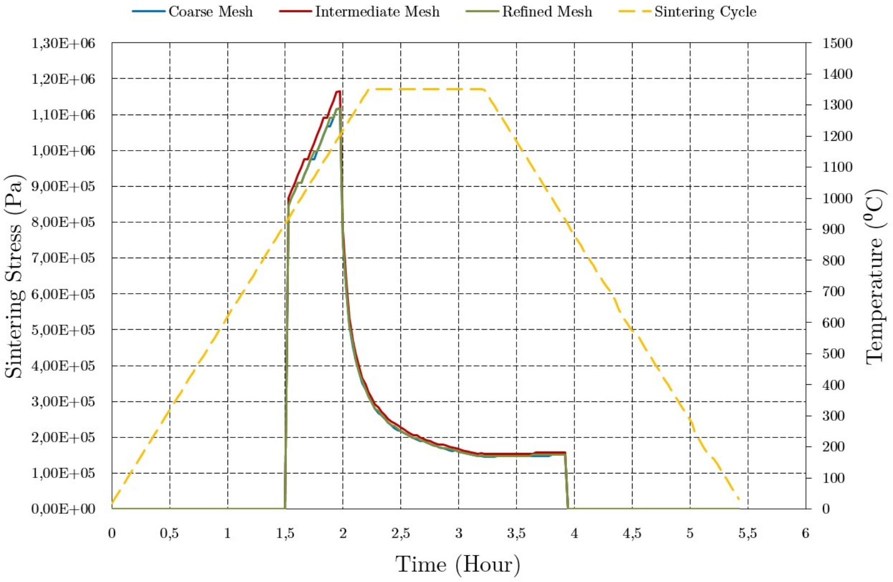

(b) Sintering stress (σ_s) evolution along the sintering cycle in elements 132; 648 and 957 for different mesh types.

Figure 9.29: Sintering stress evolution along the sintering cycle for the elements in the bottom edge.

independently the mesh type, than the sintering stress did not present considerable variation. Observing figure 9.28 (a), there is not any difference testing with a coarse, intermediate or refined mesh. For the three meshes, the sintering stress (σ_s) starts after the transition temperature with a stress around 0.64 MPa and reaches its maximum at 1.1 MPa. After that, with the grain growth increasing, the sintering stress (σ_s) starts decreasing, reaching its minimum at 0.15 MPa. In figure 9.28 (b), the sintering stress behaviour, in the elements 11, 24 and 29, has a similar behaviour to figure 9.28 (a). All the three different mesh types have an identical behaviour. Three mesh types, the sintering stress starts at the transition temperature with 0.41 MPa. At 1200 °C, where the sintering stress reaches its highest value, the coarse and refined meshes reach 1.09 MPa, while the intermediate mesh reaches 1.11 MPa. This can be perceived in figure 9.28 (b), where the intermediate mesh reaches an higher value than the coarse and intermediate meshes. At the end of sintering cycle, the three meshes register the lowest sintering stress at around 0.15 MPa. Analysing figure 9.29 (a), the intermediate mesh starts with a sintering stress around 0.41 MPa, while the coarse and the refined meshes starts with a sintering stress of around 0.4 MPa. The sintering stress maximum value for the intermediate mesh is around 1.11 MPa, while the coarse and intermediate meshes reach 1.07 MPa. At the transition temperature, in the cooling ramp, the intermediate mesh ends with a sintering stress around 0.15 MPa and the coarse and refined meshes end with a sintering stress around 0.14 MPa. In figure 9.29 (b), it is noticed that the sintering stress curve for the three different mesh types has the same behaviour of figure 9.29 (a). For the elements 132, 648 and 957, the intermediate mesh presents the highest values. The difference in the values between the intermediate, coarse and refined mesh is very low. For example, the intermediate mesh begins the sintering stress with a value of approximately 0.86 MPa instead of 0.84 MPa which is verified for the coarse and refined meshes. At the maximum value of sintering stress, the intermediate mesh assumes a value around 1.16 MPa and the coarse and refined meshes assume values around 1.11 MPa. At sintering stress end the intermediate mesh registers a value around 0.16 MPa instead the 0.15 MPa which is verified for the coarse and intermediate meshes.

Part IV

Final Considerations

Chapter 10

Conclusions and Future Works

10.1 Conclusions

In this section, a reflection about the developed work in this document is done and after that, the major conclusions retained are revealed.

A powder metallurgy industrial process adapted to a finite element program was modelled. Not all the steps of the powder metallurgy process were addressed. The concern was in studying the two major steps in powder metallurgy: the compaction process and the sintering process.

A study about soils criteria was developed to simulate the compaction process. With appropriate material parameters and an appropriate soil model applied (in this case the Modified Drucker-Prager/cap model), it was possible to reproduce the compaction process in FEM with good accuracy. In the end of this stage, the reference parameter to control was the relative density, however the von Mises stress behaviour along the compaction process was also studied. The relative density had an expected behaviour, because the plastic volumetric strain had a deformation around 50%, therefore the relative density had to increase 100% in order to its initial value, and this is what actually happened. Analysing the residual stress, expected values were obtained, this is, it is a relatively low stress value along the specimen.

In the sintering process, it was necessary to implement a viscoelasticity model. The viscoelasticity model was implemented based on the Maxwell model, considering thermal deformation. This same model accounts for grain growth. Thus, the viscoelasticity was implemented in a finite element code in association with grain growth model, being possible to predict the shrinkage in the sintering process. In this sintering process there was a connection with inhomogeneous factors such as initial density distribution and the residual stress resulting from die compaction. The viscoelasticity model was successfully implemented in an user's subroutine, CREEP, after some validation tests. This subroutine has shown good behaviour when applied in the case study. The main parameters like sintering stress, viscosity, porosity work successfully between them.

Subsequently, a sensitivity study about the different mesh types was carried out. In the compaction stage, it was noticed that the influence of the refinement of the meshes was not relevant, except for the punch force, where the difference was notorious. In the sintering stage, the axial shrinkage is the parameter in which the discrepancy between meshes is more accentuated. All the other parameters that were important to study in sintering, it was concluded that there was not significant variance with the refinement of mesh.

10.2 Future Works

The main objectives that were proposed for this research were reached. The two major phases that describe the PM industry process were both implemented, i.e., the Drucker-Prager soil criteria and the viscoelasticity model were successfully implemented in a finite element program.

However this was an introductory study in the powder metallurgy processes, therefore, it is necessary to continue the work in this area. Some suggestions that is registered are:

- Testing the developed model but for other types of geometry and testing in a geometry which is not axisymmetric;
- Adapting this model for other types of materials, like an alumina powder, which is a very common material in powder metallurgy;
- Testing the compaction model using another soil criteria that many researchers use in the powder area, the Cam-Clay model;
- Apply the porous elastic model instead of the linear elastic model;
- Implement an UMAT subroutine instead of the CREEP subroutine for a stainless steel and compare the results between an UMAT and a CREEP subroutine.

Bibliography

[1] R Zhang. *Numerical simulation of solid-state sintering of metal powder compact dominated by grain boundary diffusion.* PhD thesis, The Pennsylvania State University, 2005.

[2] Randall German, M. Powder Metallurgy of Iron and Steel. In *Powder Metallurgy of Iron and Steel*, chapter The Powder, pages 29–44. John Wiley & Sons, Inc., New York, 1998.

[3] http://www.gkn.com/sintermetals/capabilities/soft-magnetic-pm/process/Pages/Sintered-Soft-Magnetic-products.aspx, visto em 1/10/14.

[4] Gautam Wagle, S. *Die compaction simulation: simplifying the application of a complex constitutive model using numerical and physical experiments.* PhD thesis, The Pennsylvania State University, 2006.

[5] http://www.designinsite.dk/htmsider/pb1007.htm, visto em 23/09/14.

[6] Ecole Des and Mines D Albi Carmaux. Numerical Methods for Predicting Powder Rolling. 2003.

[7] Randall M. German. *Sintering Theory and Practice.* John Wiley & Sons, Inc., New York, 1996.

[8] Suk-Joong L. Kang. *Sintering.* Elsevier, 2005.

[9] J. Song. *Experiments, modelling and numerical simulation of the sintering process for metallic or ceramic powders.* PhD thesis, Southwest Jiaotong University, 2007.

[10] C Greskovich and K W Lay. Grain Growth in Very Porous. *Journal of The American Ceramic Society*, 55(3):142–146, 1972.

[11] B.P. Kashyap and K. Tangri. Grain growth behaviour of type 316L stainless steel. *Materials Science and Engineering*, A149(1992):L13–L16, January 1992.

[12] Randall German, M. Grain Growth in Austenitic Stainless Steels. *Metallography*, 11(1978):235–239, 1978.

[13] F.J. Humphreys. A unified theory of recovery, recrystallization and grain growth, based on the stability and growth of cellular microstructuresI. The basic model. *Acta Materialia*, 45(10):4231–4240, October 1997.

[14] Bruno Barroqueiro. *Modelação e Análise Numérica de Tratamentos Térmicos.* PhD thesis, Universidade de Aveiro, 2013.

[15] Críspulo Gallegos and Francisco J Martínez Boza. Linear Viscoelasticity. *Rheology*, I.

[16] Frank P Incropera, David P DeWitt, Theodore L Bergman, and Adrienne S Lavine. *Fundamentals of Heat and Mass Transfer*, volume 6th of *Dekker Mechanical Engineering.* John Wiley & Sons, 2007.

[17] J. Brewin, P.; Coube, O.; Doremus; P.; Tweed. *Modelling of Powder Die Compaction.* 2008.

[18] A. Kakani, S.; Kakani. *Material Science.* New Age Internation (P) Limited, New Dehli, 2004.

[19] SC Lee and KT Kim. Densification behavior of aluminum alloy powder under cold compaction. *International journal of mechanical sciences*, 44:1295–1308, 2002.

[20] Baosheng Zhang, Mukesh Jain, Chenghao Zhao, Michael Bruhis, Roger Lawcock, and Kevin Ly. Experimental calibration of density-dependent modified Drucker-Prager/Cap model using an instrumented cubic die for powder compact. *Powder Technology*, 204(1):27–41, December 2010.

[21] I Aydin, BJ Briscoe, and KY anlitürk. The internal form of compacted ceramic components: a comparison of a finite element modelling with experiment. *Powder Technology*, 89:239–254, 1996.

[22] Tuhin Sinha, Jennifer S. Curtis, Bruno C. Hancock, and Carl Wassgren. A study on the sensitivity of DruckerPrager Cap model parameters during the decompression phase of powder compaction simulations. *Powder Technology*, 198(3):315–324, March 2010.

[23] a. Arockiasamy, S. J. Park, and Randall M. German. Viscoelastic behaviour of porous sintered steels compact. *Powder Metallurgy*, 53(2):107–111, June 2010.

[24] Julian Vincent. Basic Elasticity and Viscoelasticity. In *Structural Biomaterials*, chapter 1. Princton University Press, third edition, 1990.

[25] M. Zhang, Rui; Engel, S., Renata; Salomon, J., Nicholas; Randall. Finite Element Analysis on the Sintering of Stainless Steel 316L Powder Compacts. In *Proceedings of the 2002 World Congress on Powder Metallurgy and Particulate Materials*, number 1990, Orlando, 2002.

[26] Hibbit, Karlsson, and Sorensen. *ABAQUS/Standard Documentation.* Hibbit, Karlsson, Sorensen Inc., USA, 2010.

[27] M. Shamasundar, S.; Chidanand, G.; Sachim, B. Finite Element Modeling of Powder Compaction and Ejection Process, 2006.